CHAPTER 1

INTRODUCTION

Inplane walls act as diagonal bracing elements and attract significant lateral loading due to their high stiffness, which leads to potential diagonal failure of such walls. Wide spaced reinforced masonry (WSRM) walls subjected to inplane loading exhibit complex structural behaviour that is not well understood in spite of a few years of investigation in several parts of the world on walls of similar design. This thesis provides the reader better insight into the behaviour of WSRM walls subjected to racking loading through experimental and numerical investigations.

Inplane behaviour of WSRM walls containing vertical reinforced cores at horizontal spacing up to 2000mm and no horizontal reinforcement except bond beams at roof level is investigated in this thesis. WSRM walls are considered as a structural system defined by the interaction between the unreinforced masonry (URM) panels, the vertical reinforced cores and the bond beam. Elastic analyses of the walls are performed to infer the potential failure mode and stress distribution in the WSRM walls affected by the presence of vertical grouted cores. Hypotheses of nonlinear behaviour including cracking of WSRM and URM walls are formulated from the results of the elastic FE analyses. The hypotheses are validated using experimental investigation of ten full-scale WSRM and Non-WSRM shear walls. Shear capacity, ductility and damage characteristics of the shear walls have been evaluated from the experiments, compared with the provisions of AS3700 (2001) and formulae available in the literature where possible and are reported in this thesis. As the experiments have been carried out on walls of one aspect ratio (0.84) subjected to one level of vertical compressive pressure loading (0.50 MPa), to understand comprehensively the behaviour of WSRM walls of all other aspect ratios and subjected to

different vertical compressive pressure levels, an explicit FE model incorporating a macro masonry material model reported in the literature is developed. The FE model effectively captures the behaviour of the WSRM and Non-WSRM shear walls obtained from the experiments. The predicted behaviour of WSRM shear walls of other aspect ratios (0.50, 1.11) subjected to vertical compression (0MPa and 0.25MPa) by the FE model are validated by constructing and testing four additional WSRM walls. The validated FE model is then used for the examination of the appropriateness of the design prescriptions in AS3700 (2001) for WSRM shear walls suitable for small buildings in the Australian regions of wind category N4, C2 and earthquake category H1, H2, H3.

1.1 Aim and Objectives of the Thesis

The main aim of this thesis is to comprehensively understand the inplane response of WSRM walls. This aim will be achieved through the following enabling objectives:

(i) To gather information on the existing knowledge on the response of masonry shear walls through a comprehensive literature review.

(ii) To examine the elastic response of WSRM shear walls and formulate hypotheses of nonlinear and failure behaviour of these walls.

(iii) To carry out experiments on full-scale walls with a view to examining the appropriateness of the hypotheses formulated in (ii).

(iv) To develop an efficient FE model capable of predicting the behaviour of the WSRM shear walls.

(v) To validate the FE model for cases that have not been included in (iii) by carrying out additional experimental investigations.

(vi) To apply the validated FE model to examine the effectiveness of the design parameters to the response of WSRM shear walls.

(vii) To use the validated FE model to verify the prescriptive designs provided in AS3700 (2001) for WSRM shear walls suitable for small buildings.

1.2 Scope and Limitations

The scope of the thesis is to examine the inplane response of WSRM walls. Walls that do not satisfy the design specifications of WSRM walls will also be included for completeness.

The following is a list of limitations:

- The experiments deal with shear walls made from clay blocks only. However, the FE model developed will be capable of dealing with both the concrete and clay masonry shear walls.
- The thesis is developed for understanding the behaviour of single leaf shear walls only
- The shear walls will have no horizontal reinforcement except in the bond beams
- Out-of-plane behaviour of walls will not be considered

1.3 Outline of the Thesis

This thesis consists of nine chapters.

Chapter 1 provides an introduction and states the aim, objectives, scope and limitations of the research.

Chapter 2 reports a review on the structural behaviour of masonry shear walls. It includes theory of shear walls and their failure modes, and equations for the prediction of shear capacity of URM and WSRM walls. Critical parameters including the reinforcement, the vertical compression, the aspect ratio (shape of the walls) and the material properties that affect the behaviour of the shear walls are also reviewed. Typical experimental studies on the masonry walls conducted in different parts of the world are also discussed. A critical review of the design principles of the masonry shear walls and the state-of-the-art of masonry shear walls research in this aspect is provided in this chapter. Constitutive relations of masonry materials required in developing the FE model are reviewed in detail. Theory of plasticity and the most commonly used failure theories of masonry are also included.

Chapter 3 discusses the elastic behaviour of the WSRM shear walls obtained from micro modelling analysis. This chapter aims at studying the stress distribution in the critical zones of shear walls that could lead to potential failure. The effect of the vertical grouted cores to the stress distribution at the critical zones and to the global behaviour of the WSRM walls is also discussed.

Chapter 4 presents the design of the first phase of experiments (ten full-scale walls), construction and testing procedures. Details of arrangement of boundary conditions, positioning of sensors and data acquisition system are also included in this chapter. Failure mechanism and crack patterns of the shear walls observed during experiments are presented. Typical data collected during the testing process and their use for extracting the behaviour of the walls is explained.

Chapter 5 reports the load-displacement curves obtained from the experiments and presents the effect of loading history (monotonic/cyclic) to the overall behaviour of the WSRM walls. Damage characteristics such as stiffness degradation, diagonal deformation, and deformations at critical zones are examined with reference to the overall drift of the shear walls with the

increasing lateral loading. Shear capacity of the walls predicted by different empirical equations is also reported and compared with that from the experiments.

Chapter 6 presents an explicit finite element model for the analysis of the WSRM and the Non-WSRM walls. Theory of macro modelling for masonry, and yield and failure surfaces for masonry and grout are reviewed. Parameters that define the yield surface of masonry under biaxial loading are discussed. The basics of the explicit algorithm of finite element analysis (FEA) are briefly discussed. The method of incorporating the masonry material model into ABAQUS/Explicit through the VUMAT user material subroutine is described. Procedures for obtaining the stable nonlinear solutions are also discussed in detail.

Chapter 7 validates the FE model developed in Chapter 6 with the WSRM walls of different aspect ratios and subjected to different vertical loadings. Modes of failure, load-deformation response and shear capacity of the validation test walls obtained from the FE model are compared with those obtained from the experiments (four full-scale walls). Shear capacity of the validation test walls predicted by AS3700 (2001) and by the FE model are also compared with that obtained from the experiments. Effects of the aspect ratio and the vertical stress to the behaviour of the WSRM walls are discussed in this chapter.

Chapter 8 examines the applications of the FE model to some problems of practical significance. For this purpose, a concrete masonry WSRM shear wall (one of the prescriptions in AS3700 (2001)) suitable for small buildings in the Australian regions of wind categories N4, C2 and earthquake categories H1, H2, H3 is selected. Effect of variability of material properties to the racking load response of the wall is reported. For this purpose material variability is assumed with 20% coefficient of variation and data are spread for 3 standard deviations. Shear capacities of the selected wall obtained from the FE analyses are compared with that obtained from the

prescriptions of AS3700 (2001). The effect of the width of door openings to the load-displacement response and ultimate shear capacity is also discussed.

Chapter 9 includes the major and specific conclusions obtained from the experimental as well as FE modelling studies. This chapter also discusses recommendations for future studies.

CHAPTER 2

MASONRY SHEAR WALLS – A LITERATURE REVIEW

2.1 Introduction

This chapter reports a review of the structural behaviour of masonry shear walls. Theory of shear walls including the analysis of stresses in critical regions of the shear walls, failure modes and shear capacity is reviewed in this chapter. Various types of masonry shear walls, namely the unreinforced and ungrouted, the partially grouted unreinforced, the partially reinforced, the fully reinforced and the wide spaced reinforced are discussed. Critical design parameters including the reinforcement, the vertical compression, the aspect ratio (shape of the walls) and the material properties that affect the behaviour of the shear walls are reviewed. Mechanical properties of masonry such as the compressive strength, the elastic modulus, the tensile strength and shear strength, and the tensile crack opening energy are also discussed.

As the constitutive relations of masonry materials including the failure mechanism are required to develop finite element models to simulate the behaviour of masonry shear walls, such material models and finite element models are reviewed in detail. Review of the theory of plasticity and the most commonly used failure theories is also included. A critical review of the design principles of the masonry shear walls and the state-of-the-art of masonry shear walls research is provided in this chapter.

2.2 Theory of Shear Walls

Australian Standard for concrete structures AS3600 (2000) defines a wall as a structural element whose width is larger than three times its thickness. When walls are subjected to inplane vertical and lateral loading induced by wind or earthquake, they are called shear walls. The seismic behaviour of buildings is strongly affected by the arrangement of shear walls, the rigidity of floors and the connections of floors to the walls. Shear walls are normally arranged such that they resist lateral load on either axis of the building effectively. A typical apartment building is shown in Fig. 2.1 where solid lines represent the locations of shear walls.

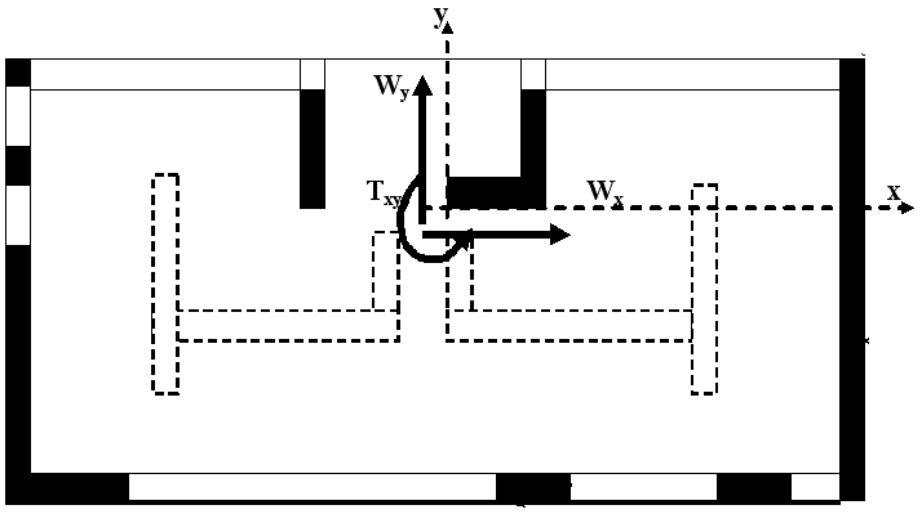

Figure 2.1: Shear walls in an apartment building

W_x, W_y and T_{xy} in Fig. 2.1 are the total lateral forces and the torque acting in the x-y plane induced by earthquake or wind action. Shear walls, based on their relative stiffness in each direction, resist the lateral forces and the torque. The resultant inplane resistance at the centre of gravity of the building is shown as W_x and W_y. In addition to the inplane forces, additional forces are also induced due to out-of-plane loading on flexural walls that are square to the shear walls as shown in Fig 2.2.

For the purpose of the analysis, when L=H the shear walls are termed square shear walls; when L << H they are termed tall shear walls, and when L >>H they are known as squat shear walls. According to AS3600 (2000), a wall can act like a column in compression, as a beam when cantilevered at one end and as a slab when loaded transversely depending on the loading configuration and support system. From the design viewpoint shear walls are also known as bracing walls. In this chapter only the analysis and design aspects of the shear walls are discussed and walls subjected to out-of-plane bending are considered out of the scope of this thesis.

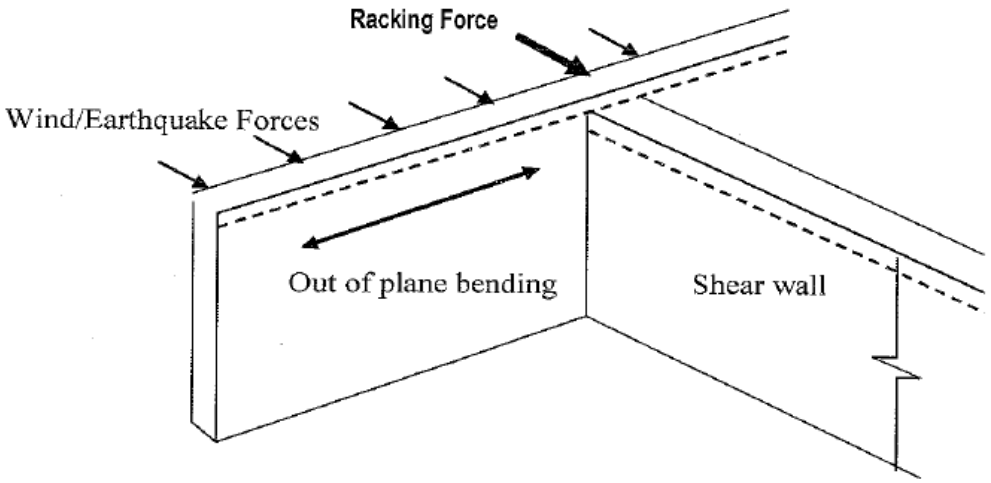

Figure 2.2: Transfer of racking forces to a shear wall

2.2.1 Analysis of Stresses

Shear walls undergo relative lateral deformation from the bottom layer to the top and hence they are usually regarded as cantilever walls (fixed at the base, free at the top) loaded vertically and laterally as shown in Fig. 2.3. Heel, toe, centre and local point of application of load on the shear wall are the critical regions. Failure in these regions mainly controls the overall behaviour of the shear walls.

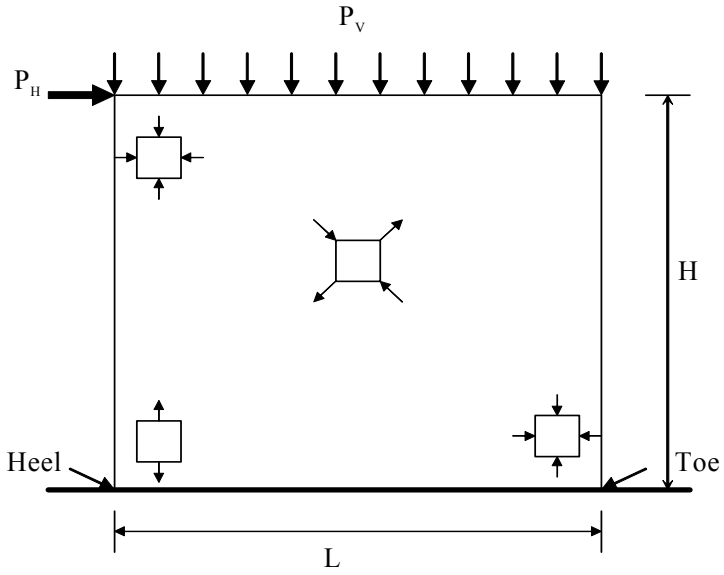

Figure 2.3: A typical shear wall for analysis consideration

Usually toe crushing occurs due to biaxial compressive stresses, failure at the heel occurs due to vertical tensile stresses and shear failure along the diagonal of the wall occurs due to the combination of principal tensile and compressive stresses along the diagonal.

2.2.2 Failure of Shear Walls

Shear walls fail either due to toe crushing or due to tensile cracking at the heel or followed by shear failure along the diagonal. Failure can also occur due to a combination of two or more modes. Tall walls usually fail due to a progressive flexural mechanism characterised by heel cracking followed by toe crushing as shown in Fig. 2.4(a) whilst the squat shear walls predominantly fail by diagonal cracking as shown in Fig. 2.4(b). Square shear walls generally fail due to a combined mechanism (tension at the heel, crushing at the toe and shear along the diagonal).

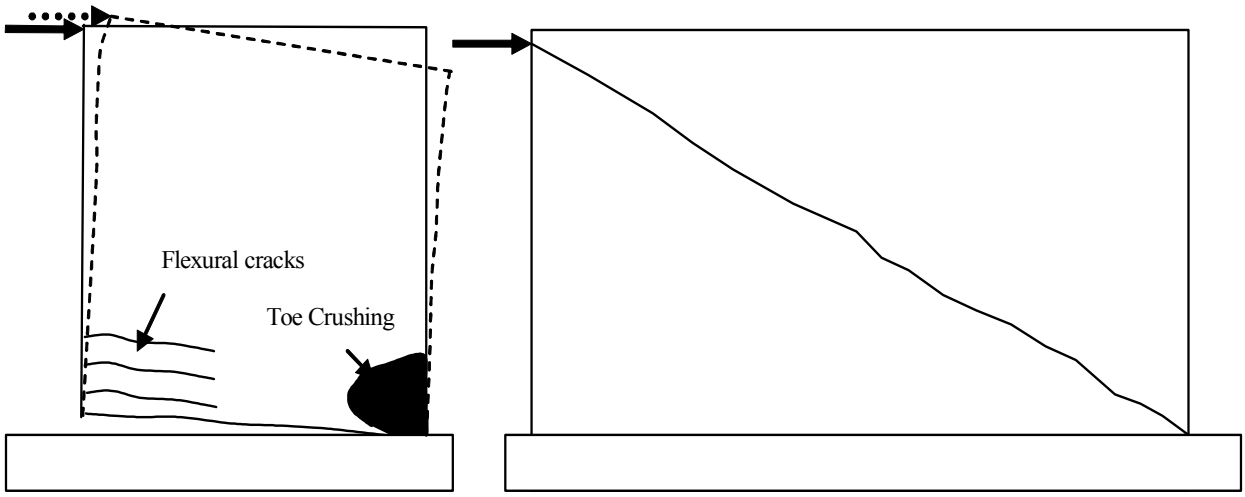

Figure 2.4: Failure mechanisms of shear walls

Shear behaviour of a squat reinforced wall depends upon several complicated mechanisms such as the compression strut mechanism, the aggregate-interlock forces, and the dowel action of the vertical reinforcement. In squat walls, flexure and shear cannot be separated and are discussed together because they are interrelated mechanisms, whereas in tall walls failure is dominated by bending. Eccentrically loaded masonry walls fail when the compressive strength of the masonry reaches its ultimate value. Brunner and Shing (1996) have shown that when the walls fail in a combined flexural and shear mode of failure, they exhibit higher lateral load resistance than if they fail only due to flexure.

Reinforcing steel is usually provided to resist lateral wind pressure (especially in high wind regions) induced flexure; they also resist tensile and shear stresses due to inplane loading. Fig. 2.5 shows the stresses induced in the reinforcement and at the toe of the shear wall subjected to lateral inplane loading. Under inplane loading, depending on the relative magnitudes of the vertical (P_V) and horizontal (P_H) load, the heel is generally subjected to tensile stresses and the toe is subjected to an increased level of compressive stress.

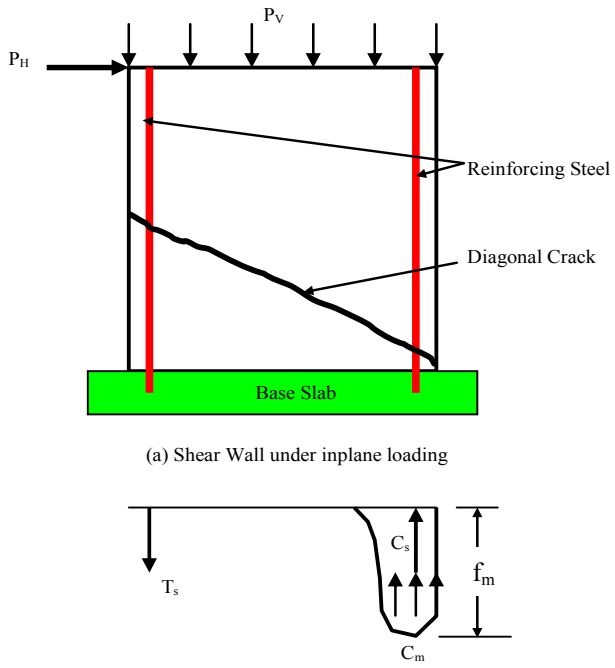

Figure 2.5: Stress distribution in a shear wall under lateral inplane loading

Depending on the lateral tie down details of the compression steel near the toe region, compressive force (C_s) develops in the steel. Where the steel reinforcement is not tied down (as in most masonry walls), its contribution to the load bearing is discounted as the reinforcement bars buckle and do not utilise their compression capability. Therefore it is common to ignore the reinforcement bars in the analysis of the toe region of shear walls.

2.3 Types of Hollow Block, Single Leaf Masonry Shear Walls

Masonry is typically constructed with no reinforcement in most parts of the world where earthquake and wind hazards are minimum. Such masonry is regarded as unreinforced masonry (URM). URM may either be constructed of solid bricks and mortar or hollow blocks and mortar. Some selected or all the cores of the hollow URM walls may be grouted to increase their vertical load carrying capacity or to account for local concentrated loading (to avoid bearing failure). If all cores of URM are grouted, it is termed grouted masonry (GM), whereas when selected cores

are grouted it is known as partially grouted masonry (PGM). The grouted cores may contain reinforcement in cases where seismic or wind hazards are accounted in the design. Depending on the reinforcement, they are regarded as partially reinforced masonry (PRM), or reinforced masonry (RM). According to Australian Standard for masonry structures (AS3700 (2001)), the masonry walls that contain reinforcement in both the vertical and the horizontal directions at spacing not greater than 800mm are classified as RM walls, and the masonry walls that contain reinforcement bars at spacing between 800mm to 2000mm are defined as wide spaced reinforced masonry (WSRM) walls. Types of masonry walls are schematically shown in Fig. 2.6.

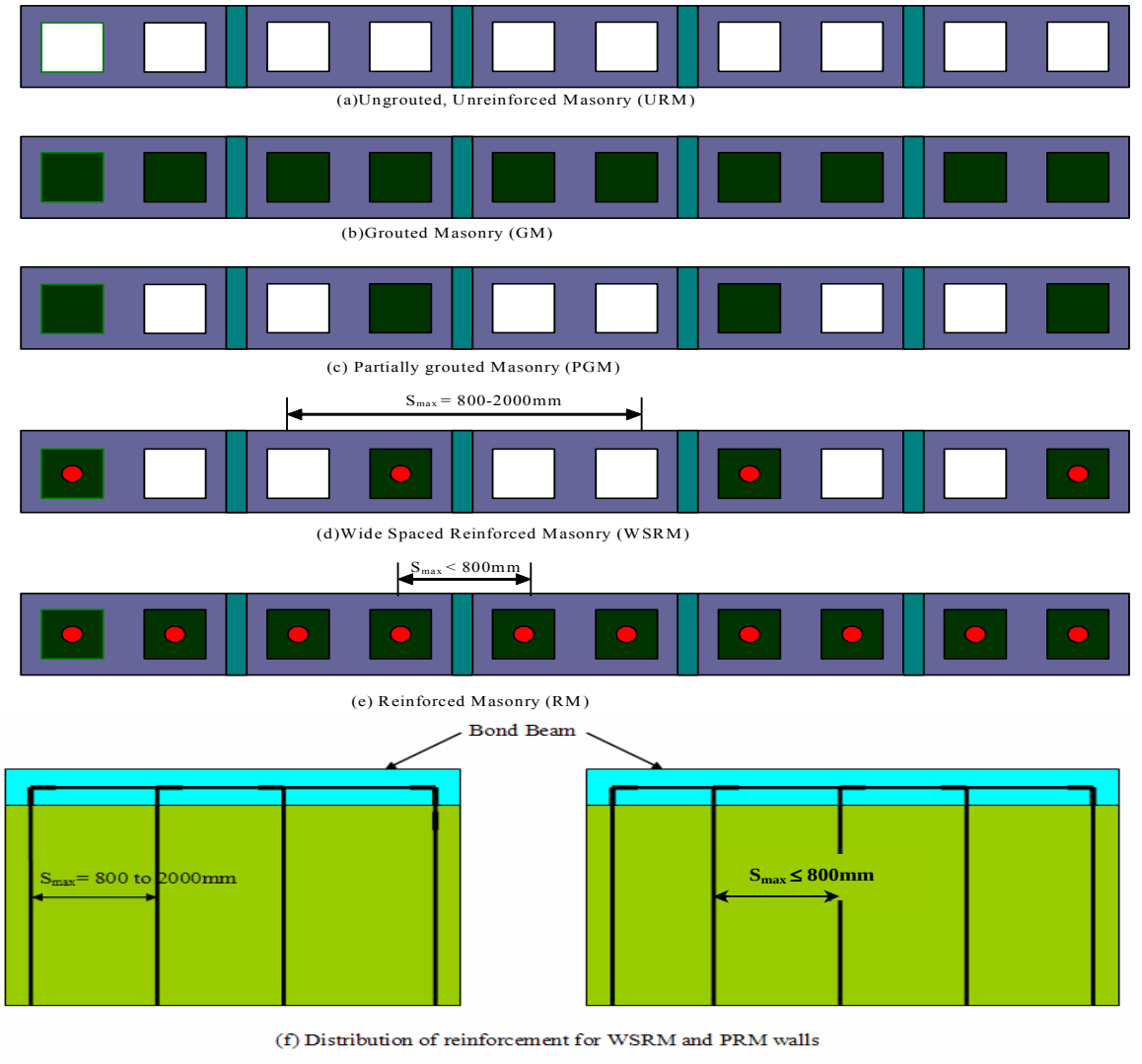

Figure 2.6: Types of masonry shear walls

Australian Standard for masonry structures AS3700 (2001) requires wide spaced reinforced masonry (WSRM) walls to meet the following details of reinforcement:

- Vertical reinforcement is spaced at centres not exceeding 0.75H and in any case not greater than 2000mm horizontally, where 'H' is the height of the wall
- Horizontal reinforcement is spaced at centres not exceeding 0.75L and in any case not greater than 3000mm vertically, where 'L' is the length of the wall
- Area of the vertical reinforcement is at least 0.13% of the design area of the wall and the area of the horizontal reinforcement is at least 0.07% of the design area of the wall. (Design area for the WSRM walls is equal to the area of the grouted cores plus the bedded area of the ungrouted masonry).

In this thesis, behaviour of the WSRM is investigated; however, URM walls are also included to provide a basic datum reference in discussions.

2.4 Unreinforced Masonry Shear Walls

Unlike other popular structural materials (concrete or steel), masonry exhibits orthotropic behaviour due to mortar joints acting as planes of weakness. Most commonly the failure of masonry can be predicted by using the biaxial failure criterion. It is well known that the strength of masonry is affected by the magnitude and orientation of the principal stresses to the bed or head joints, which was investigated by Samarasinghe et al. (1981), Page (1982) and Dhanasekar (1985).

2.4.1 Failure Modes

The heterogeneity of the masonry induces a multitude of causes for the failure of masonry walls. The cause that provides the lowest bound is therefore critical. For URM walls, three failure pattern modes under inplane loading have been observed by several researchers (Zhuge (1995), Mahmoud et al. (1995), Drysdale et al. (1993)). These modes are shear sliding, rocking and diagonal shear as shown in Fig. 2.7.

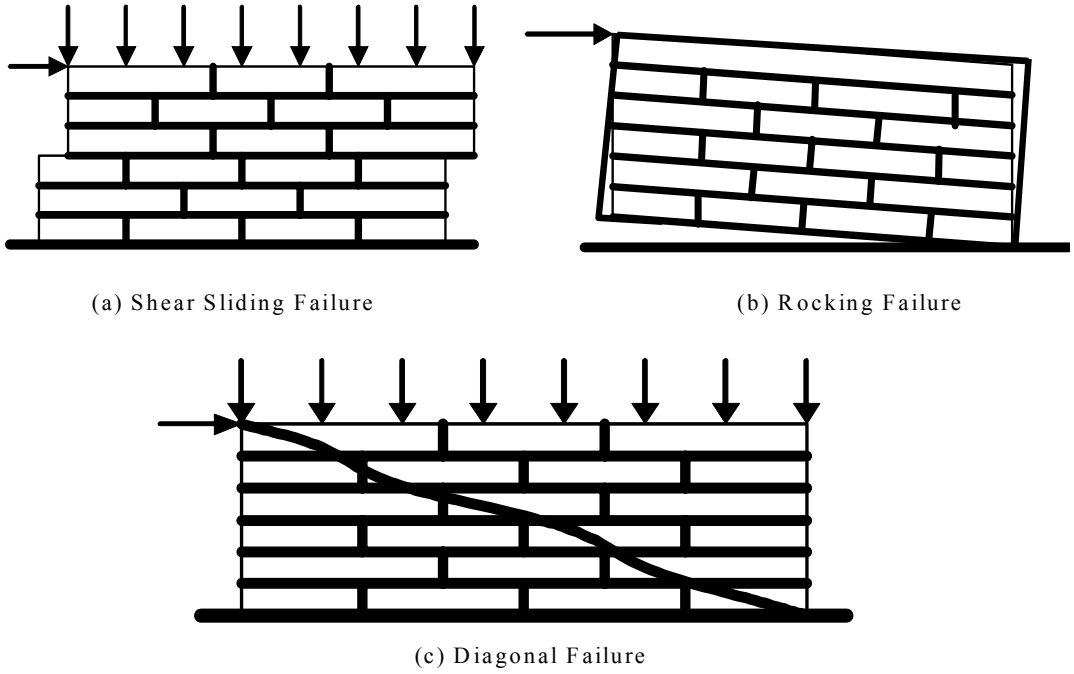

Figure 2.7: Failure modes of URM walls under inplane loading

Shear sliding along the bed joints occurs when the shear stress (τ) on a horizontal mortar joint exceeds the sum of the bond strength of that mortar joint (τ_m) and the frictional stress between the mortar and the units. Diagonal shear failure occurs when the diagonal tensile stress resulting from the compression shear state exceeds the splitting tensile strength of masonry. Rocking mode of failure occurs due to overturning caused by either low level of axial load and/or weak tensile bond strength of mortar joints dominated by poor workmanship.

Several researchers have found that the vertical compressive stress affects remarkably the type of failure of URM shear walls (Dhanasekar (1985), Zhuge (1995), Mahmoud et al. (1995)). Low levels of 'σ_v' induce failure in the horizontal bed joint, moderate levels of 'σ_v' induce tensile cracking in the masonry units, and high levels of 'σ_v' lead to compressive failure.

2.4.2 Shear Capacity

Ultimate shear capacity of URM walls is influenced by three parameters, namely the mortar strength, the inplane vertical compressive stress (σ_v) and the aspect ratio. For design purposes, the shear capacity of URM shear walls is usually expressed by the relationship between the ultimate shear strength (τ) and the axial compressive stress (σ_v) using the Coulomb type criterion shown in Eq. (2.1).

$$\tau = \tau_o + \mu\sigma_v \qquad (2.1)$$

in which 'τ_o' is the bond shear strength between the mortar and masonry units at zero axial stress and 'μ' is the friction coefficient at the brick mortar interface. Bond between the base of the URM wall and the supporting foundation plays a significant role in resisting the inplane horizontal loading. Mullins and O'Connor (1994) advocated for the consideration of a crack of zero tensile strength at the interface of the wall and the supporting foundation whilst considering the capacity of the joint due to friction. This means that the shear Eq. 2.1 is simplified as $\tau = \mu\sigma_v$.

Hendry (1978) has derived Eq. 2.2 to incorporate the nonlinear relationship between the shear strength and the normal stress.

$$\tau = \tau_o^2 + 1.1\tau_o\sigma_v + 0.053\sigma_v^2 \qquad (2.2)$$

Due to limitations of Eq. 2.2, research has been carried out to develop the failure surface of masonry. Samarasinghe et al. (1981) first derived a biaxial failure criterion with consideration of the bed joint orientation, Page (1982) derived failure surface for masonry under biaxial compression, and Dhanasekar et al. (1985b) developed a three a dimensional failure surface in terms of principal stress space and orientation of bed joints (σ_1, σ_2, θ). Ali and Page (1986) derived a three-dimensional surface for the shear failure of the joint.

2.5 Reinforced Shear Walls

In the areas of high seismic intensity, URM shear walls are not recommended because they have limited capacity to withstand the ground excitation. Therefore in those regions construction of RM walls is required. Since the behaviour of reinforced masonry is quite similar to that of reinforced concrete (RC) structural elements, the prediction of the capacity and deformability of reinforced masonry walls could be made analogous to the reinforced concrete elements. The resistance of RM shear walls to inplane loading is provided predominantly by their in-plane shear or flexural capacity. It depends upon the wall geometry, the level of axial stress, properties of masonry materials, and the amount and distribution of the vertical and the horizontal reinforcement.

2.5.1 Shear Capacity

Capacity of reinforced concrete (RC) shear walls is usually calculated using a truss analogy, which assumes that a pattern of parallel cracks form in the region of high shear. Warner et al. (1999) suggest that the concrete between the adjacent inclined cracks carries an inclined compressive force and hence acts like a diagonal compressive strut, whereas the vertical reinforcement acts like a tie to carry the tensile force as shown in Fig. 2.8.

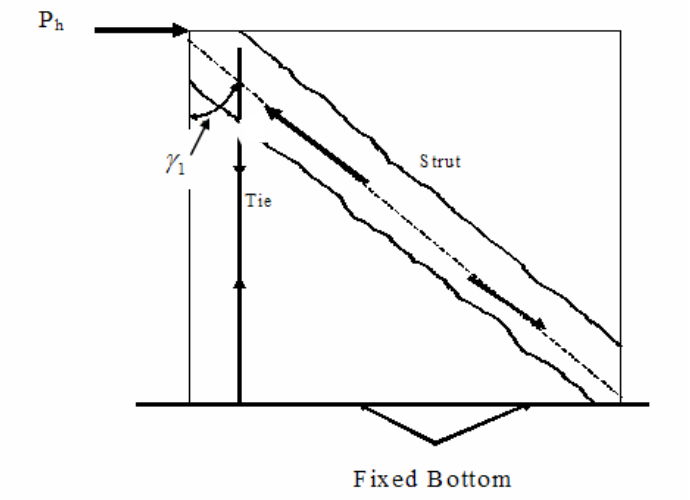

Figure 2.8: Strut and tie model for an RC shear wall

Warner et al. (1999) provided Eq. (2.3) to calculate the ultimate capacity of an RC shear wall.

$$V_u = \frac{f_c^{'}\ t_w\ d_w\ Sin\gamma_1\ Cos\gamma_1}{1.14\ +\ 0.68\ \cot^2\gamma_1} \qquad (2.3)$$

in which '$f_c^{'}$' is the characteristic compressive strength of concrete, 't_w' is the thickness of the wall, 'd_w' is the width of the compression strut and 'γ_1' is the angle of inclination of the compression strut with the vertical.

Sio (1994) has also predicted the capacity of RC shear walls using a strut and tie model. Toscan (2001) used the strut and tie model originally proposed by Warner et al. (1999) for RC shear walls to calculate the capacity of WSRM shear walls with two grouted cores and three grouted cores. Cruz-Diaz et al. (2002) developed Eq. (2.4) based on a compression strut model to determine the capacity of masonry infilled shear walls.

$$V_u = t_w\ l_b \left(\frac{l_b}{l_c}\right)^{r'} \sigma_b .\ \ Sin\ \gamma_1 \qquad (2.4)$$

in which 't_w' is the thickness of the wall, 'l_b' is the length of brick, 'l_c' & 'r' are curve-fitting parameters that express the correlation between the strut height and the brick length, and 'σ_b' is the brick strength along the principal loading direction of the wall and is calculated from Eq. (2.5).

$$\sigma_b = \left[\frac{(\sigma_{bh} \,.\, \sigma_{bv})^2}{(\sigma_{bh} \,.\, Cos\gamma_1)^2 + (\sigma_{bv} \,.\, Sin\gamma_1)^2} \right]^{1/2} \qquad (2.5)$$

in which 'σ_{bh}' and 'σ_{bv}' are the ultimate compressive strengths of brick in the horizontal and vertical direction, and 'γ_1' is the angle of inclination of the compression strut with the vertical.

Mehrabi et al. (1994) studied a diagonal strut model and used plastic analysis to determine the ultimate capacity of RC frames infilled with masonry. They found that Eq. 2.6 developed from an equivalent diagonal strut model proposed by Smith and Carter (1971) predicted the ultimate capacity well.

$$V_u = w_d \; f_m \; \cos \gamma_1 \qquad (2.6)$$

in which 'w_d' is the effective width of compression strut, 'f_m' is the mean compressive strength of masonry, and 'γ_1' is the angle of inclination of the compression strut with the vertical.

Shing et al. (1991) have also shown that the reinforced masonry shear walls exhibit diagonal failure. The racking load imposes a shear force that causes the vertical reinforcement at the heel of the wall to act in tension and the masonry along the diagonal as a strut and the succeeding grouted cores behave as a compression member.

Shing et al. (1993a) proposed a method to calculate the shear resistance of RM shear walls from three major mechanisms. Parameters involved in these mechanisms are shown in Fig. 2.9.

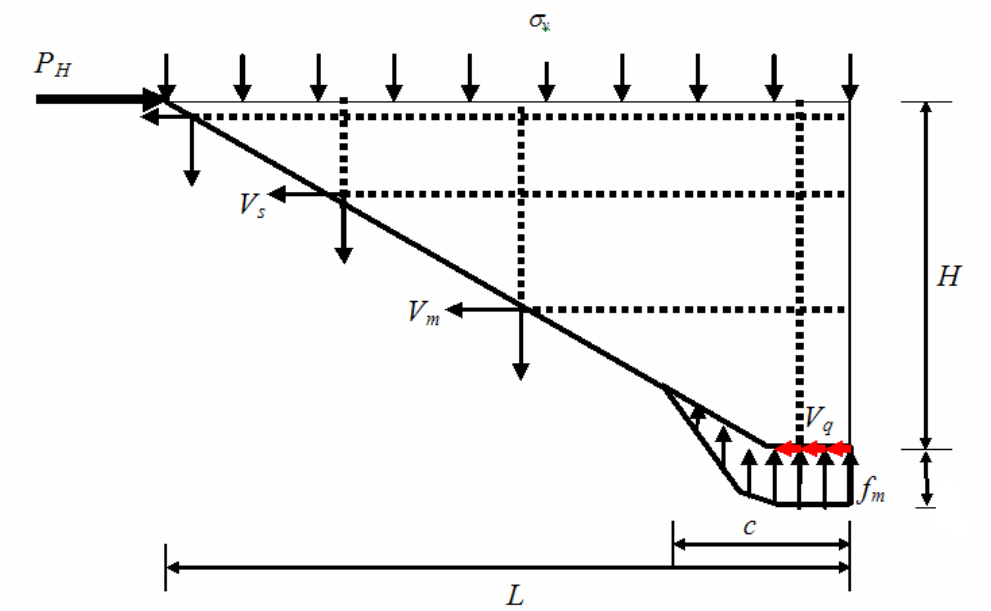

Figure 2.9: Diagonally cracked WSRM shear wall (Shing et al. (1993a))

The first mechanism is the resistance developed at the compression toe of the wall (V_q). It depends upon the compressive stress at the toe and the compressive strength of the masonry. The second mechanism is the shear resistance of masonry and the dowel action of vertical steel across a diagonal crack (V_m). The third mechanism is tensile resistance from the horizontal reinforcement across a diagonal crack (V_s). These parameters are calculated from Eq. 2.7.

$$V_m = C_3 \left(C_4 \rho_V f_{yv} + \sigma_v \right) A_g$$
$$V_s = C_5 \left(\frac{L - 2d'}{s} - 1 \right) A_h f_{yh} \qquad (2.7)$$
$$V_q = C_1 f_m \left(1 - C_2 \frac{\sigma_v}{f_m}\right)^{0.5} A_g$$

in which 'A_g' is gross area of the wall ($t_w \times L$), 'd'' is the distance of the extreme vertical steel from the nearest edge of the wall. 'C_1' represents the percentage of the total wall area effective in resisting shear at the compression toe. 'C_2' is a multiplier of vertical compressive stress. 'C_3' is the coefficient of friction along the crack. 'C_4' and 'C_5' are the coefficients to account for the yielding of horizontal and vertical steel respectively. All these coefficients were calibrated with finite element analysis. Using the imperial units, Shing et al. (1993a) found the values of

coefficients 'C_1', 'C_2', 'C_3', 'C_4', and 'C_5' through finite element analyses equal to 0.04, 4.5, 0.25, 0.667 and 0.75 respectively.

Seah and Dawe (1997) developed a computer programme for the analysis of the masonry infilled panels. Elastic-plastic behaviour of frame elements and nonlinear behaviour of in-fills were incorporated in the programme. The programme predicted the load-displacement response of the bare frame well; however, the load-displacement response of the frame elements filled with masonry did not show any softening although it was evident in their experiments.

To predict the shear capacity of partially reinforced masonry (PRM) shear walls, different equations have been proposed by several researchers (Ingham et al. (2001), Matsumura (1987), Shing et al. (1990a), Okamoto et al. (1987)). Shing et al. (1990a) determined the flexural capacity and ductility of squat PRM shear walls by means of simple flexure theory. Fattal (1993b) compared the effectiveness of several equations proposed by Matsumura (1987), Shing et al. (1990b), Okamoto et al. (1987), and UBC (1988) in predicting the ultimate shear capacity of PRM shear walls. They found that the equation proposed by Matsumura (1987) was the closest predictor of ultimate strength although it showed some inconsistency. Correlation provided by the equation of Matsumura (1987) was close for high strength walls but could not predict the shear strength of low strength walls, horizontally reinforced walls, URM walls and PRM shear walls. Fattal and Todd (1993) modified Matsumura's equation for calculating the shear capacity of the PRM walls. This modified equation is explained in Chapter 5 to investigate its effectiveness for predicting the shear capacity of the WSRM walls considered in this thesis.

2.5.2 Failure of RM Shear Walls

Fattal and Todd (1993) reported that the failure of RM shear walls could occur due to tensile cracking and yielding of vertical bars in high flexural zones, tensile shear cracking induced near

the centre of the wall, propagation of shear cracks to form rupture planes, or yielding of steel and crushing of masonry in compression at the loaded corners. However the occurrence of these events depends upon the amount and spacing of reinforcement, the aspect ratio of the wall, the level of axial stress, and the compressive strength of the masonry.

In an experimental study, Ingham et al. (2001) found that all PRM walls exhibited a diagonal tension mode of failure whereas the grouted walls exhibited rocking mode of failure. Through experimental studies, Faella et al. (1994) and Ingham et al. (2001) concluded that the PRM walls having vertical reinforcement positioned at a maximum spacing of 800mm exhibit ductile behaviour. As the failure of WSRM remains not well understood, this research project aims at investigating the complete nonlinear behaviour of the WSRM walls.

2.6 Review of Experimental Studies

Masonry walls of varying sizes and different vertical and horizontal reinforcement ratios with varying horizontal and vertical spacings have been tested in various parts of the world. An overview of such experiments is provided in this section. The outcomes of the investigations regarding these walls found from these studies and from other studies available in the literature are discussed in section 2.7.

2.6.1 New Zealand Studies

In New Zealand, research has been carried out mostly on investigating the behaviour of fully reinforced masonry shear walls (Priestley (1977), (1982)). Recently Ingham et al. (2001) have reported the behaviour of partially grouted lightly reinforced masonry walls subjected to inplane cyclic loading. They have reported the response of 12 partially reinforced masonry walls of constant height and varying thicknesses and lengths. Typically these walls were 2.4m high, 0.8m to 4.2m long and 90mm to 140mm thick. All walls contained vertical reinforcement bars (12mm

diameter) at horizontal spacing of 800mm. Dimensions and reinforcement details of these walls are shown in Fig. 2.10.

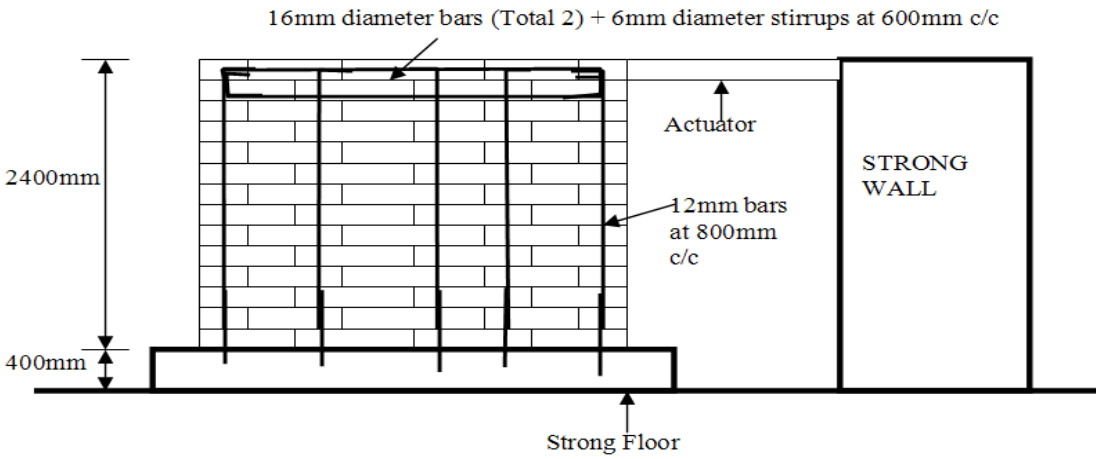

Figure 2.10: Masonry walls tested in New Zealand (Ingham et al. (2001))

All walls were tested without vertical compression. Horizontal cyclic loading was applied on top of the walls via a 150×75 steel channel, which was fastened to the top of the bond beam through the actuator supported by the strong wall. They found that the partially grouted masonry having vertical reinforcement at maximum horizontal spacing of 800mm could show ductility of 2.0.

2.6.2 American Studies

Fattal (1993b) has reported a research plan for investigating the behaviour of masonry shear walls from experimental studies, numerical methods and finite element analyses. Schultz (1994) has provided an outline of experiments for partially grouted masonry shear walls tested at the building and fire research laboratory of the National Institute of Standards and Technology of U.S. Department of Commerce and Technology Administration. In this report, design details of 42 concrete/clay masonry walls of constant height (1422mm) and thickness (203mm) but with varying lengths (2845mm, 2032mm, 1422mm) have been outlined. Varying lengths of the walls resulted in three (0.5, 0.7, 1.0) aspect ratios. For all these walls, masonry blocks were laid in face shell bedding using 'S' type mortar (conforming to ASTM (1989)). All these walls had two post-

tensioned #6 (284mm^2) hot rolled reinforcement bars in the end cores and two post-tensioned #6 (284mm^2) hot rolled reinforcement bars in the intermediate cores as shown in Fig. 2.11.

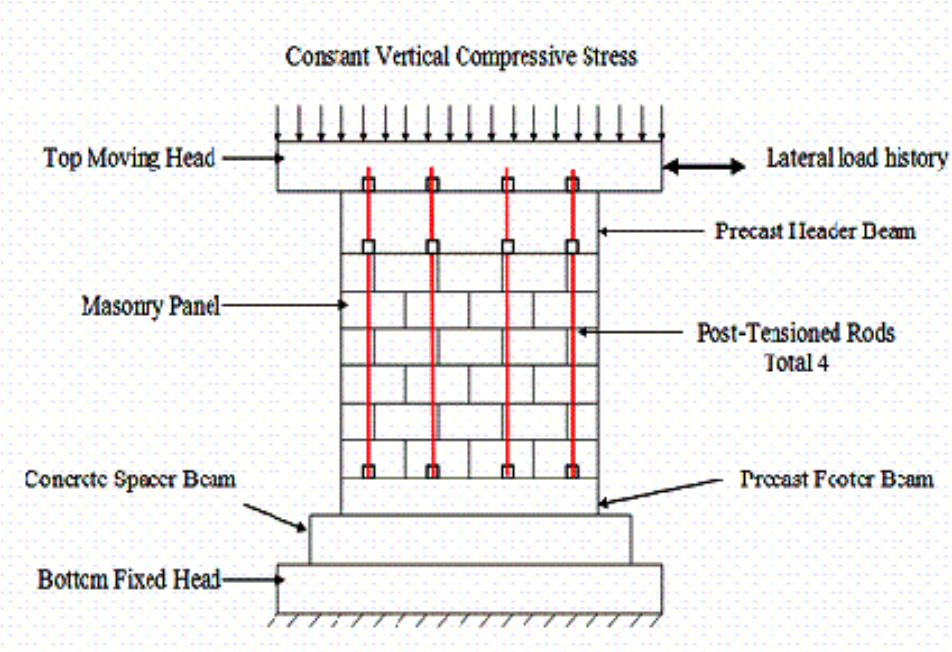

Figure 2.11: Masonry walls tested in United States of America (Schultz (1994))

Schultz (1994) also reported the influence of the aspect ratio of the walls, the horizontal reinforcement and the axial compression to the shear capacity of the walls. This report used the results of the experimental studies conducted by Fattal (1993a), Shing et al. (1990a), NEHRP (1994) and UBC (1988). From this study, it was found that with the increase of the aspect ratio (0.5 to 1.0) of the masonry shear walls, the shear capacity reduced on average by approximately 55%; with the increase of the horizontal reinforcement ratio (0 to 0.21%) the shear capacity increased on average by approximately 55%; and with the increase of the axial compression (0 to 2.75MPa), the shear capacity increased on average by approximately 25%.

2.6.3 Japanese Studies

Matsumura (1987) has reported the behaviour of fully and partially reinforced masonry shear walls investigated from experiments. For this study, 57 concrete masonry walls and 23 clay

masonry walls were constructed and tested. The main focus of this study was to investigate the effect of the vertical compression, the horizontal reinforcement and failure mode of the walls. These walls had varying lengths, heights and thicknesses. Length of these walls varied from 0.4m to 2.0m, height from 0.6m to 1.8m and thickness from 100mm to 190mm. Geometry and typical reinforcement details of these walls are shown in Fig. 2.12.

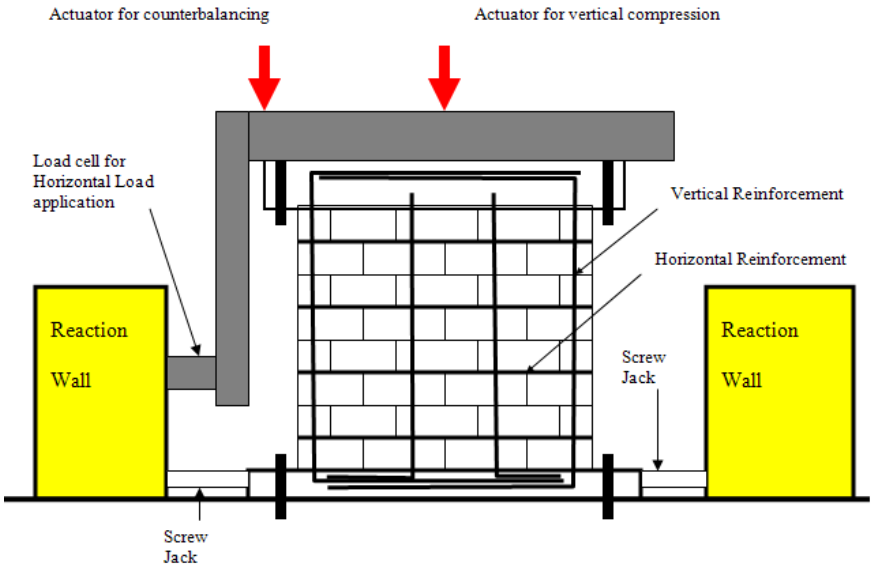

Figure 2.12: Masonry walls tested in Japan (Matsumura (1987))

These walls contained D10 (10mm diameter) horizontal reinforcement bars at the vertical spacing of 400mm and D29 (29mm diameter) or D22 (22mm diameter) vertical reinforcement bars at varying horizontal spacing. These walls were tested under cyclic loading. From this study, it was found that the shear capacity of the partially or fully grouted masonry walls increased at a rate of approximately 0.2 times the vertical stress and approximately proportional to $\sqrt{\rho_h \cdot f_{yh} \cdot f_m}$ where 'f_{yh}' is the yield strength of the horizontal reinforcement, 'ρ_h' is the horizontal reinforcement ratio and 'f_m' is the mean compressive strength of masonry.

2.7 Factors Affecting the Behaviour of Shear Walls

From the literature, it has been found that the load-deformation response and failure patterns of the shear walls are affected by various factors. Reinforcement, vertical compression, aspect ratio and material properties are some of the main parameters that significantly affect the behaviour of the shear walls. This section describes these parameters.

2.7.1 Reinforcement

Percentage and location of reinforcement play an important role in the behaviour of RM shear walls. Alcocer and Meli (1995) found that the amount of horizontal reinforcement does not affect the initial stiffness of walls, although horizontally reinforced walls resist higher forces than unreinforced walls. Several researchers (Ingham et al. (2001), Khattab and Drysdale (1993), Hamid (1991)) observed that the lateral load capacity of the shear walls does not increase significantly but the ductility increases by increasing the quantities of steel reinforcement. Fattal (1993a) has reported that cracking deformations as well as the ultimate capacity of RM walls increase with increasing horizontal reinforcement ratio up to 0.2%. Benli and Houqin (1991) have found that the horizontal reinforcement increases the shear capacity of brick walls up to 30% as compared with that of the unreinforced walls.

Priestley (1977) has reported that uniformly distributed reinforcement in RM shear walls helps avoid problems with bond and anchorage in compression associated with the practice of providing bundled reinforcement at the wall ends. The author had also found that well-distributed reinforcement along the length of the wall provides better crack control and improved dowel shear resistance across the potential sliding plane.

In most of the above-mentioned studies, the percentage of reinforcement was kept high and the spacing of steel bars was kept lower than 800mm. Clearly the state-of-the-art of the masonry

shear wall research could not define the failure/behaviour of WSRM walls, therefore, the current research is undertaken to investigate the behaviour of WSRM shear walls.

2.7.2 Axial Compression

Axial compressive stress significantly affects the behaviour of the URM walls (similar to structural columns). Several researchers (Fattal (1993a) , Alcocer and Meli (1995), Bernardini et al. (1997)) have observed that a small increase in vertical load provides the walls with a larger strength and ductility due, perhaps, to the improvement of bond resistance mechanisms between mortar and masonry units (especially in the URM). A substantial increase of axial stress changes the failure mode of the wall from flexure to shear. It has also been found by several researchers (Alcocer and Meli (1995), Davidson and Brammer (1996), Assa and Dhanasekar (2000)) that very high axial compression reduces the available ductility of the structure. Ghanem et al. (1993) have found that to avoid the brittle failure of masonry, vertical stress should not be more than 5% of its compressive strength.

WSRM walls are also used as partitions in apartment buildings and as boundary walls for houses where they do not carry axial load (excluding self weight) in their service. Their behaviour under such conditions is investigated in this research project.

2.7.3 Aspect Ratio

Aspect ratio of walls (H/L) plays an important role in the failure mode; therefore its effect must be incorporated in the equations that predict the shear capacity and deformations. Brunner and Shing (1996) devised an analytical method to determine the shear capacity of RM shear walls of different aspect ratios. Their method was formulated from the equilibrium of both the horizontal and the vertical forces as shown in Fig. 2.9. Fattal (1993a) has found that the aspect ratio in the range of 0.75-2.5 remarkably affects the ultimate capacity; however shear deformations are not

affected by the aspect ratio in this range. In an experimental study, Davidson and Brammer (1996) found that for the squat walls (H/L=0.6), shear tends to dominate the flexural behaviour.

The effect of aspect ratio to the failure pattern of shear walls is shown in Fig. 2.13. For tall walls, a 45^o crack occurs in the lower part of the walls exhibiting flexural failure as shown in Fig. 2.13(a). For walls with aspect ratio close to unity (Fig. 2.13(b)) a major diagonal crack intersects the base in the compression zone and part of the vertical force is transferred directly from the wall to the base at the compression toe. The remaining portion of the vertical force is transmitted across the diagonal crack, which leads to aggregate-interlock forces.

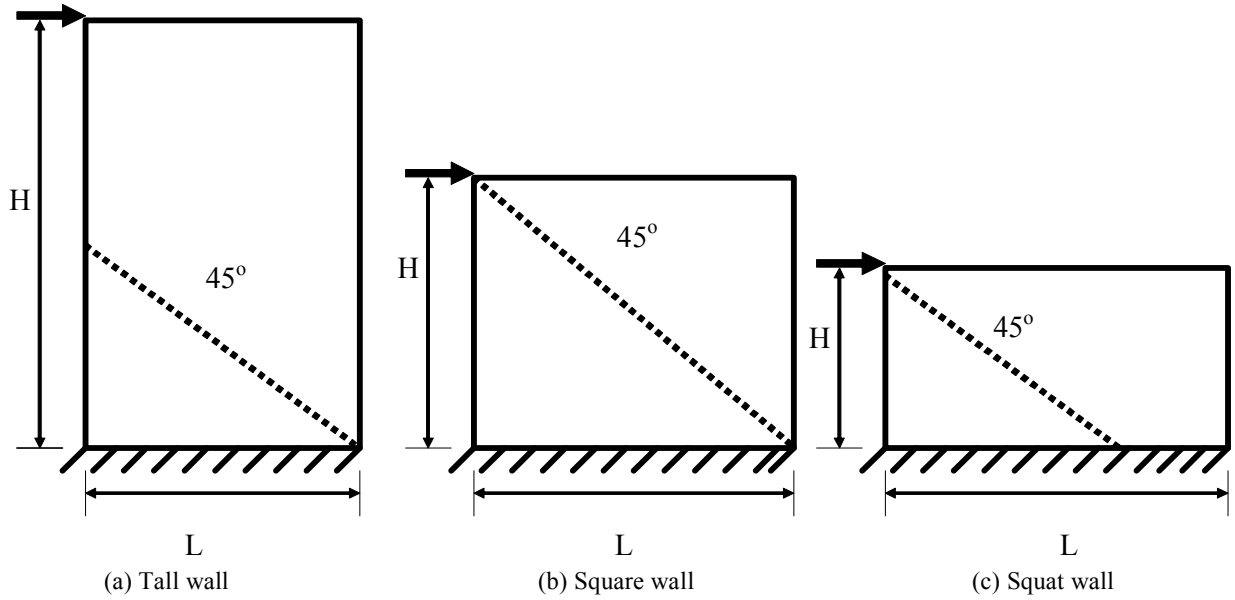

Figure 2.13: Orientation of diagonal cracks in masonry shear walls (Shing et al. (1990a))

For walls of H/L<1 (see Fig. 2.13(c)), the diagonal crack originates at the upper corner of the wall and meets the base outside the stress block, and the entire area bounded by the compressive block becomes effective in providing shear resistance at the compression toe.

The effect of aspect ratio on the behaviour of WSRM shear walls is not well understood, especially the contribution of the intermediate reinforced cores; the study presented in this thesis investigates the effect of aspect ratio on the behaviour of WSRM shear walls.

2.7.4 Material Properties

It has been found by several researchers that the strength of mortar and grout has *limited* effect on the strength of walls (Drysdale and Hamid (1979a), Scrivener and Baker (1988)). Riddington and Naom (1994) found that an increase in brick tensile strength results in an increase in the ultimate compressive capacity of walls. Zhuge (1995) reported that tensile strength of masonry has significant influence on cracking and hence the ultimate load capacity of URM walls only when the vertical compressive load is relatively low, and this effect becomes insignificant when the vertical compressive stress is high.

Hansen et al. (1998) have found that the use of stronger mortar does not generally improve the shear properties of bed joints, however in some cases stronger mortars do increase the shear strength but they lead to brittle failure of masonry. Drysdale and Hamid (1979a), Riddington and Naom (1994) have reported that the increase in thickness of mortar joints decreases the ultimate compressive strength of masonry. Riddington and Naom (1994) have considered mortar nonlinearity in addition to the tensile strengths of brick and mortar, and tensile and shear strengths of brick-mortar interface in their FE program to predict the capacity of brickwork.

2.8 Material Characteristics of Masonry

For macro modelling, masonry is considered as an orthotropic material without any need to define the properties of the constitutive materials. Some important properties of masonry are, therefore, provided in this section.

2.8.1 Compressive Strength

Compressive strength of masonry (f_m) is affected by the properties of mortar, units and grout and is usually obtained from prism tests. AS3700 (2001) provides a table to calculate the

compressive strength of masonry from the compressive strength of masonry units and the type of mortar, which can also be used conservatively where testing of prisms is not possible.

The stress-strain curves of the masonry under uniaxial and biaxial compression exhibit nonlinearity. Stress–strain behaviour of masonry determined by various researchers under uniaxial and biaxial compression is discussed in this section.

2.8.1.1 Uniaxial Behaviour

Boult (1979) carried out an experimental program to examine the effect of the strength of the masonry constituents, aspect ratio of the wallettes and shape of the masonry units. He used concrete masonry units of lightweight and normal weight, grout of different compressive strength and different shapes of masonry units in the construction of masonry wallettes of different heights. He found that the profile of the masonry units had little effect on the prism strength; however, he reported that to obtain optimum compressive strength of the grouted masonry, the compressive strength of the masonry units and the grout should be approximately equal to each other. A similar conclusion was obtained independently by Drysdale and Hamid (1979a) and Kumar (1995) in two separate programmes on the compressive strength of grouted and ungrouted masonry.

Drysdale and Hamid (1979a) tested 146 grouted and ungrouted masonry prisms and reported that the concept of superposition of the strengths of the grout and the hollow masonry prism was not valid due to incompatibility of the deformation characteristics of the grout and the masonry units (large lateral expansion of the grout leads to premature tensile splitting failure of masonry units). The behaviour was further explored with respect to clay block masonry by Kumar (1995).

2.8.1.2 Biaxial Behaviour

The constitutive behaviour of masonry under biaxial state of stress cannot be completely described from the uniaxial constitutive behaviour under uniaxial loading conditions. Due to the orthotropic nature of masonry, biaxial stress state cannot be described solely in terms of principal stresses, therefore a biaxial strength envelope of masonry needs description in terms of the full stress vector in a fixed set of material axes or in terms of principal stresses and the orientation angle 'θ' between the principal stresses and the material axes. Page (1981), Page (1983) and Dhanasekar et al. (1985b) reported failure surfaces of masonry suitable to uniaxial tension and or compression and biaxial tension and or compression. Similar studies were also carried out by Ganz and Thurlimann (1982). Strength envelopes and possible modes of failure of solid masonry are presented in Figs. 2.14 and 2.15 respectively.

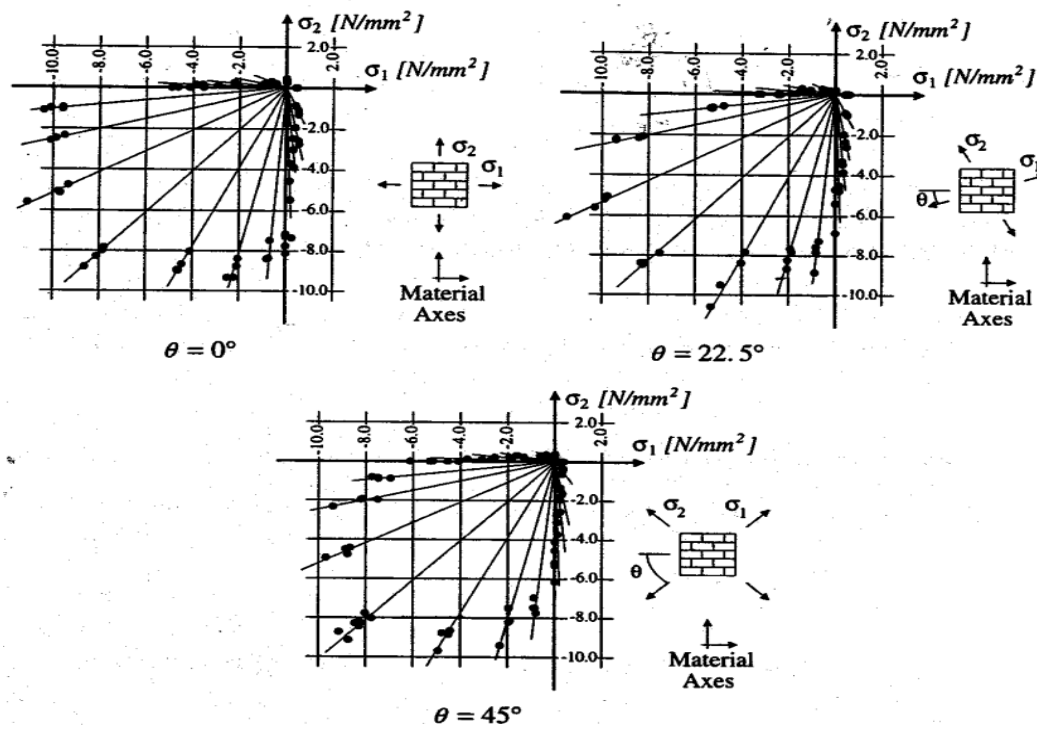

Figure 2.14: Biaxial strength of masonry (Page (1981), Page (1983))

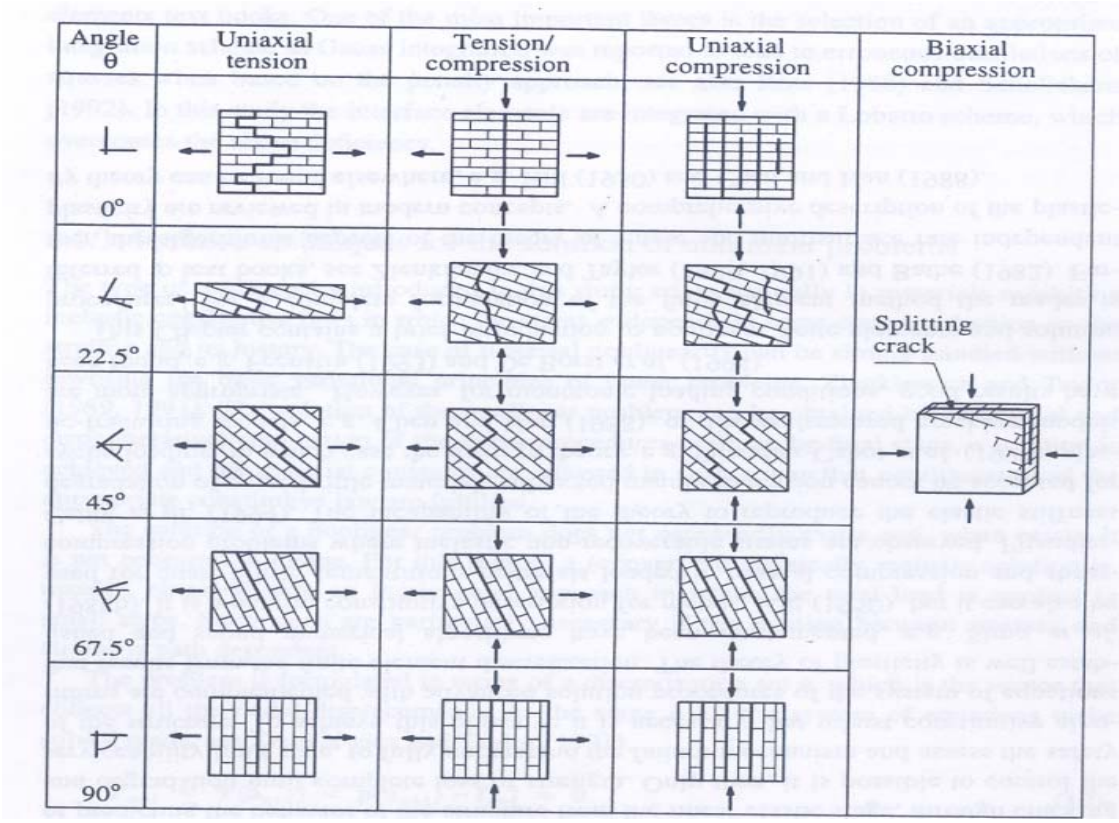

Figure 2.15: Modes of failure of masonry under biaxial loading (Dhanasekar et al. (1985b))

Under uniaxial tension, failure occurred through cracking and sliding of the vertical and the horizontal mortar joints. Under tension-compression loading, failure occurred either by cracking and sliding of the joints or in a combined failure of masonry units and mortar joints. Biaxial compression failure occurred due to splitting of specimens at mid-thickness, in a plane parallel to its free surface, regardless of the orientation of the principal stresses.

Naraine and Sinha (1992) have conducted a series of experiments and developed empirical formulae for predicting the envelope curves of the masonry under cyclic compressive loading. Based on the experimental studies, they defined two points namely the common point and the stability point. A typical stress strain curve of masonry tested under cyclic compressive loading is shown in Fig. 2.16(a).

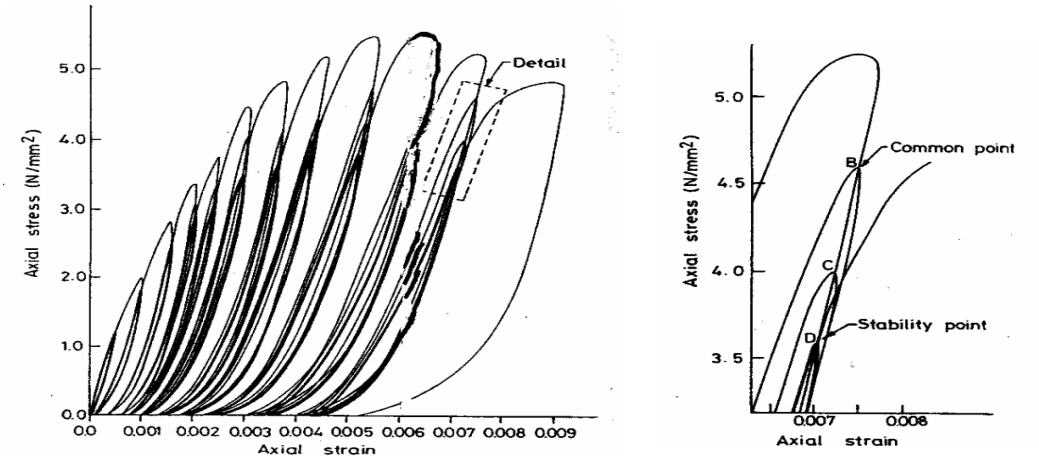

(a) Complete loading history (b) Common and stability points

Figure 2.16: Stress-strain of masonry under cyclic loading (Naraine and Sinha (1992))

The common point was the uppermost point of intersection of a reloading curve with the unloading curve of the previous cycle whereas the stability point was the point of intersection of the reloading curve with the initial unloading curve as shown in Fig. 2.16(b). The empirical equations could predict the envelope, the common and the stability point curves. Naraine and Sinha (1989) have reported that the envelope curve under cyclic loading coincided with the stress-strain curve under monotonic loading.

2.8.2 Modulus of Elasticity

Several equations have been reported in the literature to calculate the modulus of elasticity of masonry (E_m) such as Knuttson and Nielsen (1995) and Kornbak (2000). However most commonly, 'E_m' is calculated from the characteristics compressive strength of masonry (f_m) as Eq. (2.8).

$$E_m = X f_m \tag{2.8}$$

where 'X' is a factor that varies from 500 to 1000 depending upon the type of mortar and bricks used in masonry. In AS3700 (2001), it is equal to 1000 when general-purpose mortar M3 (1:1:6)

and clay units of unconfined compressive strength more than 30MPa are used. Drysdale and Gazzola (1991) also found its value equal to 1000 for masonry which they tested in their experimental work.

Several researchers have proposed stress strain relationships for masonry. Naraine and Sinha (1992) proposed equations for cyclic loading. Dhanasekar et al. (1997) proposed equations for grouted masonry under monotonic and cyclic loading. Priestley and Elder (1983) have found that stainless steel confining plates in mortar beds result in a more gradual falling branch to the stress strain curve. In a comparative study, Hamid (1997) found that concrete masonry and clay masonry exhibit somewhat different stress-strain curves. Therefore he recommended that the parameters required for design (modulus of elasticity, strain at peak stress, and stress parameters) should be appropriately determined for each type of masonry.

2.8.3 Shear Strength

In order to predict the shear capacity of masonry walls, knowledge of masonry shear strength is required. Measuring the pure shear strength of masonry joints is a difficult task. Over the years many different test methods such as the couplet (Hansen et al. (1998)), the triplet (Hamid et al. (1978), Van der Pluijm (1993)) and the diagonal tests ((Frunzio et al. (1995) , Khalaf and Naysmith (1997)) have been devised. Jiang and Xiao (1994) developed an apparatus shown in Fig. 2.17 to determine the shear strength of a masonry joint.

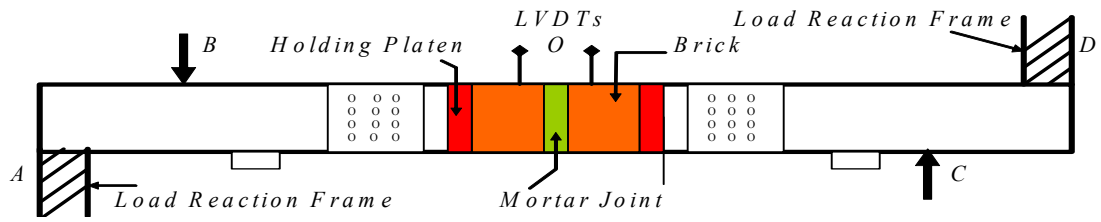

Figure 2.17: Measurement of shear strength of a masonry joint (Jiang and Xiao (1994))

According to this procedure the bricks were glued to the specimen-holder platens. The left and the right parts of the specimens were then joined with a mortar joint. After curing, the platens were bolted to the left and the right aluminium plates. Equal load was applied at points 'B' and 'C' that caused relative displacement of the two bricks. The loading frame was supported at two ends ('A' and 'D') and the deformation in the mortar joint was measured using LVDT's as shown at location 'O'. With the help of a Finite Element Model, Jiang and Xiao (1994) found that the shear stress along the mortar joint was uniform.

Jukes and Riddington (1997) tested a variety of methods to determine the masonry joint strength and concluded that the triplet test with precompression was the most appropriate and simple one. This test has become a European standard test. A schematic diagram for this test is shown in Fig. 2.18.

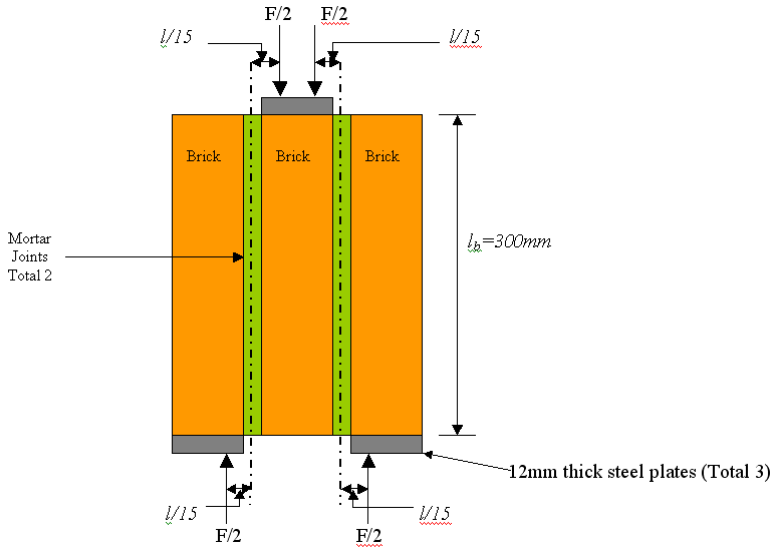

Figure 2.18: Schematic diagram of triplet test

To achieve the shear strength from this triplet test, the triplet is loaded in a manner such that minimum bending is applied. To meet this requirement, load is applied via rollers at the positions indicated in Fig. 2.18. A value of 'l/15' is used in practice with small masonry units such as British clay bricks.

2.8.4 Tensile Strength

Tensile strength of masonry plays an important role in the failure of the masonry shear walls. Some researchers have attempted to investigate the true tensile strength of unreinforced masonry. For example, Backes (1985) tested masonry wallettes under direct tension and found that tension failure was affected by the type of the mortar and the masonry units. For stronger mortar and weaker masonry units the tension cracks passed along the head mortar joints and through the centre of the bricks at the intervening courses as shown in Fig. 2.19(a).

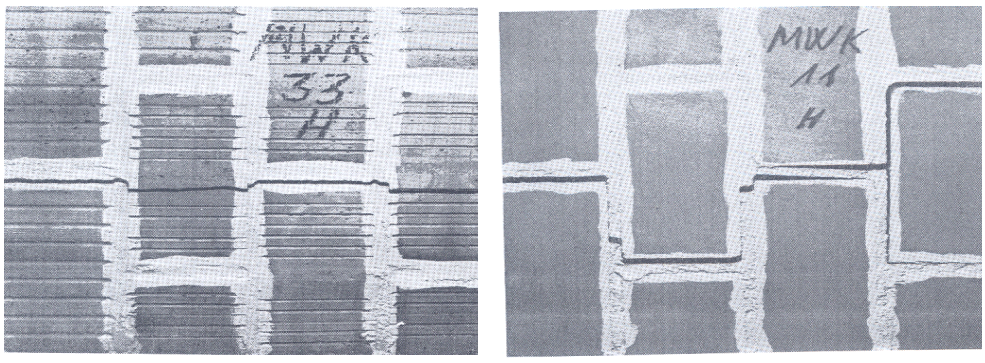

(a) Through type (b) Zigzag type

Figure 2.19: Modes of tension failure of masonry walls under direct tension (Backes (1985))

For weaker mortar joints and stronger masonry units, the tension crack passed along the head joints of the masonry units and the length of bed joints between staggered head joints as shown in Fig. 2.19(b). The author found that the direct tensile strength of masonry wallettes was ranging from 0.09MPa to 0.82MPa depending upon the tensile strength of mortar and the masonry units. Drysdale et al. (1979b) found that the tensile strength of both the grouted and ungrouted masonry varied with the orientation of applied stress due to the anisotropic nature of masonry. They concluded that the type of the mortar had little effect on the tensile strength of ungrouted masonry, and the grouting contributed the maximum when the tensile stresses were applied normal to the bed joints and provided no contribution when the tensile stresses were applied parallel to the bed joint.

2.8.5 Mechanical Properties of Masonry Collected from Literature

Material properties of masonry (for example Young's modulus, Poisson's ratio, maximum compressive and tensile strength of masonry and strain at maximum (peak) compressive strength) collected from a wide range of literature are presented in Table 2.1.

Table 2.1: Properties of masonry and its constituents collected from different sources

Author	Material	Young's Modulus MPa	Poisson's Ratio	Mean Compressive Strength MPa	Tensile Strength MPa	Ultimate Strain at Maximum Stress
Middleton et al. (1991)	Clay Units	11000	0.20	52	2.6	-
	Mortar	2200	0.25	14	2.4	-
Mehrabi and Shing (1997)	Concrete Units	-	-	16.0	-	-
	Masonry	6380	-	12.9	-	0.0031
	Masonry	14650	0.16	-	-	-
Vermeltfoort et al. (1993)	Clay Units	8000	-	10.34	0.15	-
	Concrete Units	-	-	14.5	0.5	0.0025
Correa and Page (2001)	Concrete Units	8026	0.25	22.0	-	-
	Mortar	10,900	0.20	9.5	-	-
	Grout	30,000	0.20	-	-	-
Cheema and Klingner (1986)	Concrete Units	12828	0.28	25.9	-	0.0021
	Masonry	5172	-	15.5	-	0.0023
	Mortar	-	0.28	13.5	-	-
	Grout	24828	0.37	27.3	-	0.0021
Kumar (1995)	Clay Units	-	-	36.0	-	-
	Masonry	12915	0.25	19.9	-	0.0024
	Grout	27500	-	32.5	-	0.0017
Riddington and Naom (1994)	Clay Units	22000	0.15	62.0	-	-
	Mortar	9944	0.20	13.6	2.60	-
Ali and Page (1988)	Clay Units	14700	0.16	15.3	2.20	0.0027
	Mortar	7400	0.21	7.3	0.11	0.006
Page (1978)	Clay Units	5900 -7550	0.17	36.3	-	-
	Mortar	-	-	3.2	-	-
Dhanasekar et al. (1985a)	Masonry	5700	0.19	9.85	-	-
	Clay Units	-	-	15.41	-	
	Mortar	-	-	5.08	-	-

2.9 Failure Theories

Theory of plasticity, failure criteria for most commonly used materials, and failure surfaces of masonry are reviewed in this section.

2.9.1 Review of Theory of Plasticity

Most engineering materials respond elastically at lower load levels but, when the load exceeds the yield limit, they exhibit plastic behaviour which is modelled using plastic theories. There are two types of plastic theories; one is *incremental* type in which the mechanical strain rate is decomposed into an elastic part and a plastic part; the other is *deformation* type in which the stress is defined from the total mechanical strain. Incremental type plasticity is most commonly used and is modelled in terms of a *yield surface*, a *flow rule* and *evolution laws*. The yield surface generalises the concept of *yield load* into a test function that can be used to determine that the material responds purely elastically at a particular state of stress. The flow rule determines the inelastic deformation that occurs when the material does not respond purely elastically. The evolution laws define the *hardening* in which the yield surface increases its size during the course of inelastic deformations.

The stress state at a point is represented by a second order symmetric tensor as shown in Eq. 2.9.

$$\begin{bmatrix} \sigma_x & \tau_{xy} & \tau_{zx} \\ \tau_{xy} & \sigma_y & \tau_{yz} \\ \tau_{zx} & \tau_{yz} & \sigma_z \end{bmatrix} \tag{2.9}$$

where 'σ' is the normal component and 'τ' is the shear component of the stress state. The average value of all normal components ($(\sigma_{nx} + \sigma_{ny} + \sigma_{nz})/3$) of a stress tensor is called the mean stress, also known as *hydrostatic stress* (σ_{hyd}). The *deviatoric stress tensor* is obtained by

subtracting the hydrostatic stress tensor from the stress tensor. It plays an important role in the theory of plasticity. Principal stresses and principal deviatoric stresses are calculated from characteristic Eq. (2.10) and Eq. (2.11) respectively.

$$\sigma^3 - I_1\sigma^2 + I_2\sigma - I_3 = 0 \tag{2.10}$$

$$s^3 - J_1 s^2 - J_2 s - J_3 = 0 \tag{2.11}$$

where 'I_1', 'I_2', 'I_3' are the first, second and third invariants of the stress tensor and are calculated from the principal stress components ($I_1 = \sigma_1 + \sigma_2 + \sigma_3$, $I_2 = \sigma_1\sigma_2 + \sigma_2\sigma_3 + \sigma_3\sigma_1$, $I_3 = \sigma_1\sigma_2\sigma_3$). '$J_1$', J_2', J_3' are the first, second and third invariants of the deviatoric stress tensor and are calculated from the deviatoric stress components ($J_1 = s_1 + s_2 + s_3$, $J_2 = ½ (s_1^2 + s_2^2 + s_3^2)$, $J_3 = s_1\, s_2\, s_3$) where 's_i' are the shear stresses in three planes.

2.9.2 Most Commonly Used Failure Criteria

Different yield criteria have been developed to simulate the behaviour of different materials. Most commonly used criteria are Tresca, Von Mises, Rankine and Mohr-Coulomb. The Tresca criterion states that yielding of a material occurs when the maximum shearing stress at a point reaches a critical value, which is equal to ½ the compressive strength for a uniaxial test and 'τ_o' for a shear test. The Von Mises criterion states that yielding of a material occurs when the maximum shearing strain energy at any point of a material reaches a critical value. Since the shear strain energy is proportional to the second invariant the deviatoric stress tensor, J_2, the criterion is expressed as:

$$J_2 - k^2 = 0 \tag{2.12}$$

From a uniaxial tension test, the constant 'k' is determined as '$\sigma_o / \sqrt{3}$' and for a pure shear test 'k' is taken equal to 'τ_o'. σ_o is the strength under uniaxial test. Fig.2.20 (a) and (b) show the Von Mises yield surface on the principal plane and σ-τ plane respectively.

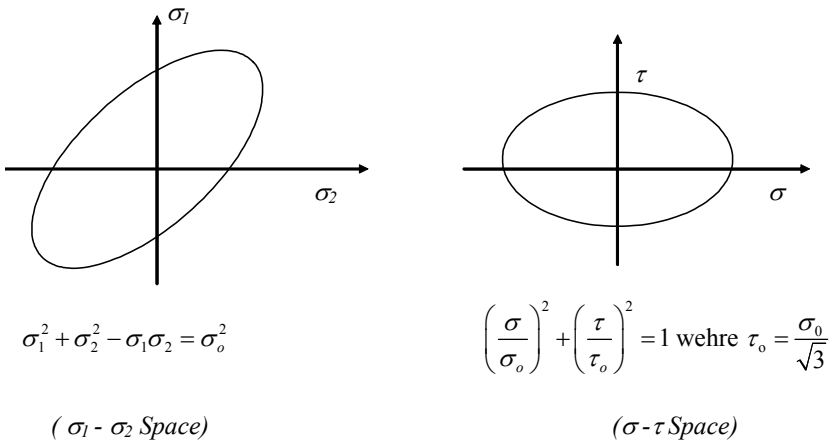

Figure 2.20: Von Mises criterion

The Mohr-Coulomb criterion used for many civil engineering friction type materials assumes the critical value of shearing stress on a plane to be a function of normal stress acting on the same plane. The yield surface given by Mohr-Coulomb criterion is shown in Fig. 2. 21.

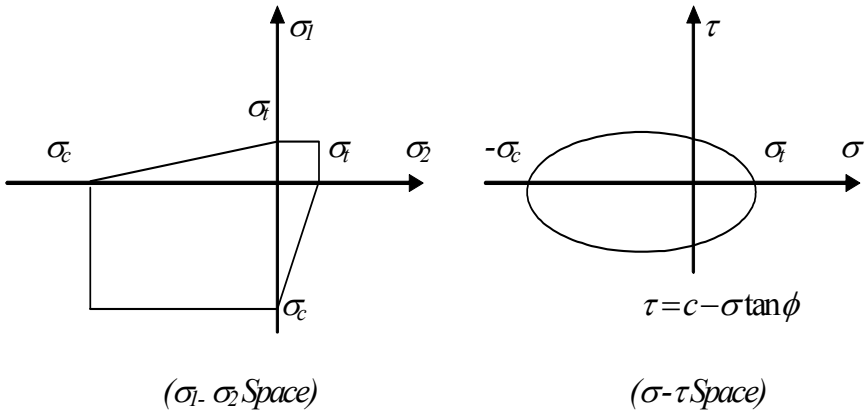

Figure 2.21: Mohr-Coulomb criterion

In Fig. 2.21, 'σ_1' and 'σ_2' are principal stresses, 'σ_t' is the tensile yield stress in the uniaxial tension and 'σ_c' is the compression yield stress in the uniaxial compression test, 'c' is the cohesion and 'Ø' is the angle of internal friction, 'σ' and 'τ' are the normal and shearing stress respectively.

2.9.3 Failure Surfaces in 3D Stress Space

Since masonry is a brittle material like concrete, various attempts have been made in the past to use the conventional concrete failure (smeared crack model) criterion for masonry with slight modifications. Originally Lotfi and Shing (1991) and then Ibrahim and Suter (1994) used the smeared crack model to determine the strength and failure mechanism of fully reinforced masonry (RM) shear walls. They found that the flexural response of the RM shear wall could be accurately reproduced, but the brittle shear behaviour dominated by diagonal cracking could not be realistically captured due to kinematic constraints on crack opening, an inherent limitation of the smeared crack approach.

More recently Maleki et al. (2005) have investigated use of the smeared crack model for the analysis of reinforced masonry shear walls. They have found that the smeared crack model predicted the behaviour of the flexure dominated RM walls; however, the model was not very effective for the shear dominated RM walls.

The masonry walls in the above three studies were fully grouted and fully reinforced. The researchers were able to ignore the mortar joints because the bulk of the masonry walls consisted of homogeneous isotropic material in grouted cores and a high amount of uniformly distributed reinforcement material along the length of the wall. For the WSRM walls, which contain large regions of unreinforced masonry and very small reinforcement at large spacings (up to 2000mm), effectiveness of the smeared crack model is yet to be investigated.

In reality, masonry is an orthotropic material due to the presence of mortar joints. The conventional smeared crack model cannot realistically predict the behaviour of unreinforced masonry. Towards this end, attempts have been made by various researchers (Yokel and Fattal (1976), Hamid and Drysdale (1981), Page (1982), Dhanasekar et al. (1985a)) in the past to develop a failure criterion which incorporates the effect of orientation of mortar joints.

Page (1982) tested half scale brickwork specimens with five different bed joint angles with ten different load-combinations and developed different failure surfaces in terms of two principal stresses at different bed joint orientation. He emphasised that a single failure surface, which includes the effect of orientation of mortar joints, needed to be derived.

Towards this end, Dhanasekar (1985) first developed a single three dimensional failure surface to predict the various kinds of failure of masonry in principal stress space (σ_1, σ_2, θ) and an alternative stress system (σ_n, σ_p, τ). This failure surface in principal stress space is shown in Fig. 2.22.

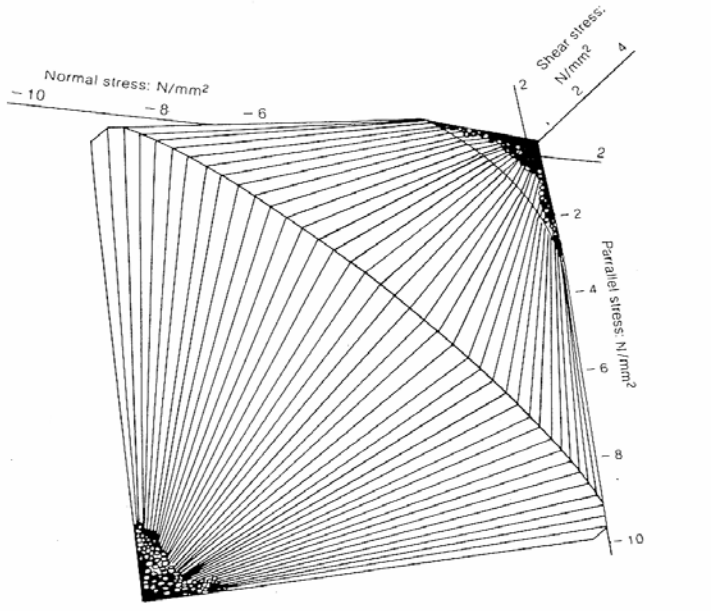

Figure 2.22: Failure surface for masonry (Dhanasekar (1985))

Zhuge (1995) produced an anisotropic plasticity material model for masonry by embedding mortar joints in Mohr-Coulomb masonry units to allow failure in either the masonry units or along the mortar joints depending upon the material properties of the masonry units and the mortar joints, the stress state and the angle of orientation of the mortar joints. This model is shown in Fig. 2.23.

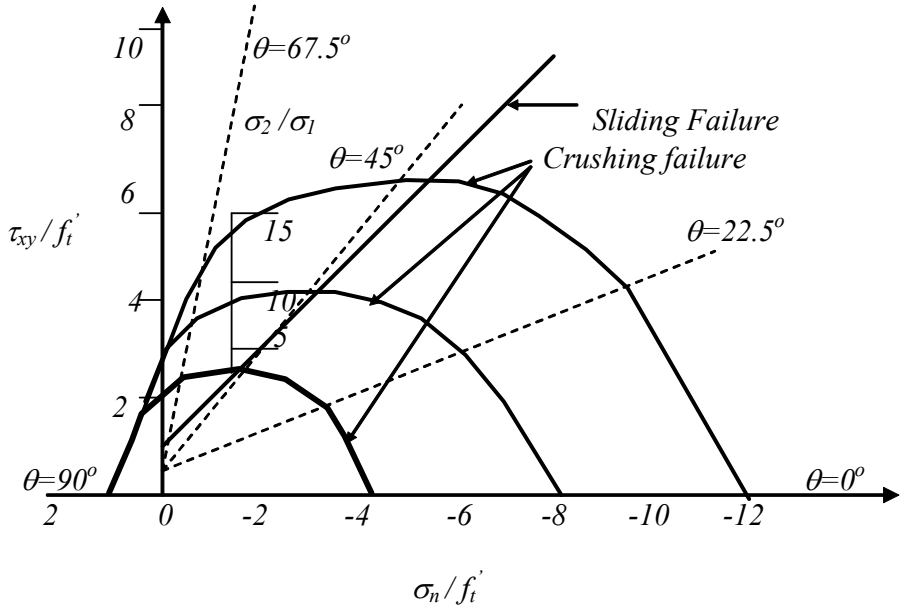

Figure 2.23: Failure envelopes for masonry (Zhuge (1995))

In Fig. 2.23, when orientation of bed joints (θ) ranges from 90° to 45°, masonry resists the low ratio of 'σ_n/τ' and the failure occurs due to bond failure along the joints. When 'θ' is decreased, the shear capacity of the wall increases as 'σ_n' increases; and when $\theta < 45^o$, shear strength exceeds the principal tensile strength and the failure is controlled by the biaxial failure criterion, and the failure mode changes from shear sliding to tensile cracking. In Fig. 2.23, 'f_t' is the uniaxial tensile strength of masonry and 'σ_n' is the axial stress normal to the bed joints.

The above-mentioned failure models consisted of complex yield surfaces and were unable to predict the complete nonlinear behaviour. Lourenco (1996) developed a material model for

masonry that combined the modern plasticity concepts (hardening, softening, flow rule and evolution laws) with an anisotropic behaviour along each material axis. Use of this material model (Lourenco (1996)) will be attempted in this thesis to investigate the behaviour of WSRM shear walls. A brief description of this material model is given in Chapter 6 of this thesis.

2.10 Design Principles of Masonry Shear Walls

Behaviour of reinforced masonry shear walls and partially reinforced masonry shear walls has been investigated by several researchers (Priestley and Elder (1982), Okamoto et al. (1987), Matsumura (1990), Fattal and Todd (1993), Pilakoutas and Elnashai (1995), Tomazevic et al. (1996), Brunner and Shing (1996) and Bernardini et al. (1997)) . There is a wealth of information on URM shear walls in the literature (Page (1978), Dhanasekar and Page (1987) , Samarasinghe et al. (1981), Soroushian et al. (1988), Mahmoud et al. (1995), Zhuge et al. (1996), Lafuente et al. (1998), Vermeltfoort et al. (1993), Zhuge (1995), Lourenco (1996), Bosiljkov et al. (2003)). Research on the behaviour of PRM shear walls has also been conducted to some extent (Benli and Houqin (1991), Davidson and Brammer (1996), Ghanem et al. (1993), Ingham et al. (2001)) whereas research on wide spaced reinforced masonry (WSRM) shear walls is limited to the author (Haider and Dhanasekar (2004)).

Many codes of practice of masonry including the Australian Standard for masonry AS3700 (2001) ignore the contribution of vertical reinforcement towards the shear capacity of the PRM walls when horizontal reinforcement is not provided. This assumption could be considered as overly conservative.

Present practices for design of WSRM walls in Australia are based on equations available (Clause 8.6.2) in AS3700 (2001). This clause outlines the requirement of the reinforcement for the WSRM walls subject to inplane shear loading. This clause accounts for the contribution of

the horizontal reinforcement but not the vertical reinforcement. In the absence of horizontal reinforcement, the code directs the designer to analyse the walls as URM walls. WSRM walls resist the inplane horizontal and vertical loading due to unit-mortar interlocking, vertical reinforcement and horizontal reinforcement if provided.

Equations available in various codes of practice for masonry structures (CSAS304.1 (1994), BS5628 (1992), ENV-1996-1-1 (1995), UBC (1988)) have been reviewed and it has been found that each equation lacks one or more factors that realistically affect the shear capacity of the WSRM walls.

Like the Australian masonry code, British and Euro and UBC masonry codes ignore the contribution of the vertical reinforcement in the WSRM walls and treat them as URM walls. The shear capacity of the WSRM walls is calculated only by shear bond strength and friction strength of the shear section. The Canadian masonry code considers the contribution of the vertical reinforcement in the shear strength of masonry walls; however, this code does not consider the effect of the aspect ratio of the shear walls, which critically affects the behaviour of the shear walls. In the American Uniform Building Code (UBC), a relationship between the aspect ratio and the panel shear strength exists; however, contribution of the vertical reinforcement to the shear capacity is ignored.

Toscan (2001) has used the equations discussed above for the calculation of shear capacity of WSRM walls and found that none of these equations predicted the shear capacity effectively of the WSRM walls with different aspect ratios. He attempted truss analogy available for reinforced concrete shear walls (Warner et al. (1999)) for determining the shear capacity of the WSRM walls by assuming isotropic masonry material along the diagonal of the walls. This method over estimated the shear capacity, however, the author found that the failure mode of the WSRM walls resembles that of a truss system.

The Australian Standard for masonry structures (AS3700 (2001)) provides a prescription for a simplified design of masonry for small buildings. In clause 12.3.5.3.1, AS3700 (2001) requires vertical reinforcement at corners, and at both sides of openings. One of the prescriptive designs provided by AS3700 (2001) is presented in Fig. 2.24. This design relates the reinforcement details with the wind and earthquake categories. Detailed information on the wind and earthquake categories can be found in Australian Standards for wind loading for housing (AS4055 (2006)) and earthquake loading (AS1170.4 (1993)) respectively.

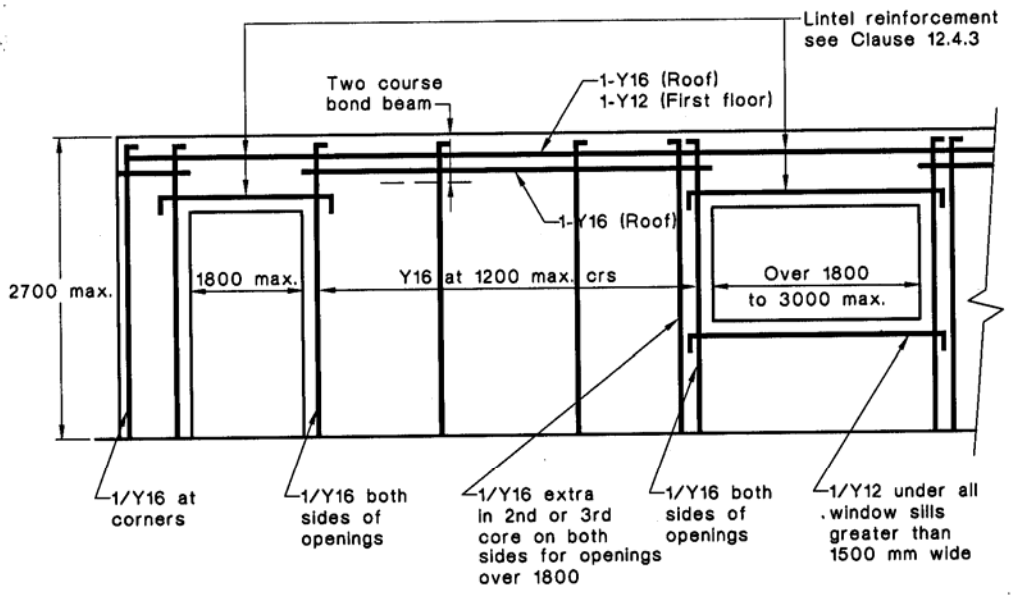

Figure 2.24: Reinforcement details for a masonry wall suitable for wind categories N4, C2

As per these designs, masonry walls contain horizontal and vertical reinforcement for two heights (2700mm and 3000mm), one thickness (190mm) and selected categories of wind and earthquakes. These figures also put limits on the detail of the reinforcement applicable to certain lengths. To the best knowledge of the author, these figures have been presented based purely on practical experience. A comprehensive research study is required to develop realistic design principles which could be applicable to masonry shear walls of various aspect ratios, design of

the horizontal and the vertical reinforcement, taking account of the effect of vertical compression on the walls and able to be used for masonry of different types (clay or concrete). This study was aimed towards this end and research has been carried out accordingly. The effect of the vertical reinforcement, aspect ratio and the vertical compression on the behaviour of the WSRM walls will be investigated in this thesis.

2.11 Finite Element Modelling of Masonry Shear Walls

Finite element models provide cost effective solutions compared to the experimental alternative, but true success of numerical techniques heavily depends on a well-validated constitutive model for the material used and appropriate discretisation of the continuum.

Masonry is highly anisotropic due to the presence of discrete sets of horizontal and vertical mortar joints. Brick masonry has orthotropic strength and softening characteristics, which depend not only on the properties of masonry units and mortar but also on their interaction reflecting the workmanship. Based on these considerations, researchers (Saadeghvaziri and Mehta (1993), Lourenco (1996), Papa (2001), Jager and Schops (2004)) have divided models for masonry into two categories: micro and macro. In micro models, masonry units and mortar are separately discretised using continuum or discrete elements, whereas in the macro model (also known as equivalent material model), masonry is modelled as a single material using average properties of masonry.

Page (1978), and Ghosh et al. (1994) concluded that macro modelling could predict the deformations satisfactorily at low stress levels and inadequately at higher stress levels when extensive stress redistribution occurs. Pande et al. (1990) categorically stated that macro modelling would not accurately predict the stress distribution within the bricks and mortar

In micro modelling, two approaches are followed in finite element analyses. In the first, both the bricks and the mortar joints are discretised by using continuum finite elements, whereas in the second approach interface elements are used to model the behaviour of mortar joints. Several researchers (Papa (2001), Lotfi and Shing (1994), Lourenco and Rots (1997), Shing and Cao (1997)) have reported that the interface elements used in heterogeneous models reproduce essentially the interaction between two adjoining masonry units, and further degrees of freedom are not required to be introduced.

For masonry walls subjected to either vertical load (only) or a combined shear and vertical loading, 2-D analyses are found effectively producing stress results that are close to those produced by 3-D analyses. Riddington and Naom (1994) concluded that the plane stress analyses generally produce results closer to 3D results than that produced by plane strain analyses. Dhanasekar and Xiao (2001) proposed a special 2D element and validated its results using a 3D model of masonry prisms. Naom (1992) showed that two-dimensional and three-dimensional elements produce similar horizontal inplane and shear stress for brick piers subjected to a uniformly distributed load of 1MPa.

2.11.1 Unreinforced Masonry Walls

To determine the internal stress distribution in URM, Page (1978) modelled joints as linkage elements in conjunction with units as plane stress continuum elements. Bricks were assumed isotropic and elastic. Nonlinear behaviour of masonry was considered to occur only due to nonlinear deformation and failure characteristics of joints. Nonlinear deformation characteristics of joints were determined indirectly from the tests performed on masonry prisms by substituting elastic properties of units. A failure criterion for joint elements was developed in terms of normal and shear stress. Units and linkage elements were incorporated into an incremental finite element program. At a particular load level, iterative solutions modelling material nonlinearities were

obtained and joint elements were then checked for violation of the failure criterion. This process continued until convergence was achieved. Experimentally it was found that the final failure was due to failure of both masonry units and linkage elements, therefore a criterion for unit failure was found essential.

Dhanasekar et al. (1985a) proposed a macro model for solid masonry, which was capable of reproducing the effects of material nonlinearity and progressive local failure. URM was modelled as a continuum with average properties of brick and mortar with appropriate nonlinear behaviour of mortar included. Each element in the finite element mesh encompassed several masonry units and joints. The effects of local brick or joint failure were smeared across the portion governed by the Guassian integration points of the finite element. This technique enabled the efficient analysis of large panels but could not be used for the analysis of local effects.

To determine the internal stress distribution in masonry panels under concentrated loading, Ali and Page (1988) modelled the masonry units and mortar joints separately. They used four-noded quadrilateral elements with refined mesh in concentrated load regions to allow redistribution of stresses. Failure of bond as well as units and mortar was considered. They used strength criterion for crack initiation and propagation and smeared crack modelling technique for reproducing the effects of the cracks. To incorporate the cracking or crushing type of failure for bricks and mortar, they used the Von Mises failure criterion with tension cut off, and to predict the bond failure of the brick mortar interface they used a three-dimensional failure surface. This model allowed for the possible closing and reopening of cracks, as well as the formation of secondary cracks normal to the direction of the primary cracks.

To incorporate strain softening effects (in other words to avoid potential sudden redistribution of stresses), Ali and Page (1988) defined a descending branch of stress strain curve of masonry assemblage in their finite element model. They showed that an ultimate strain equal to six times

the cracking strain predicted the softening behaviour accurately. Ghosh et al. (1994) also used a value of ultimate strain equal to six times the cracking strain to match the experimental ultimate load.

Shing et al. (1993b) have concluded that for modelling the brittle shear behaviour of masonry walls; a discrete crack approach is essential, in which the mortar joint interface captures the development of the dominant shear crack. Hence they adopted the discrete crack approach to model the major diagonal crack by means of interface elements and secondary cracks by smeared crack elements. This approach requires knowledge on the crack path as a priori.

Riddington and Naom (1994) modelled mortar joints as interface elements with nonlinear material characteristics to predict the compressive strength of masonry panels. Khattab and Drysdale (1994) also formulated a homogeneous model of masonry with considerations of mortar joints as planes of weakness.

Lourenco et al. (1997) modelled masonry units as continuum elements while mortar joints and potential cracks in units were represented as zero-thickness interface elements. Interface elements were modelled with an interface cap model to include all possible failure mechanisms of masonry structures. These mechanisms included cracking in the joints, sliding along the bed and the head joints, cracking of masonry units in direct tension, diagonal tension cracking of masonry units at values of normal stress sufficient to develop friction in joints, and splitting of units in tension as a result of mortar dilatancy at high values of normal stress. This model reproduced the complete path of load-displacement until total degradation with minimal numerical difficulties.

Sayed-Ahmed and Shrive (1995) analysed face-shell bedded hollow masonry prisms subjected to concentrated loads by modelling face shells as discrete shell elements with orthotropic material characteristics using the smeared crack method, and web cracking and splitting as interface

elements using the discrete cracking method. The smeared crack model for orthotropic material was used to simulate the nonlinear material behaviour in the failure process. Cracking in units and mortar was modelled using the Mohr-Coulomb criterion. Interface elements were modelled using the Lagrange multiplier technique. Multipoint constraint equations were used to provide compatibility between continuum and shell elements. To define crack detection surface for units and mortar, material constants such as relationships of uniaxial tensile stress and uniaxial compressive strength, biaxial compression and biaxial tension-compression and ratio of tensile and compressive strengths were used in this study.

Ghosh et al. (1994) used ABAQUS to model solid masonry walls subjected to vertical and/or horizontal loads. Masonry was treated as a two-phase material in which the bricks and the mortar were modelled as a continuum and the contact between the bricks and mortar was modelled by interface elements. They used the inelastic constitutive model of concrete (see Appendix A) available in ABAQUS for both brick and mortar.

Due to lack of biaxial test results on brick and mortar, Ghosh et al. (1994) used the values of the ratio of ultimate strength in biaxial compression to ultimate strength in uniaxial compression (a_o) and the ratio of the total plastic strain in uniaxial compression to total plastic strain in biaxial compression (c_o) of concrete for both brick and mortar. For concrete these values are 2.16 and 2.28 respectively. Once values of 'a_o' and 'c_o' are selected, the values of yield stress in the state of pure shear stress (τ_p) and the hardening parameter (λ_c) can be determined from uniaxial test data. The fracture energies for bricks and mortar were obtained from Van der Pluijm (1992). Tensile strength of bricks and mortar were obtained from Ali and Page (1988).

Zhuge (1995) developed a two-dimensional plane stress element model for the non-linear analysis of URM shear walls. This model was developed using a homogeneous material model to predict the detailed load-deflection characteristics and critical limit states of URM walls under

inplane earthquake ground acceleration. Later Zhuge and Thambiratnum (1998) combined a two dimensional finite element model for nonlinear joint behaviour with an isotropic material model developed for reinforced concrete to analyse masonry subjected to inplane static and dynamic loading.

Among all the various modelling techniques reviewed in this section, a macro modelling technique developed by Lourenco (1996) showed capability of accurately predicting the behaviour of the URM shear walls until the walls showed large deformations, therefore, this modelling technique will be used in the analysis of the WSRM shear walls.

2.11.2 Fully Reinforced and Partially Reinforced Walls

To analyse reinforced masonry shear walls, Lotfi and Shing (1991) used the smeared crack approach for masonry and steel reinforcement. Uncracked masonry followed a plasticity model, cracked masonry an orthotropic material model and steel reinforcement an elastic hardening-plastic material. This model predicted flexure dominant behaviour but couldn't capture the brittle shear behaviour of RM walls because of an unrealistic kinematic constraint introduced by the smeared crack assumption. Later Shing et al. (1993b) used the discrete crack approach to model the major diagonal crack in a shear wall by means of interface elements and secondary cracks as smeared crack elements, which are caused by flexure as well as shear. This approach predicted the behaviour well but expected the location of the major diagonal crack to be known in advance.

Mortar joints are inherent planes of weakness in WSRM shear walls, and therefore, the failure of such walls is expected to be dominated by the fracture of these joints. The interface between the brick and the mortar is subjected to bond failure and friction.

Shing and Cao (1997) indicated that a smeared crack model alone cannot capture the brittle shear behaviour of RM walls and introduces additional problems in the analysis of WSRM shear walls.

They modelled PRM shear walls using plasticity-based interface elements for mortar joints and smeared crack elements for masonry units. The reinforcing steel was modelled as an elastic-hardening plastic material by means of a smeared overlay on top of the smeared crack elements. The compressive and tensile behaviours of masonry units were governed by a Von Mises failure surface with a Rankine type tension cut-off. The elastic-plastic interface model developed earlier by Shing et al. (1993b) was used to simulate the behaviour of mortar joints and vertical splitting of masonry units. They introduced interfaces at the middle of the masonry units to allow splitting of masonry units, which is often observed in actual tests but cannot be captured in a smeared crack model. The smeared crack model and the discrete crack model are reviewed in the following section.

2.12 Review of Conventional FE Models for Brittle Materials

Smeared crack and discrete models are conventionally used for the finite element analysis of brittle materials like concrete. The models are briefly discussed in this section.

2.12.1 Smeared Crack Model

The smeared crack approach is a convenient way to model tensile cracks in reinforced masonry structures and is computationally efficient because it does not require a large number of degrees of freedom to model crack propagation. In this technique, constitutive calculations are performed independently at each integration point of the finite element and the cracks are entered into calculations with each successive increment of loading.

The smeared crack approach models tensile cracks by transforming the material characteristics matrix to account for the crack induced with the axes of orthotropy '*n*' and '*p*' as shown in Fig. 2.25.

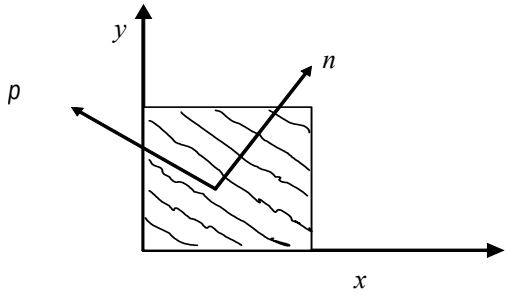

Figure 2.25: Smeared cracks

For a single crack, the incremental stress-strain relation can be expressed in the local n-p coordinates as

$$d\bar{\sigma} = D\, d\bar{\varepsilon} \tag{2.13}$$

In Eq. 2.13, the stress vector $\bar{\sigma}$ is $\{\sigma_n \;\; \sigma_{\mathrm{p}} \;\; \sigma_{\mathrm{np}}\}^T$ and strain vector $\bar{\varepsilon}$ is $\{\varepsilon_n \;\; \varepsilon_{\mathrm{p}} \;\; 2\varepsilon_{np}\}^T$. The stress-strain matrix 'D' for a cracked material is assumed to have the following form:

$$D = \begin{bmatrix} E_n & 0 & 0 \\ 0 & E_P & 0 \\ 0 & 0 & G \end{bmatrix} \tag{2.14}$$

In Eq. 2.14, 'E_n', 'E_P', and 'G' are the tangent moduli corresponding to the respective normal and shear strains, and the Poisson's effect is neglected. This change in 'D' significantly affects the stress state at the integration point, and the element subsequently re-distributes the stresses to the adjacent Gauss points or elements. This process involves significant iteration within the prescribed load or displacement increment.

2.12.2 Discrete Crack Model

Discrete crack models are used for interaction between two surfaces when the planes of weakness are known. Discrete crack elements are also known as joint elements or interface elements. Several researchers have used this method for modelling masonry joints (Page (1978), Dhanasekar (1985), Shing et al. (1993a), Shing and Cao (1997), Hossain et al. (1997)). Discrete elements were used either to model the mortar joints of masonry or contact between masonry and frames or the potential crack along the diagonal of masonry walls.

To model the plastic behaviour of a discrete crack, the relative displacement between two surfaces is decomposed into an elastic component (d_{elas}) and a plastic component (d_{plas}) as:

$$d = d_{elas} + d_{plas} \qquad (2.15)$$

in which $d = \{d_n \ \mathrm{d}_p\}^T$ where 'd_n' and 'd_p' are the relative normal and tangential displacements respectively. The elastic displacement is given as Eq. 2.16

$$d_{elas} = D^{-1}\sigma \qquad (2.16)$$

in which, $\sigma = \{\sigma \ \ \tau\}^T$, where 'σ' and 'τ' are the normal and tangential interface stresses respectively, and 'D' is a diagonal matrix of elastic constants. The yield criterion of the masonry joint developed by Lotfi and Shing (1994) is shown in Eq. 2.17

$$F(\sigma, q) = \tau^2 - \varphi^2(\sigma - f_t)^2 + 2\ rad\ (\sigma - f_t) = 0 \qquad (2.17)$$

in which 'f_t' is the tensile strength, and 'φ' is slope of asymptotes; '*rad*' is radius of curvature at the vortex of the hyperbola which is calculated from Eq. 2.18.

$$rad = (coh^2 - \varphi^2 f_t^2) / 2 f_t \qquad (2.18)$$

where '*coh*' represents cohesion of the joint.

2.12.3 Difficulties in Predicting Softening Behaviour of Materials

Kozar and Bicanic (1999) showed that the prediction of the softening regime of materials by the FE model could be wrong due to lack of regularisation of material behaviour. To achieve a single reliable physical path in the softening regime, a localisation limiter was used. The localisation limiter (weaker point) helped avoid localisation in zero volume and switching to a wrong solution path.

Rots (1988) studied the fracture behaviour of concrete and proposed a fracture energy concept for FE modelling for softening behaviour of concrete. This model used fracture energy, a characteristic length of the elements used in the mesh and Young's modulus of concrete. Since masonry has direction dependent material characteristics due to its orthotropic nature, the effectiveness of a single characteristic length for the fracture energy based model for masonry is unknown. This concept has not been tested for masonry and hence requires a detailed study. However, this fundamental research is outside the scope of this thesis and will not be conducted in this research program.

2.13 Summary

This chapter has presented a review of the behaviour of wide spaced reinforced masonry (WSRM) shear walls. Theory of shear walls and analysis of stresses in critical areas of the shear walls have been briefly discussed. Failure mechanisms of the shear walls under lateral inplane loading in the presence of axial compression have been reviewed.

Failure modes of the unreinforced masonry (URM), partially reinforced masonry (PRM) and fully reinforced masonry (RM) shear walls have been discussed. Analytical methods used for the analysis of the URM, PRM and RM in shear have been reviewed. Factors that significantly affect the behaviour of masonry shear walls have been included. Mainly these factors are the percentage of the horizontal and vertical reinforcement, axial compression, aspect ratio and material properties.

Failure modes, shear capacity equations and the effect of critical parameters on the behaviour of the URM, PRM and RM walls have been found in the literature; however, the response of the WSRM walls has been studied by the author only. For PRM walls, the spacing between the vertical reinforced cores is limited to 800mm, whereas in the WSRM walls, large areas of unreinforced masonry (up to 2000mm spacing between the reinforced cores) are expected. Behaviour of the WSRM walls is expected to be different and hence will be investigated in this thesis.

Material properties of masonry such as the compressive strength, the elastic modulus, the shear and tensile strengths have been reviewed to help with understanding the behaviour of the WSRM walls. Failure theories for different types of failures (tension, compression and friction) and the theory of plasticity have been reviewed to develop the finite element model for predicting the behaviour of the WSRM shear walls. Failure theories developed by various researchers for predicting the behaviour of masonry have also been reviewed.

Design principles provided in various codes of practice for design of masonry shear walls have been critically reviewed and their limitations discussed. Finite element modelling techniques used by different researchers for predicting the behaviour of the URM, PRM and RM shear walls have been discussed. In this thesis experimental investigations and finite element modelling techniques will be applied to evaluate the behaviour of the WSRM shear walls.

CHAPTER 3

WIDE SPACED REINFORCED MASONRY SHEAR WALLS – AN ELASTIC ANALYSIS

3.1 Introduction

This chapter discusses the elastic behaviour of the wide spaced reinforced masonry (WSRM) shear walls obtained from micro modelling analysis using a commercial finite element package ABAQUS. Techniques of discretisation and material characteristics used in the analyses are explained. This chapter aims at studying the stress distribution in the critical zones of shear walls that could lead to potential failure. The effects of the vertical grouted cores on the stress distribution at the critical zones and on the global behaviour of the WSRM walls are also reported.

3.2 Geometry of WSRM Shear Walls

WSRM walls contain reinforced grouted cores in the vertical direction at specified spacings and a bond beam at their top. When the walls contain grouted reinforced cores only at their ends, they are defined as end cores reinforced masonry (ECRM) in this thesis. When the wall contains no vertical reinforcement, it is defined as unreinforced masonry (URM). Fig. 3.1 shows details of the geometry of the WSRM, ECRM and URM walls.

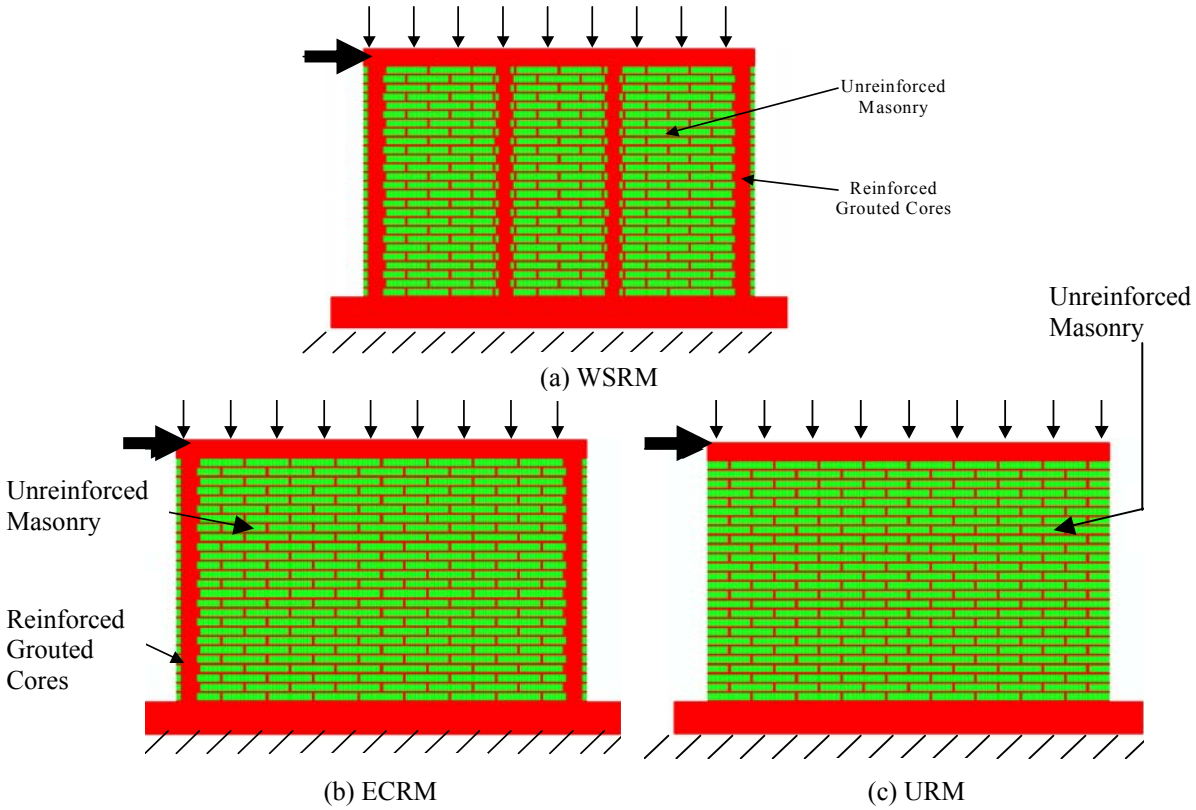

Figure 3.1: Geometry of WSRM, ECRM and URM walls

Masonry construction in typical running bond prevents continuity of planes of weakness in the vertical direction. Masonry units in alternate layers used in the construction of the three types of walls are shown in Fig. 3.2.

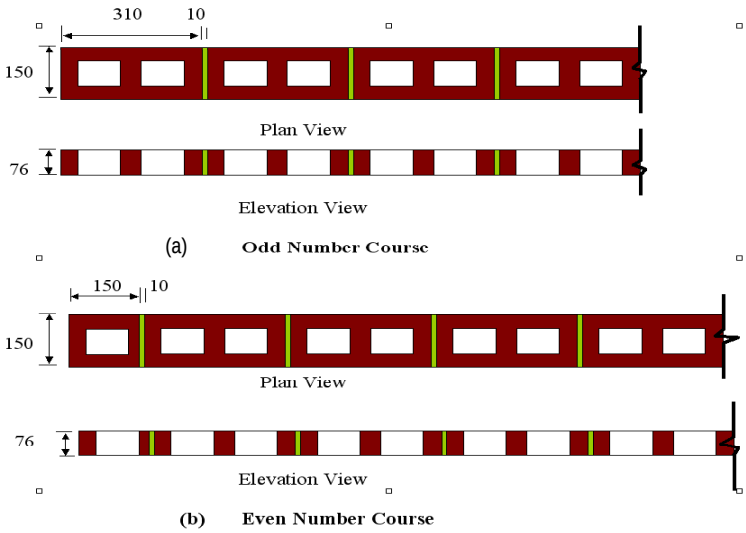

Figure 3.2: Alternate layers of hollow masonry units in the construction of masonry walls

3.3 Micro Modelling for Masonry Shear Walls

True representation of all constituent materials of the masonry walls is possible through the micro modelling technique. This technique requires discretisation of masonry walls into mortar, masonry units and grouted cores. As the analysis is focused on the elastic behaviour, interface bonds between the brick, the mortar and the grout, and the mortar and the brick shells are assumed to remain perfect throughout the loading stage. The model does not take account of pre-cracking and shrinkage effects as these are really long term issues.

3.3.1 Discretisation

For micro modelling, masonry walls were discretised into seven sections shown in Table 3.1.

Table 3.1: Sections of masonry walls for micro modeling

Section	Width (mm)	Comments
Mortar in the horizontal bed joints	70	Face shell bedding
Mortar in the vertical perpend joints	70	Face shell bedding
Mortar in the horizontal bed joints at edges of walls	150	Full bedding at the ends
Solid block sections	150	Solid parts of the masonry blocks
Hollow block section	70	Face shells of the masonry blocks
Section containing grout and mortar	150	80mm thick grout and 70mm thick mortar
Section containing grout and hollow masonry unit	150	80mm thick grout and 70mm thick face shells

As a common practice, face shell bedding was adopted in the construction of the walls. Width of both the horizontal bed joints and the vertical joints was taken equal to 70mm (35mm at each face shell of the masonry unit). The width of horizontal bed joints at the edges of the walls was taken equal to 150mm as the edge web shell is normally mortared. Solid and hollow sections of the masonry units were separated due to different width. The width of the solid and hollow sections was 150mm and 70mm respectively. The width of sections containing grout and mortar and grout and hollow masonry units was also 150mm.

In addition to the constituent materials for masonry walls, material properties for the bond beam and the base slab were also defined for the application of loading and effective boundary conditions. Elastic properties adopted for the analysis of the walls are provided in Table 3.2. For the elastic analyses of the WSRM walls, the effect of reinforcement was ignored; therefore no material properties for steel bars are included in Table 3.2. The data represent some typical values reported in the literature as summarised in Table 2.1

Table 3.2: Elastic properties for the elastic analysis of masonry walls

Constituent Material	Young's Modulus E (MPa)	Poisson's Ratio ν
Mortar	5000	0.20
Masonry Unit	40000	0.25
(Grout + Mortar)	13000	0.22
(Grout + Masonry Unit)	29300	0.22
Bond Beam	30000	0.25
Base Slab	35000	0.25

Elastic properties provided in Table 3.2 were selected based on the material test data reported in Table 2.1. Compressive strength tests were performed during this research work for the masonry units to determine their Young's modulus and Poisson's ratio values. The steel reinforcement was not included in the model as:

- The reinforcement becomes effective only after the cracking of masonry.
- The area of steel being so small (440mm^2) related to the area of cross-section of the wall.

Table 3.2 contains Young's modulus for the homogenised sections of *grout and mortar* and *grout and masonry unit*, which were calculated from Eq. 3.1 and Eq. 3.2 respectively.

$$E_{Grout-Mortar} = \frac{(E_{Grout} \times T_{Grout}) + (E_{Mortar} \times T_{Mortar})}{T_{Grout} + T_{Mortar}} \quad (3.1)$$

$$E_{Grout-Block} = \frac{(E_{Grout} \times T_{Grout}) + (E_{Block} \times T_{Block})}{T_{Grout} + T_{Block}} \quad (3.2)$$

where 'E' and 'T' represent Young's modulus and thickness of the corresponding sections. For grout, Young's modulus and thickness were equal to 20,000MPa and 80mm respectively.

The URM wall was modelled using the properties of mortar and masonry units whereas the ECRM and the WSRM walls were modelled using all materials listed in Table 3.2. All types of walls were provided with the properties of the bond beam and base slab. Fig. 3.3 shows discretisation of masonry walls into horizontal mortar joints, vertical mortar joints, vertical grouted cores, and the base slab.

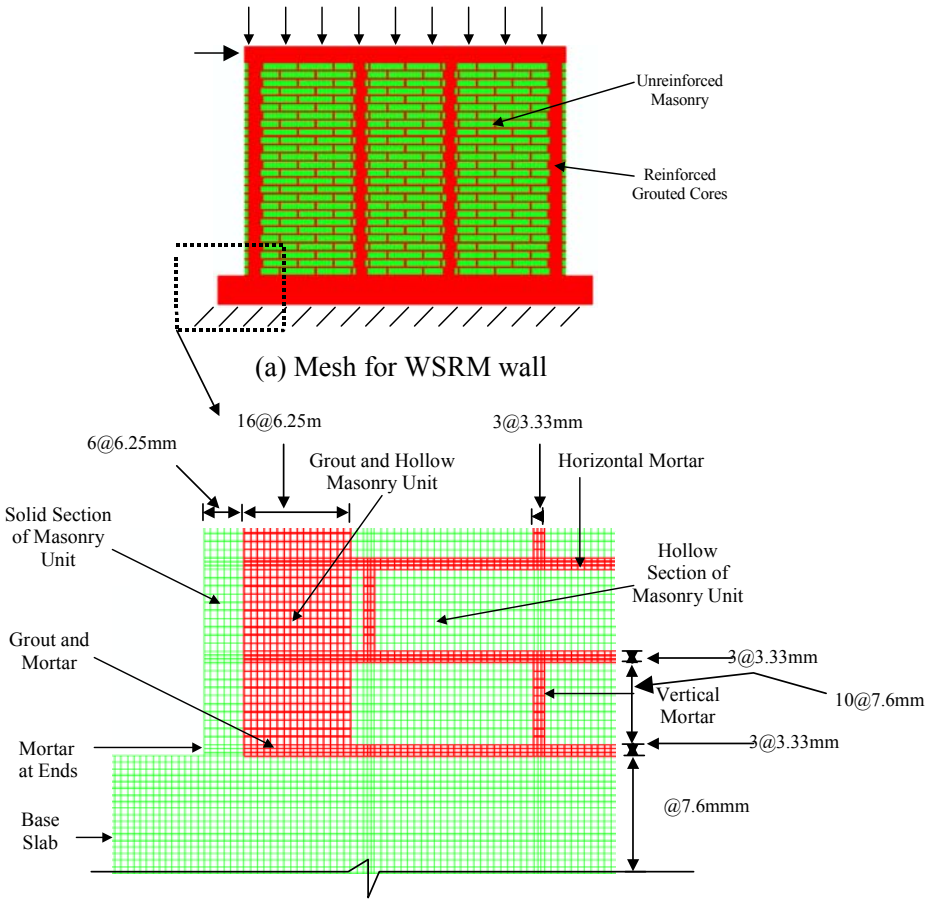

(a) Mesh for WSRM wall

(b) Section of Mesh

Figure 3.3: Mesh for micro modelling of WSRM shear wall

3.3.2 Meshing

To achieve appropriate/acceptable stress distribution in the masonry walls, a suitable meshing technique is required. For this purpose, a fine mesh was generated in which each 10mm thick mortar joint was discretised into 3 elements of equal thickness (3.333mm) with a view to obtaining better stress distribution in the mortar joints. The small size of elements in the thickness direction of mortar joints required the element size in the other direction to also be small so as to achieve the aspect ratio equal to a maximum of two. Hence the element size in the mortar joints was set equal to 3.333mm × 6.25mm whereas it was set equal to 6.25mm × 7.6mm for the masonry units (see Fig. 3.3). The same sized elements were used for the bond beam and the base slab.

To achieve the required size of elements in the mortar joints and for the masonry units, the total number of nodes and elements used in the analysis were equal to 204,940 and 203,962 respectively for modelling masonry shear walls of 2870mm length by 2408mm height, and the base slab of 3350mm length and 300mm thickness. A personal computer of normal workstation configuration took approximately 30 minutes to complete the analysis of these shear walls.

Fig. 3.3 shows an enlarged view of a section of the mesh of a WSRM wall. Bond between constituent materials was considered perfect, as the purpose of the analysis was only to examine elastic stress distribution. This helped avoid modelling of a complex bond using joint elements.

3.4 An Overview of Elastic Analysis Program

Plane stress elements are used for the analysis of the WSRM shear walls. The constitutive relation for linearly elastic and isotropic material for plane stress problems is given by Eq. 3.3.

$$\begin{Bmatrix} \varepsilon_x \\ \varepsilon_y \\ \gamma_{xy} \end{Bmatrix} = \begin{bmatrix} 1/E & -\upsilon/E & 0 \\ -\upsilon/E & 1/E & 0 \\ 0 & 0 & G \end{bmatrix} \begin{Bmatrix} \sigma_x \\ \sigma_y \\ \tau_{xy} \end{Bmatrix} + \begin{Bmatrix} \varepsilon_{x0} \\ \varepsilon_{y0} \\ \gamma_{xy0} \end{Bmatrix} \tag{3.3}$$

where 'ε_x', 'ε_y' and 'γ_{xy}' are the normal strains along the 'x' and 'y' directions and shear strain respectively. 'σ_x', 'σ_x' and 'τ_{xy}'are the normal stresses along the 'x' and 'y' directions and shear stress respectively. '*E*', 'υ'and '*G*' are Young's modulus, Poisson's ratio and shear modulus respectively. 'ε_{x0}', 'ε_{y0}' and 'γ_{xy0} are initial values of the normal strains along the x and y directions and shear strain respectively. To determine the stress vector 'σ', Eq. 3.3 can be rewritten as in Eq. 3.4.

$$\sigma = D\varepsilon + \sigma_0 \tag{3.4}$$

in which $\sigma_0 = -E\varepsilon_0$ and '*D*' is a material property matrix as shown in Eq. 3.5.

$$D = \frac{E}{1-\upsilon^2}\begin{bmatrix} 1 & \upsilon & 0 \\ \upsilon & 1 & 0 \\ 0 & 0 & (1-\upsilon)/2 \end{bmatrix} \tag{3.5}$$

Eq. 3.5 is valid only for plane stress problems in which $\sigma_z = \tau_{yz} = \tau_{xz} = 0$. ABAQUS makes extensive use of strain-displacement relations. Normal strain is defined as the change in length divided by original length and shear strain is defined as the amount of change in a right angle as shown in Fig. 3.4.

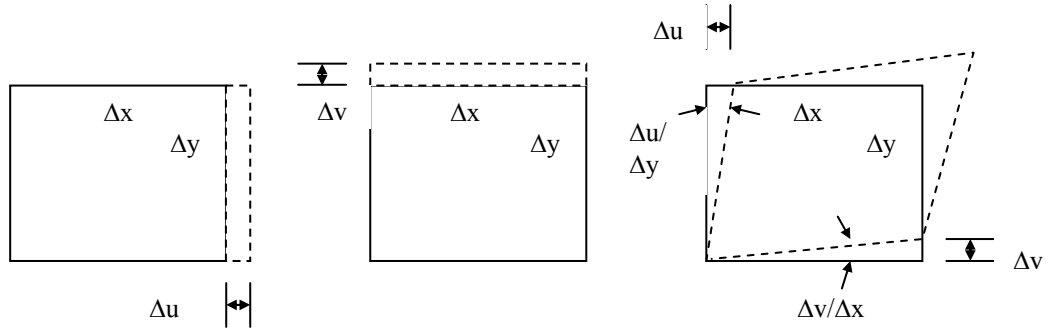

(a) x-direction strain (b) y-direction strain (c) Shear strain

Figure 3.4: Strain-displacement relations

The normal and shear strains shown in Fig. 3.4 can be calculated from Eq. 3.6.

$$\begin{Bmatrix} \varepsilon_x \\ \varepsilon_y \\ \gamma_{xy} \end{Bmatrix} = \begin{bmatrix} \partial/\partial x & 0 \\ 0 & \partial/\partial y \\ \partial/\partial y & \partial/\partial x \end{bmatrix} \begin{Bmatrix} u \\ v \end{Bmatrix} \quad or \quad \varepsilon = \partial \mathrm{u} \tag{3.6}$$

where the x-direction displacement 'u' and the y-direction displacement 'v' are both functions of the coordinates, $u = u(x, y)$ and $v = v(x, y)$ in a plane problem. Displacements 'u' and 'v' in a plane finite element are interpolated from nodal displacement 'u_i' and 'v_i' as follows:

$$\begin{Bmatrix} \mathrm{u} \\ \mathrm{v} \end{Bmatrix} = \begin{bmatrix} \mathrm{N}_1 & 0 & \mathrm{N}_2 & 0 & - - - \\ 0 & N_1 & 0 & N_2 & - - - \end{bmatrix} \begin{Bmatrix} u_1 \\ v_1 \\ u_2 \\ v_2 \\ - \end{Bmatrix} \tag{3.7}$$

where the 'N_i' are separate shape polynomials and 'N' is called the shape function matrix. Eq. 3.7 can be re-written in algebraic formats as shown in Eq. 3.8.

$$\varepsilon = \partial N d \quad \text{or} \quad \varepsilon = \mathrm{B}d \quad \text{where } \mathrm{B} = \partial N \tag{3.8}$$

Matrix 'B' is called the strain displacement matrix and 'd' is the displacement matrix.

3.4.1 Analysis Procedure

Restraining the bottom nodes in the horizontal and vertical directions simulates fixity of the base slab. Firstly, vertical load in terms of pressure was gradually increased on the top surface of the bond beam until it reached a maximum value of 0.5MPa (step-1) and then the horizontal displacement was applied at the top left corner of the bond beam (step-2). The horizontal displacement was increased to 0.3mm, which provided good insight into the stress distribution at the critical regions of the walls in addition to the overall deformation behaviour. As the analysis was limited to understanding of elastic behaviour, no further increase in horizontal load was considered essential.

In ABAQUS, initial time increment, time period of the step, minimum time increment and maximum time increment control the solution for static analysis of structures. In addition to these four parameters, the total number of increments can also be used to achieve better-controlled solutions. In the analysis of the shear walls, the period of the each step-time was set equal to 1.0 that allowed application of 0.3mm of horizontal displacement; the initial increment was set equal to 0.01 (or 0.003mm of horizontal displacement) at the first increment; the minimum time increment was set equal to 1.e-05 (or 3e-6mm of horizontal displacement). The program was allowed to control the solution automatically adjusting the increments suitably for achieving converged solutions within a minimum period.

ABAQUS provides two types of output data, namely field output and history output. In the field output components of stresses and strains for the whole model are extracted, whereas in the history output selected components (stresses, strains, displacements and energies etc.) for specified regions, or nodes or elements are extracted during the course of the analysis. For understanding of the stress distribution and potential failure mechanisms of WSRM walls, components of stresses and strains for elements in the critical regions and reactions force and

displacement at the nodes of load application were extracted for post processing. Results obtained from post processing of the extracted data are discussed in the following sections.

3.5 Results

The horizontal reaction forces at the loaded nodes were extracted from the history output data and their sum versus horizontal displacement for the loaded nodes of the WSRM, the ECRM and the URM walls is plotted in Fig. 3.5. A small increase in stiffness was observed from URM to WSRM walls depending on the number of thicker cores present.

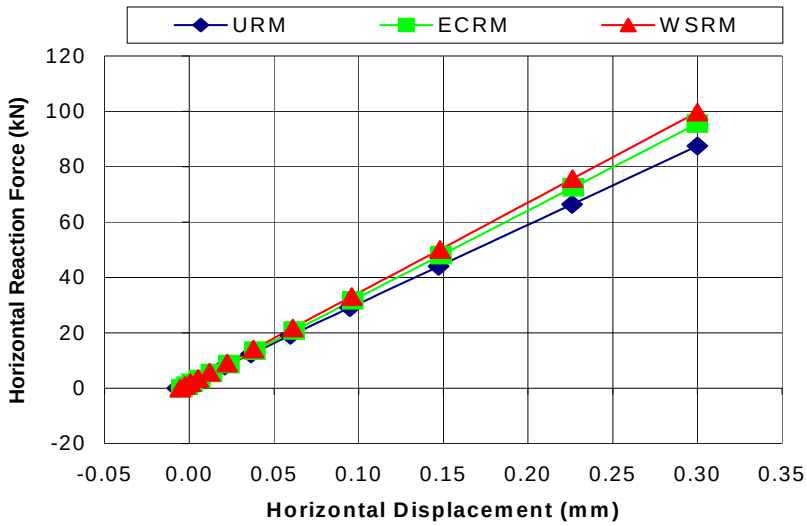

Figure 3.5: Load – Displacement response of WSRM, ECRM and URM walls.

To understand the elastic behaviour of the WSRM shear walls, different components of stresses namely the horizontal stress (S11), the vertical stress (S22), the shear stress (S12), the Mises stress, the maximum principal stress and the minimum principal stress were studied in different regions of the walls. Among all these stresses, shear stress (S12) provided good insight into the general deformation behaviour of the walls. Shear stress distribution in the WSRM, ECRM and URM walls is shown in Fig. 3.6.

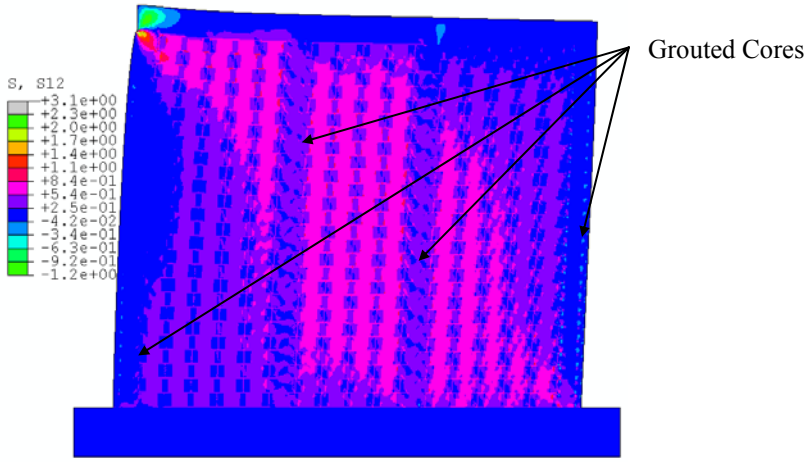

(a) WSRM wall

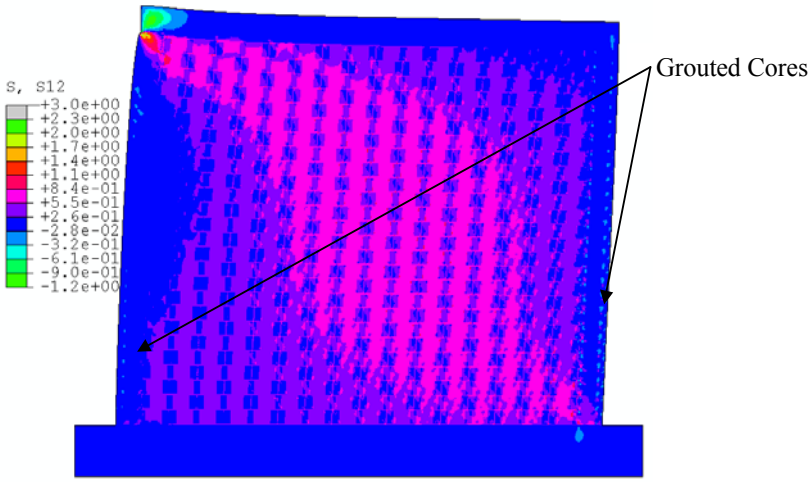

(b) ECRM wall

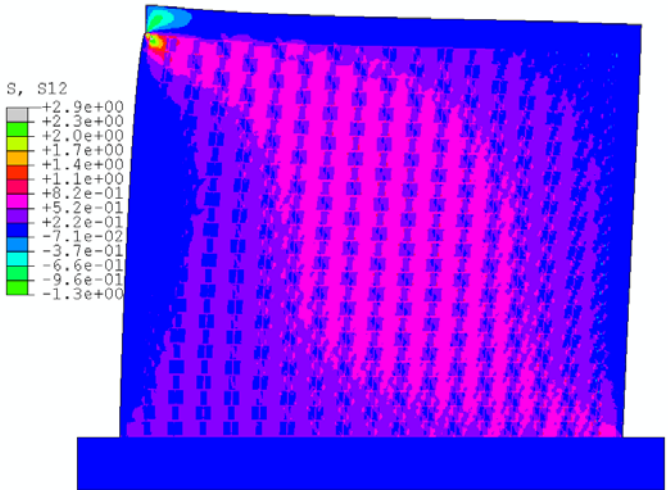

(c) URM wall

Figure 3.6: Shear stress distribution in masonry walls

Shear stress in all the three masonry shear walls dominated in the diagonal regions irrespective of the presence of vertical grouted cores. The magnitude of the shear stress in the hollow sections of masonry units was high (0.84-0.54MPa) along the diagonal of the walls with the exception of grouted cores where the shear stress was considerably lower (0.54-0.25MPa).

Fig. 3.6(a) shows that the magnitude of shear stress is much smaller in the grouted sections of the masonry units than the adjacent hollow sections. Elements in the mortar joints were closely examined and no significant distortion was observed.

The adoption of fine mesh as described in section 3.3.2 was adequate since the predicted failure path and the stress concentration at critical locations of the walls were similar to the theory as depicted in Figs. 2.3, 2.4 and 3.6. Therefore, mesh sensitivity analyses using coarser and finer meshes were not considered essential. However, for ultimate failure of the walls, mesh sensitivity was investigated and the effects are discussed in section 6.7.1.

3.5.1 Interaction of Grouted Cores with Ungrouted Masonry

Fig. 3.7 shows several critical regions of the masonry walls considered to examine the effects of grouting on the stress states of the adjacent elements. Three critical regions namely the centre, the heel, and the toe of the shear walls are dominated by different stress components (see Fig. 2.3). For example, at the centre of the walls, shear stress is dominant, at the heel vertical tensile stress remains dominant and at the toe region biaxial compression-compression stress is dominant. Therefore, distribution of only the most appropriate and dominant stresses was studied. Sections of vertical grouted cores were also selected along the diagonal of the walls to examine their effect on the adjacent unreinforced masonry.

Contours of stress distribution at three critical sections (centre, mid left core and mid right core) of the WSRM, ECRM and URM walls are plotted in Fig. 3.8. For these regions shear stress

variation was studied, as this was the dominant stress. These plots were extracted at 0.3mm of horizontal displacement under an equivalent vertical load of 0.5MPa.

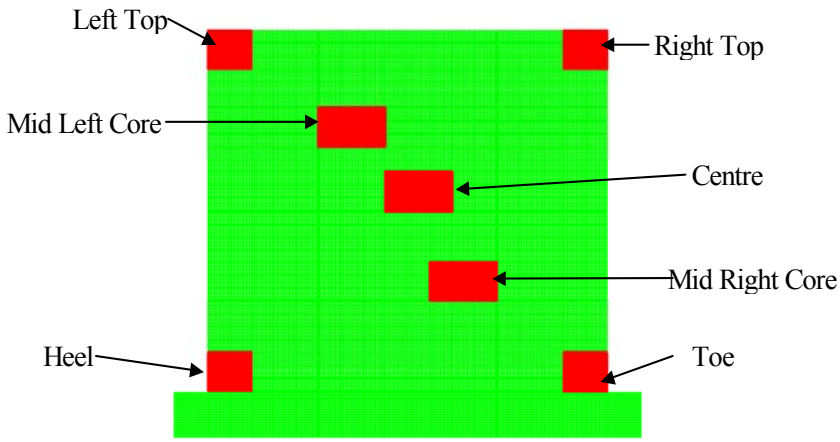

Figure 3.7: Critical regions of shear wall

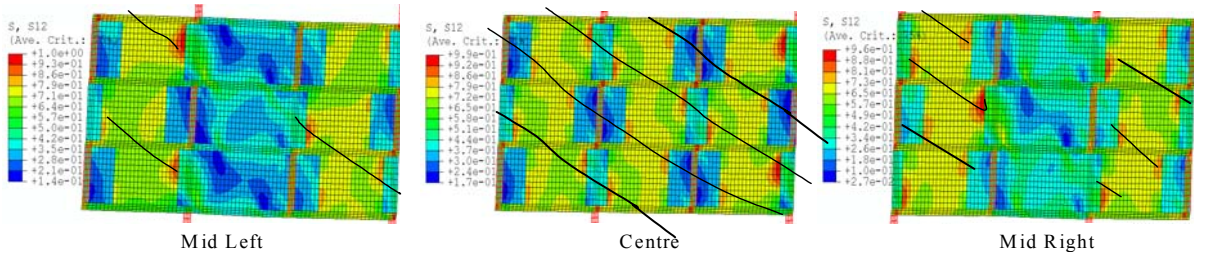

(a) Shear stress distribution in WSRM wall

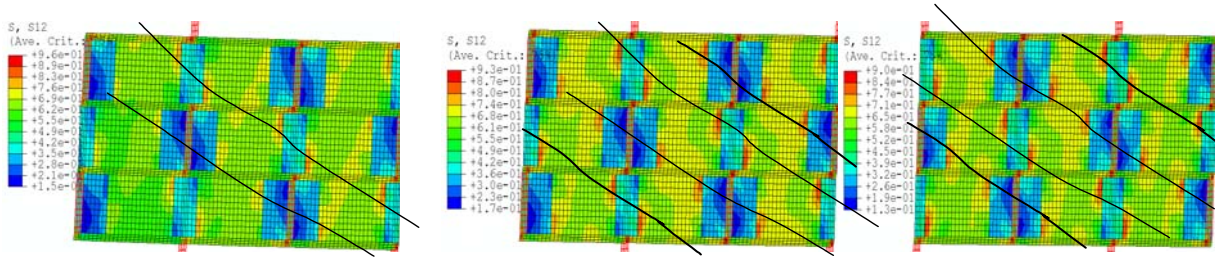

(b) Shear stress distribution in ECRM wall

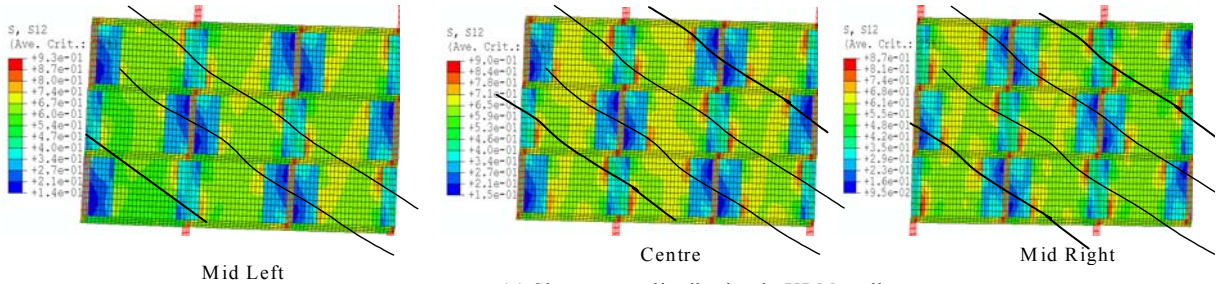

(c) Shear stress distribution in URM wall

Figure 3.8: Shear stress distribution at 0.3mm of horizontal displacement

Paths of the shear stress are marked on these contours to better understand the behaviour of the walls in the critical regions. Since all the regions shown in Fig. 3.8 were along the diagonal of the walls, flow of high shear stress was found inclined along the diagonal exhibiting potential failure paths. Stress flow was continuous in all three walls in a global sense; however, the stress flow was discontinuous locally at the location of the grouted cores of the WSRM walls with significant reduction in magnitude. In spite of this local discontinuity, the stress flow maintained its path along the diagonal in a global sense as can be seen from Fig. 3.8.

From the contours presented in Fig. 3.8, the following observations were made:

- Magnitude of shear stress at the mid left core section was the largest in all walls (WSRM / ECRM / URM) because this section was closer to the point of load application.

- Magnitude of shear stress in the WSRM wall was the largest relative to other walls in all three regions (centre / mid left / mid right).

- The width of the high shear stress region enlarged in size from the mid left core to the mid right core region passing through the central zone.

- Grouted section introduces significant reduction in the stress magnitude.

To examine the effect of grouted cores at the critical areas of the wall, selected components of stresses are plotted in Fig. 3.9. Plots for the shear stress (S12) distribution in the hollow block units and the horizontal mortar joints are presented for the centre, the mid left core and the mid right core regions; plots of vertical tensile stress (S22) for the toe and the heel are also included. Each graph contains stress distributions obtained from the analysis of the WSRM, the ECRM and the URM walls. Each plot is drawn using the horizontal distance measured from the heel of the wall. Elements representing the horizontal mortar joints and the hollow masonry units are highlighted at the top of each chart for the illustration of the location of stress points.

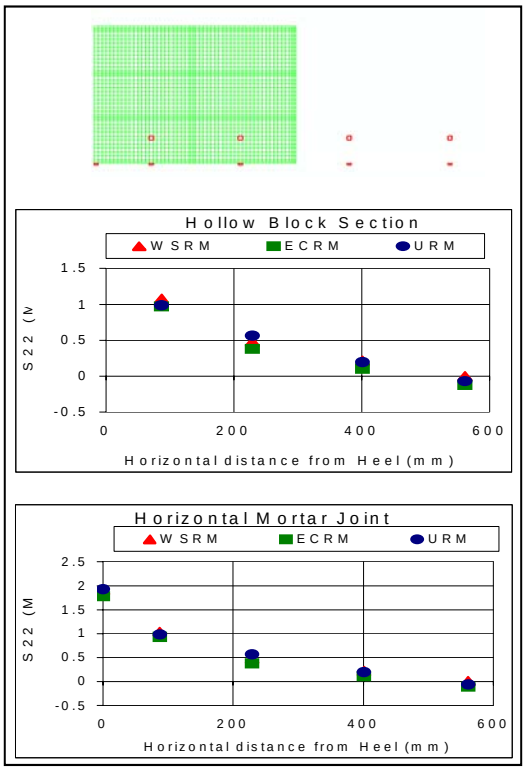

(a) Vertical tensile stress at heel

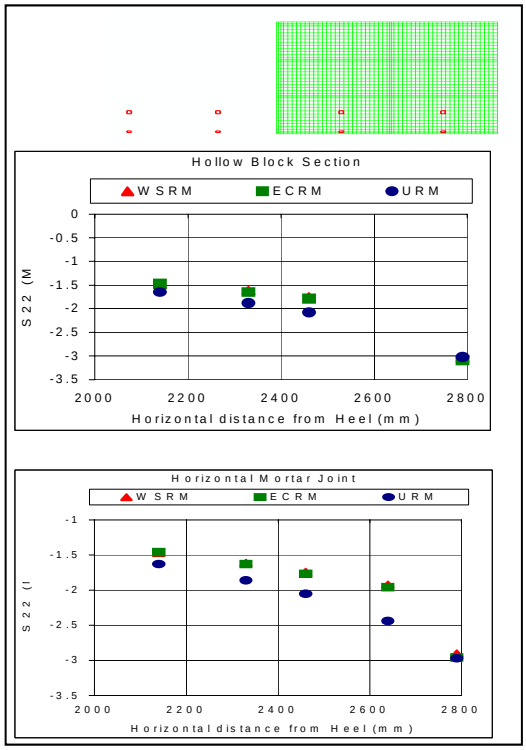

(b) Vertical compressive stress at toe

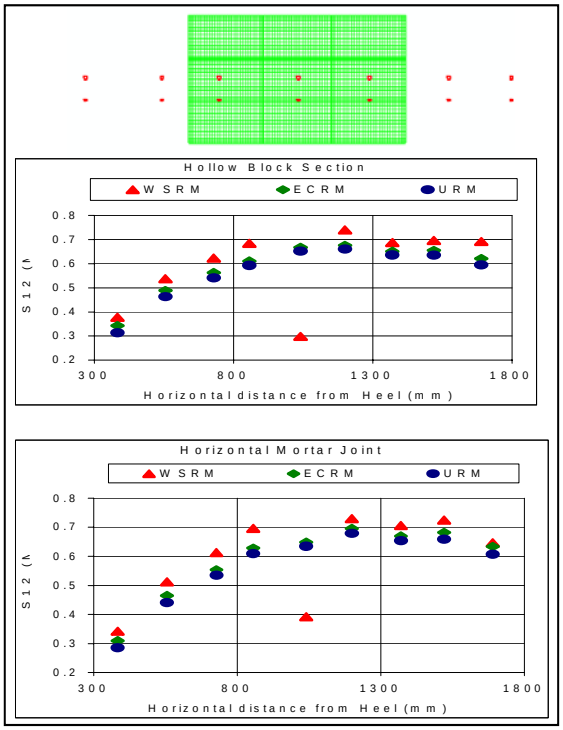

(c) Shear stress at Mid Left core

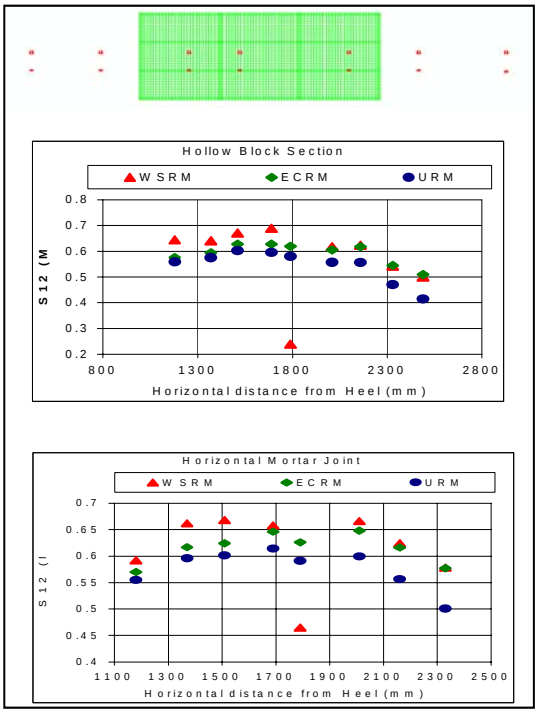

(d) Shear stress at Mid Right core

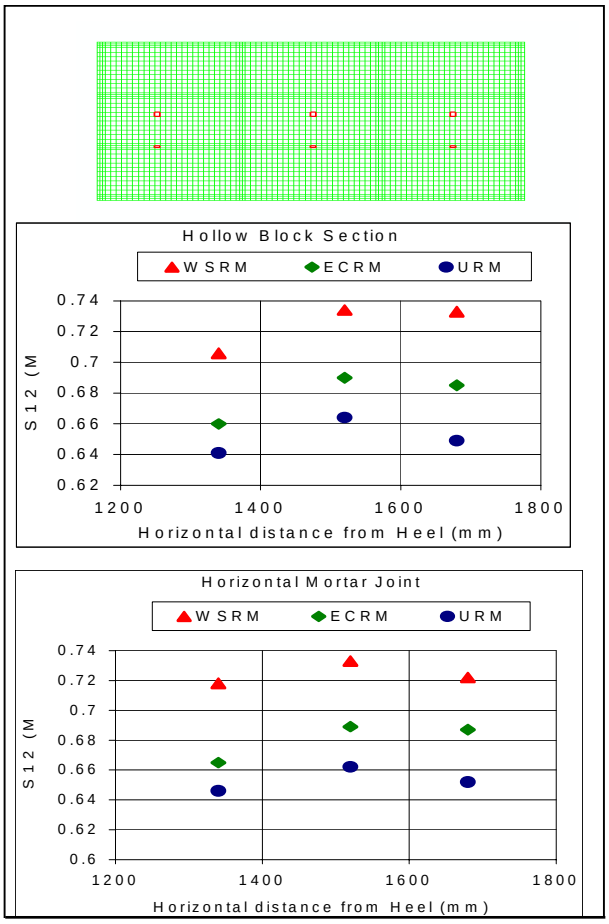

(e) Shear stress at centre

Figure 3.9: Stress variation at critical regions of the walls

From Fig. 3.9 following conclusion are made:

1. Higher magnitudes of vertical stress (S22) exist in the heel and the toe regions, whilst the shear stress (S12) is the largest at the centre of the wall. This result is in accordance with the generally accepted stress dominance criterion of the shear walls.

2. The presence of vertical grouted cores affects the shear stresses along the diagonal of the wall. The effect can be inferred from the increased magnitude of shear stress in the hollow block section and in the mortar underneath (Figs. 3.9(c), (d) and (e)) of the WSRM walls relative to the other walls. This phenomenon indicates potential for diagonal cracking of WSRM walls at early stages of diagonal drift. Increased stiffness of

WSRM walls perhaps have constituted to the higher level of shear stresses relative to other walls.

3. Shear stress flow has remained continuous for all walls in the diagonal direction except for the grouted sections where the stress was significantly low due to increased thickness. This observation has been made for all regions independent of the type of stress (S11/S22/S12) examined.

4. From Fig. 3.9(c) & (d), it can be seen that the shear stress (S12) in the grouted elements in the mid left and the mid right cores has remained smaller than that for the ungrouted sections.

5. The magnitude of the shear stress in the hollow units adjacent to the grouted cores is not significantly different from that for the hollow units away from the grouted sections. It shows that the vertical grouted cores do not affect (increase or decrease the stress) the adjacent hollow units locally; however, their effect is felt in a global sense as described in (2) above.

6. As the order of the magnitude of the shear stresses is not significantly different across the diagonal region (mid left, centre, mid right as shown in Fig. 3.9(c), (d) and (e)), it is expected that the diagonal crack would form along most of the entire diagonal rather than progressing from a limited length crack formed at the centre due to the variability in shear strength (affected by workmanship) typical of masonry.

The elastic analyses have provided a basis for hypothesizing the potential cracking and nonlinear behaviour of the masonry shear walls as listed below:

- The crack will form along the major compression diagonal of the shear walls irrespective of the presence or absence of the vertical grouted cores.

- The cracking will occur along most of the entire diagonal region rather than progressing from a small length crack from the central zone. Tracking the cracking path would therefore be difficult in the experiment. Width of crack zone rather than the crack length would offer a better indication of the lateral drift of single story masonry shear walls.

- The cracking is expected to be restricted to a smaller area in the mid-left region whilst it will be broader in the central and mid-right regions.

- WSRM walls will exhibit cracking at the early stages of lateral drift in comparison to the ECRM and the URM walls (in that order).

- WSRM walls will be stiffer than the ECRM and the URM walls (in that order).

3.6 Summary

Analyses of the full-scale masonry shear walls of length 2870mm, height 2408mm and thickness 150mm constructed from hollow clay blocks were performed. Each of these walls was discretised into 204,940 elements to provide three elements in 10mm thicknesses of the mortar joints to better understand the stress distribution and hence the elastic behaviour of the masonry shear walls. An attempt was made to infer potential failure mode as affected by the presence of vertical grouted cores.

Shear stress dominated along the diagonal region of the walls irrespective of the presence of vertical grouted cores. The magnitude of shear stress for the hollow units was higher than that of grouted units due to reduced thickness.

Vertical grouted cores did not increase or decrease the stress of the adjacent hollow units locally, but their presence increased the shear stress at the central zone of those walls that possessed them.

Grouted sections introduced local discontinuity to the shear, however, it was inferred that the discontinuity could not modify the potential global diagonal failure planes.

The magnitude of shear stress in the WSRM wall was the largest in all three regions (centre / mid left / mid right) when compared to that for the ECRM and the URM walls. This phenomenon indicated potential for early diagonal shear cracking in the WSRM walls.

High shear stress regions increased from a small area at the mid left core (close to the loaded point) to larger areas at the centre and the mid right core sections.

Stress flow was continuous across the vertical sections of the masonry shear walls except for the grouted cores where the stresses were significantly lower.

Stiffness of the WSRM wall was the largest compared to URM and ECRM walls reflecting the presence of additional grouted cores.

CHAPTER 4

EXPERIMENTAL INVESTIGATION OF WSRM SHEAR WALLS

4.1 Introduction

This chapter presents an experimental investigation of WSRM shear walls. Design of experiments, and construction and testing procedures for the shear walls are provided in detail. Mechanical properties of constituent materials, curing technique and handling process of walls are also included in this chapter. Details of the arrangement of boundary conditions, the positioning of sensors and data acquisition system are also presented. Failure mechanism and crack patterns of the shear walls observed during testing are also included. Typical data collected during the testing process and their use for extracting the behaviour of the walls are also explained.

4.2 Design of Experiments

Aspect ratio of the shear walls (aspect ratio = height/length), quantity and location of reinforcement and level of pre-compression are the major parameters that affect the behaviour of the masonry shear walls.

The quantity of reinforcement is linked to the expected severity of earthquakes and/or cyclones. Effect of distribution of the reinforcement to the behaviour of wide spaced reinforced masonry (WSRM) shear walls is not widely examined and the information available in the literature is limited to that of the author (Haider and Dhanasekar (2004)). In this study, experiments were

designed to investigate the effect of only one variable, namely the location of the vertical reinforcement, whilst all other variables were kept constant.

The strategy of examining only one parameter in detail using a full-scale experimental program is related to the need to minimise the costs. It is expected that a finite element model could be developed and validated using the experimental data set and then the FE model could be extended to investigate the sensitivity of all other parameters.

The reasons for identifying this strategy of varying only the spacing of the reinforced cores as the major parameter are as follows:

- From the elastic analysis presented in Chapter 3, it has been found that the presence of the intermediate vertical grouted cores has not modified the overall crack path relative to the ECRM and the URM walls. Presence of intermediate vertical grouted cores has therefore raised a question of their effect on the nonlinear/post-crack behaviour of the walls also.

- If the results obtained from the elastic analysis were true for the nonlinear behaviour also, then it would provide the opportunity to group most walls into a single category thus providing improved confidence to the experimental data set. (Had other factors – aspect ratio / load ratio been included in the experimental program, for each category, testing of more than one full scale specimen would not have been possible within the time and budget constraints of this PhD thesis).

- From the reasons listed above, only the location of the vertical grouted reinforced cores were varied in the experimental program and it was decided to examine all other parameters through a reliable finite element model developed as part of this thesis.

Detailing of all WSRM walls was carried out as per the Australian Standard for masonry structures. As a limiting case, walls containing reinforcement at end cores only (ECRM walls) with the spacing violating the 2000mm limit specified in AS3700 (2001) were also considered. One unreinforced masonry (URM) wall was also constructed and tested. A horizontal bond beam was constructed at the top of each wall to facilitate the application of inplane lateral loading. Details of the bond beam are provided in section 4.3 of this chapter. All walls were constructed on a reinforced concrete footing.

A total of eleven single leaf, clay block shear walls were constructed and tested. Among these walls, there was one URM wall, two ECRM walls and eight WSRM walls. All walls had the same gross dimensions (2408mm high, 2870mm long and 150mm thick that represent nine blocks long and 28 blocks high); no wall contained openings. The size of the walls was so designed that they could easily fit within an available rigid loading frame capable of applying displacement controlled lateral loading with ease even after significant cracking of the walls.

All the walls were constructed from the commercially available hollow clay blocks. Blocks were of gross dimensions 310mm × 150mm × 76mm with two symmetrical voids of size 100mm × 80mm × 76mm in the centre to accommodate grouting and steel bars. Gross area of the walls determined as the product of the thickness of the wall (150mm) and the length of the wall (2870mm) was equal to 430,500mm^2, whereas the design area of the WSRM walls determined as the bedded area of the ungrouted masonry (70mm × 2870mm), plus the area of the grouted cores (4mm × 100mm × 80mm) was equal to 232,900 mm^2. For ECRM walls the design area was equal to 216,900 mm^2 and for the URM wall the design area was equal to 200,900 mm^2.

In this experimental program each WSRM wall was reinforced with 4N12 (four normal ductility 12mm diameter) vertical bars with one bar in each grouted core providing the vertical reinforcement ratio equal to 0.10% or 0.19% depending on whether gross area or the design area

was used in the calculation. Figure 4.1 shows the location of reinforcement bars for all the walls considered in the test program. It should be noted that only the cores that contained reinforcement were grouted and all other cores were left ungrouted. Walls #1 to #8 were WSRM, #9 and #9A were ECRM, and #10 was URM.

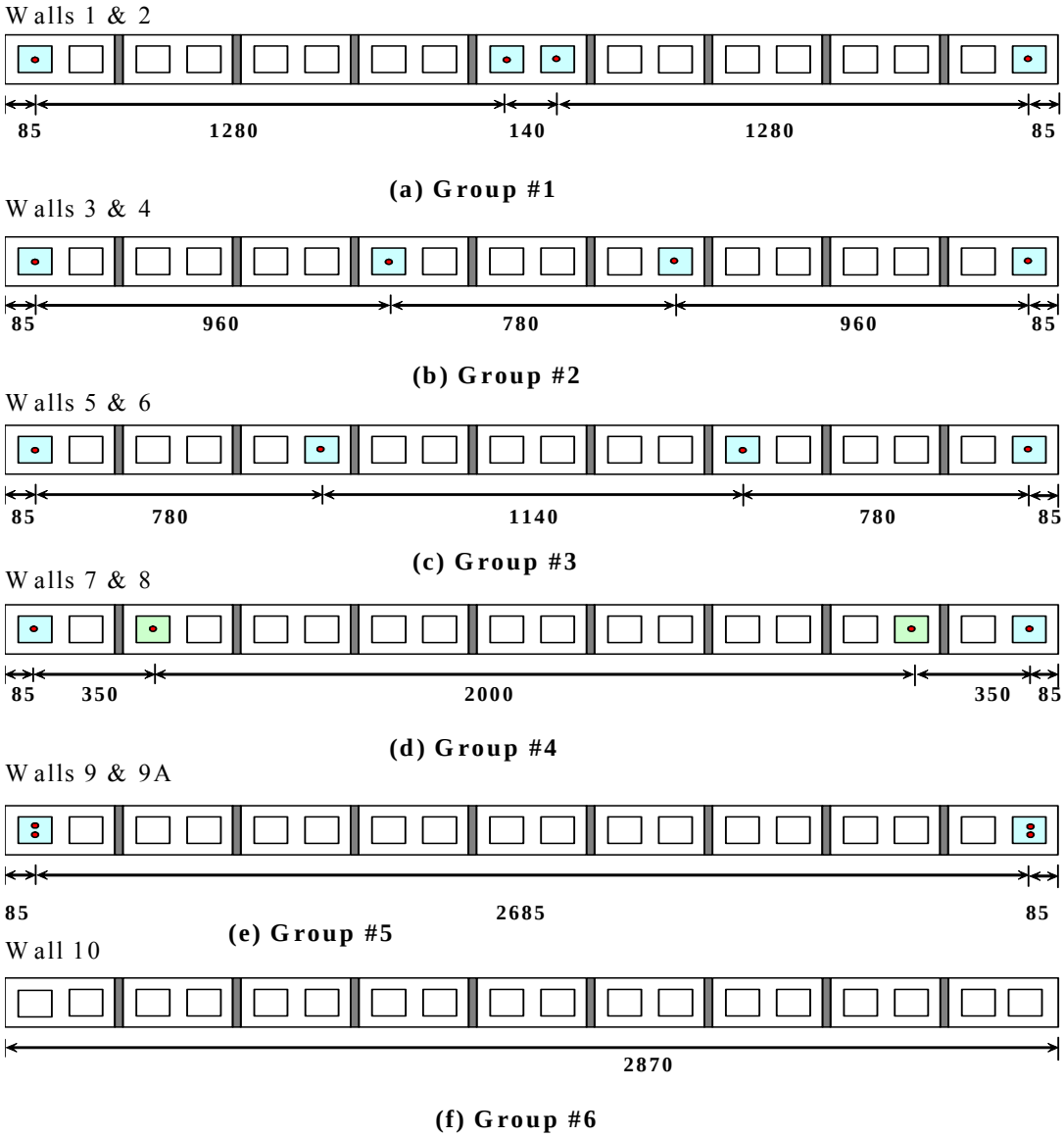

Figure 4.1: Design details of walls

Based on the location of the vertical reinforcement, there were four groups of WSRM shear walls where each group consisted of two walls. The first group consisted of walls #1 & #2 with centre to centre spacing of intermediate grouted cores equal to 140mm. The second group

consisted of walls #3 & #4 with centre to centre spacing of the grouted cores equal to 780 mm. The third group consisted of walls #5 & #6 in which centre to centre spacing of the intermediate grouted cores was equal to 1140 mm. The fourth group consisted of walls #7 & #8 in which the centre to centre spacing of the intermediate grouted cores was equal to 2000mm. The first wall in each of these groups was tested under monotonic loading and the second wall was tested under cyclic loading.

Walls #9 and #9A were of ECRM type. Both of these walls were tested under monotonic loading. Mechanical disorder of the test setup affected the testing of wall #9A; subsequently the results of this wall were disregarded. Therefore, another wall (#9) with the same parameters was constructed and tested. Wall #10 had no grouted cores or reinforcement and was of the URM type. This wall was tested under monotonic loading only. Detailed behaviour of all these walls is reported in Chapter 5 of this thesis. Design details of the walls shown in Table 4.1 include the group numbers and designation of walls, loading history, and width of the middle and end URM panels for each wall.

Table 4.1: Design details for test specimens

Group	**Wall No.**	**Designation of Walls**	**Loading History**	**Panel width of URM (mm)**	
				Middle	**End**
Group #1 (Fig. 4.1a)	**#1**	**WSRM# 1**	Monotonic	-	1280
	#2	**WSRM #2**	Cyclic		
Group #2 (Fig. 4.1b)	**#3**	**WSRM #3**	Monotonic	780	960
	#4	**WSRM #4**	Cyclic		
Group #3 (Fig. 4.1c)	**#5**	**WSRM #5**	Monotonic	1140	780
	#6	**WSRM #6**	Cyclic		
Group #4 (Fig. 4.1d)	**#7**	**WSRM #7**	Monotonic	2000	350
	#8	**WSRM #8**	Cyclic		
Group #5 (Fig. 4.1e)	**#9**	**ECRM**	Monotonic	End cores reinforced	
Group #6 (Fig. 4.1f)	**#10**	**URM**	Monotonic	No vertical reinforcement	

It could be regarded that the vertical grouted cores containing reinforcement bars divided each WSRM wall into three zones of unreinforced masonry confined by the grouted reinforced cores and the bond beam. The ECRM wall had reinforcement bars only in the end cores, providing only one panel of unreinforced masonry confined by the reinforced end cores and the bond beam. The URM wall did not have any vertical grouted core, therefore, the whole wall acted as one block of uniform masonry. The URM wall, however, had a bond beam at the top to facilitate the application of the horizontal load.

4.2.1 Constituent Materials

Material properties such as the type and the quantity of the vertical reinforcement, the type of masonry units, the mortar mix and the grout mix were intended to be maintained uniform for all the walls so that solely the effect of the spacing of the vertical reinforcement would be investigated. However, due to workmanship issues, some variability in material properties could not be avoided. To examine the effect of the variability in the material properties, samples of the mortar, the masonry units, the grout, and the grouted and ungrouted masonry prisms for each wall were collected at the time of construction and tested at the time of testing of the walls. Three specimens for each constituent material were prepared and tested as per standard procedures (AS2701.4 (1984), AS4456.3 (2003), AS3700 (2001)). All the test samples were air cured for 24 hours and then kept in the water tank until tested.

Using standard test procedures (AS2701.4 (1984), AS4456.3 (2003), AS3700 (2001)), the compressive strength of these constituents was determined. Mortar M3 (as per classification of Australian Standard for masonry structures AS3700 (2001)) was used in the construction of all the walls. This general purpose mortar mix is normally used for masonry elements in interior environments to meet minimum durability requirements of the Australian Standard for durability of structures (AS2699 (2002)). This mortar was prepared by mixing 1:1:6 proportions by volume

of general purpose Portland cement, building lime and sand respectively. A commercially available mortar plasticiser (Brickies Own) was added as per the manufacturer's specifications to maintain the workability of the mortar mix. Mortar cubes of size 50mm × 50mm × 50mm were made to determine the representative compressive strength of the mortar used in the construction of the test walls. Photographs of the mortar samples were taken and are presented in Appendix B of this thesis. Average compressive strength of the mortar cubes calculated from Eq. 4. 1 for each of the test walls is provided in Table 4.2.

$$\text{Compressive Strength (MPa)} = \frac{\text{Failure Load (N)}}{\text{Bearing Area (mm}^2\text{)}} \tag{4.1}$$

As per Table 3.2 of AS3700 (2001), compressive strength factor is 1.0 for masonry aspect ratio of 7.6. For all the walls tested for this research program, masonry aspect ratio was 7.6 since the masonry blocks and the mortar bed joints were 76mm and 10mm thick respectively. Therefore no modification was required for the compressive strength measured from experiments. Photographs of the tested masonry prisms are included in Appendix B.

Voids of masonry blocks in the bond beam and the intended vertical cores were filled with grout. The grout was prepared by mixing 350kg cement, 275 kg water, 768kg 10mm size aggregate and 747kg sand for each m^3 of grout. The water cement ratio for this grout mix was kept equal to 0.79. This mix proportion was taken from Kumar (1995) who carried out a large number of tests to arrive at a grout mix that maximised the compressive strength of the grouted masonry. Grout cylinders of size 100mm diameter × 200 mm high were made at the time of grouting of the walls. Average compressive strength of the grout (measured at the time of testing of the walls) is reported in Table 4.2. Compressive strength of the test samples was calculated from Eq. 4.1. Photographs of the specimens of grout cylinders are included in Appendix B.

Masonry prisms were constructed as 4-high stack bonded prisms (310mm long × 334mm high × 150mm wide) with three mortar bed joints. Hollow voids of masonry blocks used in the construction of the prisms (100 mm long × 80 mm wide) were filled with grout at the time of grouting of the walls. The prisms were tested at the time of testing of the walls. Average compressive strength of masonry prisms calculated from Eq. 4.1 for all the test samples is provided in Table 4.2.

Table 4.2: Average compressive strength of the constituent materials (MPa)

Wall No.	Mortar Cubes[1]			Grout Cylinder[2]			Masonry Prism[3] (f_m)		
	Number of samples	Mean	Standard Deviation (MPa)	Number of samples	Mean	Standard Deviation (MPa)	Number of samples	Mean	Standard Deviation (MPa)
WSRM #1	3	8.3	1.37	3	28.4	0.86	3	12.5	3.53
WSRM #2	3	9.3	0.59	3	23.6	0.57	3	14.4	2.36
WSRM #3	3	9.7	0.71	3	29.5	1.28	3	13.7	1.65
WSRM #4	3	9.5	1.10	3	31.5	1.13	3	14.4	2.48
WSRM #5	3	5.3	0.59	3	34.8	1.19	3	15.5	0.91
WSRM #6	3	6.9	0.46	3	39.7	3.62	3	15.7	2.09
WSRM #7	3	5.0	0.65	3	36.5	1.85	3	18.4	1.23
WSRM #8	3	6.4	0.81	3	34.7	5.28	3	18.1	1.39
ECRM	6	10.0	0.78	6	39.7	3.29	7	20.1	3.39
URM	3	5.1	0.61	3	34.6	8.18	3	15.7*	1.21

1: 50mm x50mm x 50mm, 2:100mm diameter x 200mm high, 3: four high stack bonded prism
* Hollow masonry compressive strength

To determine the compressive strength of masonry clay blocks, specimens of size 25mm × 25mm × 50mm were cut from randomly selected full clay blocks and were tested under displacement controlled compression force. The average value of the compressive strengths obtained for these specimens was equal to 40MPa.

The effects of the workmanship are evident from the variation of compressive strength of the mortar and grout and are also reflected in the compressive strength of masonry prisms. Masonry units were factory made; therefore, they exhibited almost the same compressive strength. To

neutralise the effect of the variation in the material properties on the behaviour of the walls, the ultimate load capacity of the walls was normalised using the shear strength of masonry calculated from the compressive strength of masonry prisms as shown in Eq.4.2.

$$\text{Normalised Horizontal Load} = \frac{\text{Inplane Horizontal Load}}{0.22\sqrt{f_m} \times \text{A}_\text{g}} \times 10^3 \qquad (4.2)$$

where 'f_m' is the compressive strength of masonry and 'A_g' is the gross area of the wall.

4.3 Construction, Curing and Handling of Walls

A specially designed reinforced concrete base slab was constructed for each wall to allow fixing to the strong floor of the Heavy Testing Laboratory (HTL) of the Central Queensland University (CQU). A photograph of reinforcement detailing for the slab and the vertical steel bars required for the walls placed within the footing as starter bars of a typical base slab are shown in Fig. 4.2(a). Fig. 4.2(b) shows the finished top surface of the slab that was used for laying masonry blocks after seven days of curing of the slab. The top surface was finished with a steel trowel and no adhesive material was applied to the top surface of the slab. The surface was left smooth to provide a horizontal mortar joint between the slab and the masonry units.

(a) Before concreting (b) After concreting

Figure 4.2: Construction of a base slab used for fixing the test wall to the strong floor

A mason with average workmanship skills constructed all the test walls. Masonry was laid in face shell bedding using a mortar bed of 10-mm thickness and was grouted seven days after construction of the walls. A high level of attention was paid to maintain consistency of the geometric parameters (length, height, thickness) of all the walls. The author supervised all the construction to ensure the standard requirements of masonry construction were achieved. All the walls were constructed inside the HTL of the Central Queensland University. One of the walls just after completion of construction is shown in Fig. 4.3(a).

(a) Wall just after construction (b) Wall under dripline curing

Figure 4.3: Curing process of walls

Drip lines were installed on both sides of the walls to maintain a uniform spray of moisture for curing. Water was supplied to the drip lines on a daily basis for seven days to cure the walls. Bond beams and the grouted masonry cores were also cured along with the walls using the drip lines. All walls remained covered in thick polyethylene sheeting as shown in Fig. 4.3(b) to prevent evaporation of moisture. After curing, the walls were shifted to the test rig in the laboratory using an overhead gantry crane. Speed of the crane was kept to the lowest possible level to avoid any jerky motions and premature failure of the walls.

A bond beam of size 2870mm × 150mm × 172mm consisting of two layers of masonry blocks reinforced with 4N16 bars was constructed at the top of each wall. The purpose of the bond

beam was to enable uniform distribution of the applied vertical load and to minimise the chances for local failure of the loaded corner of the walls under the application of the horizontal displacement controlled loading at the time of the test.

Special attention was paid to the masonry cores containing the vertical reinforcement bars and the horizontal reinforcement bars for the bond beam. The bottom of the vertical cores accumulated mortar dropping during construction of the walls. These cores were flushed out using water with great care after construction of the walls to leave them clean for grouting. The tops of the vertical hollow masonry cores were filled with scrap paper to fill the gap and to provide a temporary bedding surface for the wet grout to be poured in the horizontal bond beam. A smooth surface steel bar was used for tamping the wet grout in the vertical cores and a steel trowel was used for tamping the grout in the bond beam.

The size and location of the hollow rectangular voids in the masonry units and the traditional masonry construction practice resulted in staggered hollow vertical cores. A typical staggered shape of grouted cores is shown in Fig. 4.4.

Figure 4.4: Staggering of cores in the test walls

A tested wall was dismantled as shown in Fig. 4.4 to investigate whether the grout was properly filled and compacted in the staggered cores. A hammer and a chisel were used to remove the brick shell around the grouted core; it was found that the grout surrounding the reinforcement was hard and well compacted. This investigation provided evidence of the quality of the grouting process, which could not be assured at the time of grouting of the walls

4.4 Testing of Walls

All the walls were tested using a general purpose test rig shown in Fig. 4.5 at the Heavy Testing Laboratory (HTL) of the Central Queensland University (CQU) under a constant precompression and horizontal inplane racking load. A 2000 kN compression hydraulic cylinder was used to apply the vertical load on a spreader beam, which in turn distributed this load uniformly to the full length of the wall. The horizontal load was applied under controlled displacement. The depth of the spreader beam was sufficient to achieve the required load spread.

A 500kN tension-compression hydraulic cylinder was used to apply the horizontal load on the vertical face of the bond beam. Both the horizontal and the vertical hydraulic cylinders were bolted to the loading frame and were controlled by a software system LabVIEW (2004). After the application of the required vertical load, horizontal displacement was gradually increased either monotonically or cyclically until failure of the walls. This section describes the arrangement of the boundary conditions, locations of the data sensors, the loading history and loading procedures used for the application of monotonic and cyclic loading.

From Fig.4.5 (d), it can be seen that the 900WB218 spreader beam and the steel made rolling assembly provided an effective bearing width of 2870mm for uniformly spreading the vertical load to 2.87m long WSRM walls. The dispersion of vertical load shown in Fig 4.5 (d) is as per figure 5.13.1.1 of the Australian Standard for steel structures (AS4100 (1998)).

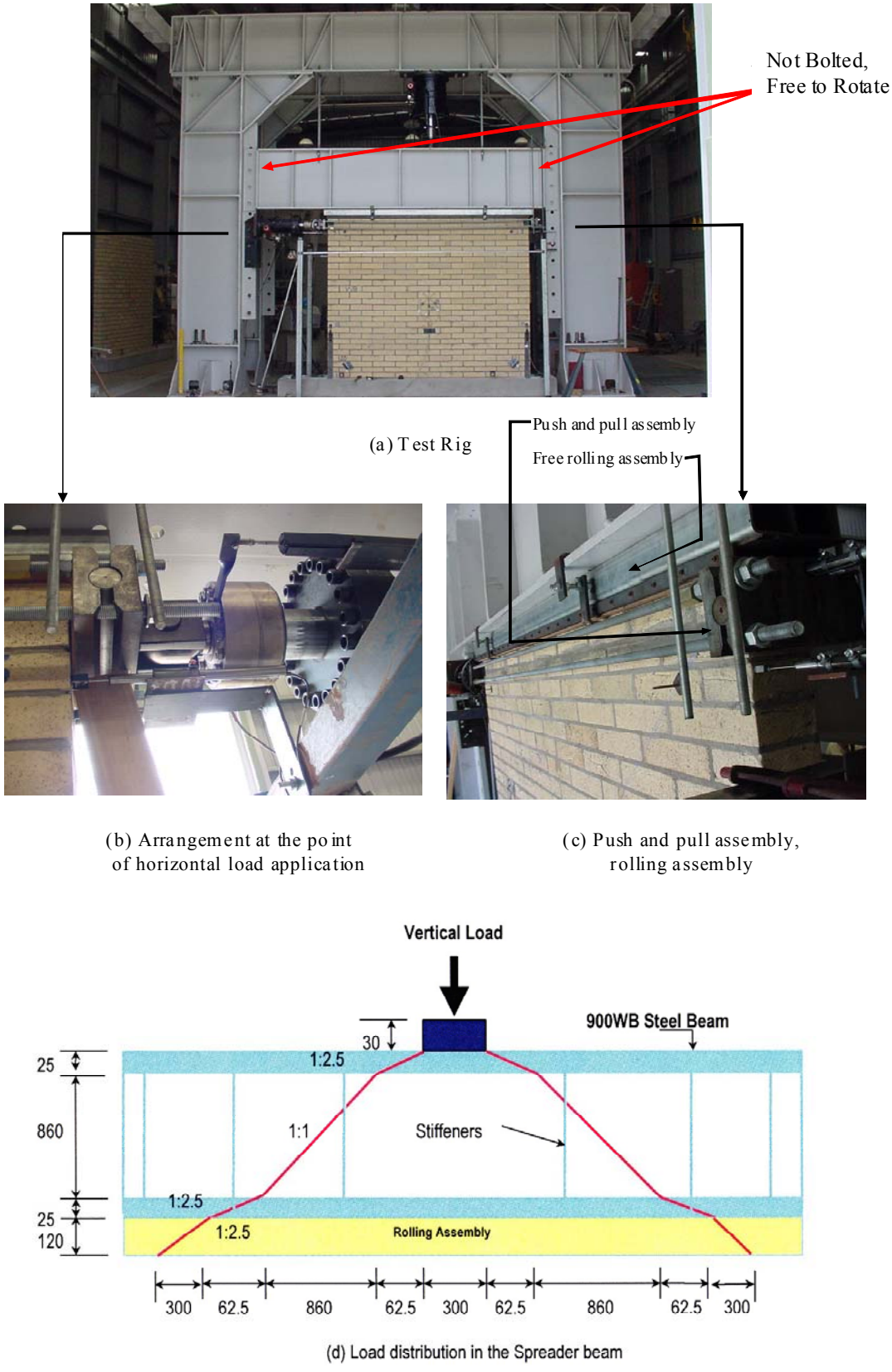

Figure 4.5: Test rig, push-pull and free rolling assemblies

4.4.1 Arrangement of Boundary Conditions

As all walls were required to simulate the response of true cantilever walls, appropriate boundary conditions were therefore arranged after positioning the walls inside the test rig. The base slab at the bottom of the wall was bolted down to the strong floor of the HTL through six 48mm diameter bolts to prevent any horizontal sliding of the base slab due to the application of the horizontal load.

A prefabricated assembly shown in Fig. 4.5(c) consisting of four N24 threaded bars with two 20mm thick end plates was placed and tightened around the bond beam at the top of the wall. This assembly connected to the horizontal cylinder allowed the push and pull mechanism to act on the wall under the application of displacement controlled horizontal loading. Another prefabricated assembly shown in Fig. 4.5(b) consisting of channel sections and steel rollers was placed on top of the bond beam for the full length of the wall to allow the top of the wall to freely drift longitudinally. A schematic diagram of the boundary conditions is shown in Fig. 4.6.

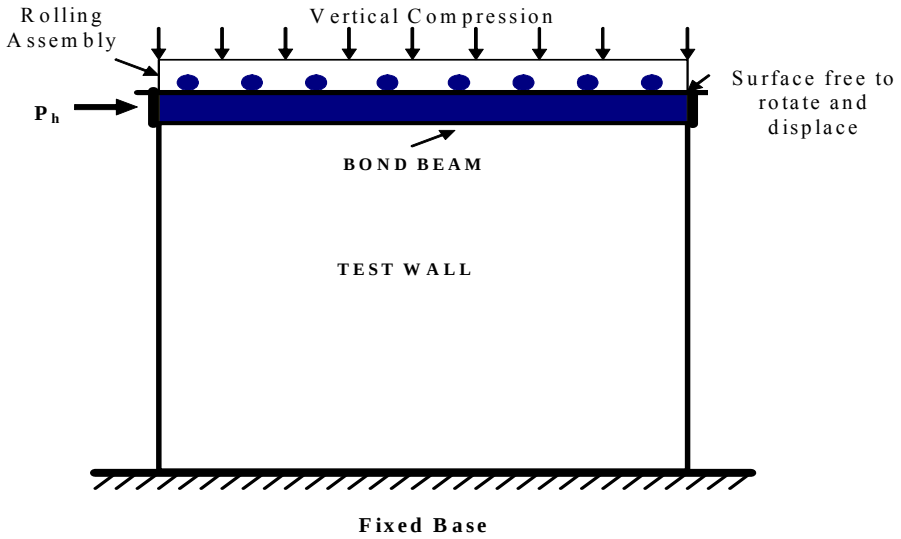

Figure 4.6: Schematic diagram for boundary conditions arranged for testing of the walls

A deep spreader beam was then positioned on the top of the rolling assembly and a hydraulic cylinder of capacity 2000kN was then positioned on top of the spreader beam aligned to the centre of the wall to apply vertical compression.

A clear horizontal gap of 25mm was left between the end of the wall including the testing apparatus and the supporting frame. This gap ensured free lateral drift of the top of the wall. Lateral drift of the spreader beam was calculated by the application of simple trigonometric functions to the deformed rectangle consisting of the wall and the spreader beam. Coordinates of the deformed rectangle were calculated using the data collected during the test. It was found that the potential drift in spreader beam was smaller than the gap left between the end of the spreader beam and the loading frame at the full application of the horizontal load, which ensured a free top surface capable of translating horizontally and rotating in the plane of the wall.

4.4.2 Positions of Sensors

Load and deformation was measured through a total of 23 data collection channels installed on each test wall. These channels were as follows:

- Load measurement (2 channels)
- Displacements measurement LVDTs and potentiometers (15 channels)
- Surface strain measurement LVDTs (6 channels)

A schematic diagram of all data channels is shown in Fig 4.7. Numbers marked before and after the slash "/" symbol were so allocated to the channels that would continuously collect data from South and North faces of the test walls respectively. North face and East and West ends of the wall are marked in Fig. 4.7. The average values from North and South faces were used to plot the deformation behaviour of each wall.

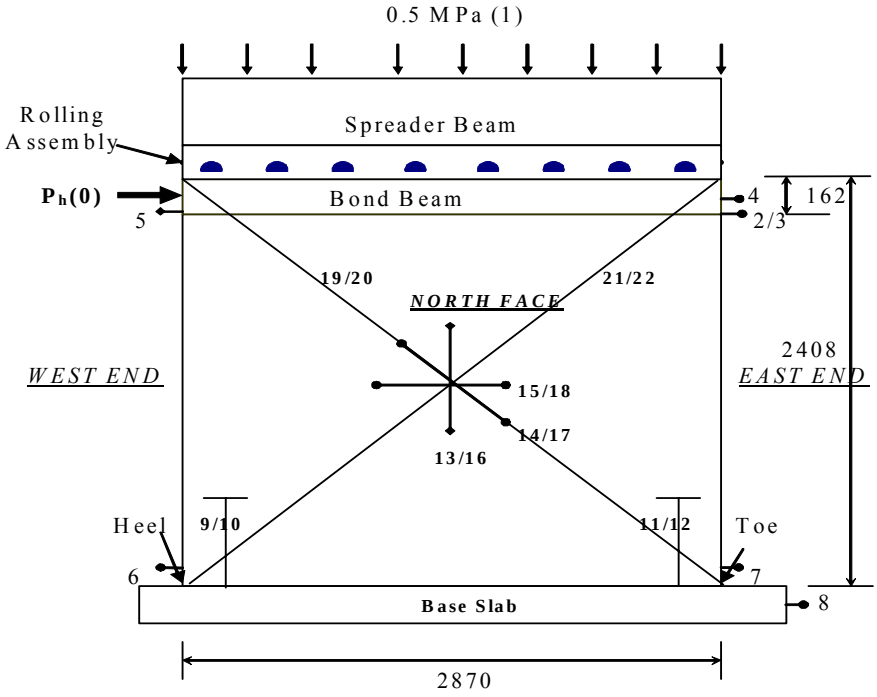

Figure 4.7: Sensors for loads and deformations for the test walls

Channel 0 was used to read the horizontal load. This load was applied under controlled horizontal displacement. The value of the horizontal load was continuously monitored on the data acquisition computer screen.

Channel 1 read the vertical load applied to the spreader beam.

Channels 2 and 3 read horizontal deformation at the bottom of the bond beam at the East end of the wall. The average value of the two readings determined the deformation at the top of the walls.

Channel 4 was so installed that it could read the horizontal displacement of the bond beam at the East end of the wall in the line of application of the horizontal load. Channel 5 read horizontal deformation displacement at the bottom of the bond beam at the West end of the wall.

Due to the importance of the deformation of the top of the cantilever wall, many channels were used at the expense of being redundant.

Channels 6 and 7 read data for horizontal deformation at the heel and the toe of the walls respectively. Channel 8 recorded possible horizontal movement of the base slab relative to the strong floor of the HTL.

Channels 9&10 and 11&12 were used to record vertical deformation of the heel and toe of the walls respectively.

Channels 13-18 read inplane relative deformations at the centre of the walls, which were used to define the strain state at the centre of the walls.

Channels 19-22 collected diagonal deformations of the walls. These channels were used for walls # 5 to #10. These channels were not used for the first four (#1 to #4) walls.

Channels 2-12 were all LVDTs, channels 14-18 were all LVDTs in Strain Rosettes configuration and channels 19-22 were all Mechanical String Pots. Gauge lengths for LVDTs and string pots were measured and recorded prior to application of loads. Steel wires of 1mm diameter were used with string pots to measure the deformation of the walls along the diagonals. String pots fixed at the bottom corners of the walls allowed rolling and unrolling of the steel wires as the wall diagonals elongated or shortened under the application of horizontal displacement. Steel wires were fixed at the top corners of the walls opposite to the location of string pots. Typical use and significance of the data collected from these channels are explained in section 4.5 of this chapter.

4.4.3 Loading History

It is common to test structures in low cycle fatigue, which is a method of subjecting the specimens to cycles of high magnitude deformation or load (typically a maximum of a few hundred cycles only) until failure to infer the response to seismic action. To perform the cyclic loading tests on WSRM walls, it is necessary first to acquire knowledge on the monotonic

behaviour of the structures. In this research program, monotonic loading tests were performed on the first wall of each wall group to obtain its load – deformation behaviour. Information on load-displacement data collected during the monotonic loading test helped with designing the displacement history for the cyclic loading tests.

Several patterns of displacement cycles have been used by various researchers (Usami et al. (1991), Tomazevic et al. (1996), Bernardini et al. (1997), Zhuge et al. (1996)) to investigate the behaviour of structures under cyclic loading. A most commonly used loading history is the one in which progressively increasing amplitudes of displacement are cycled twice. This pattern of history was adopted in this experimental study as shown in Fig.4.8.

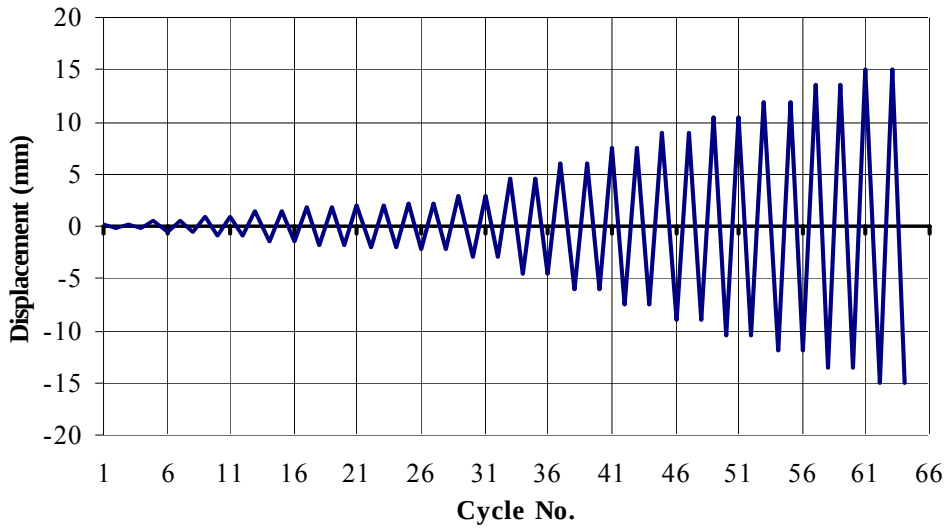

Figure 4.8: Loading history for the cyclic load tests

4.4.4 Application of Loading

In all tests, the loading was applied under displacement control to allow monitoring of the complete load deformation response. Initially the increment in displacement was kept small (0.2mm) until the elastic range, then it was increased to 1mm until the failure of the walls.

The first wall of each group was tested under monotonic loading and its load - displacement data were used to determine the loading history for performing cyclic loading test of the second wall. In the monotonic loading test, horizontal displacement was applied only in one direction until failure of the wall and then the direction of the applied displacement was fully reversed and increased until the wall became structurally unstable. In the cyclic loading test, cycles of positive and negative displacements were applied until failure of the wall.

None of the walls failed suddenly during testing. Therefore, the increment in the horizontal displacement was ceased upon the first occurrence of any of the following three parameters:

- Peak load dropped by at least 20%
- Crack widths in different regions of the wall became wide-open providing indication of stability failure of the wall
- Gap between the wall and the loading frame decreased to such a point that there was a probability of activation of unwanted restraint from the frame to the top corner of the wall.

The scheme of application of loading for the monotonic tests was as follows:

- Loading of the walls in the forward direction until failure
- Unloading of the walls in the forward direction
- Loading of the walls in the reverse direction until failure
- Unloading of the walls in the reverse direction

All the walls tested under monotonic loading in the forward direction were pulled back and loaded in the reverse direction under the same loading rate.

4.4.5 Data Acquisition System

The data acquisition program "LabVIEW (2004)" collected the required data from all the channels set to read the applied load and deformation of the walls. Values of the horizontal load and displacement readings from channels 3 and 4 were plotted on the computer screen, which allowed continuous monitoring of the walls during the test. A typical screen shot is shown in Fig. 4.9.

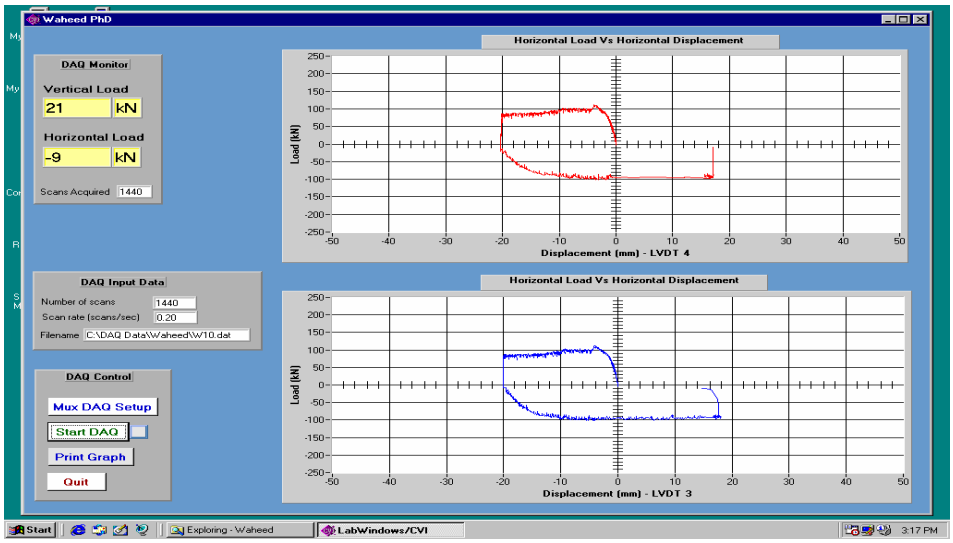

Figure 4.9: Monitoring of the test during application of loads

The vertical load was also displayed on the computer screen during the test to monitor it continuously. This program collected data from each channel once every 5 seconds for the entire period of the testing. Monotonic loading tests took approximately two hours and collected approximately 1440 data points. Cyclic loading tests took on average six hours and provided approximately 4300 data points.

4.5 Typical Test Data

23 channels of data were used for understanding loads and deformations. Among these channels, some were installed only to check the appropriateness of the boundary conditions of the test set-up and others were installed to read deformation at critical locations of the test walls. In this section, typical data collected from each channel are plotted and their significance to the overall behaviour of the walls is explained. Horizontal load is plotted against horizontal displacement measured at various locations of the walls from the stage of loading the walls in the forward direction to the unloading stage of the walls in the reverse direction.

Data collected from channels 0 and 1 for the vertical load and the horizontal load plotted against the displacement read through channel 4 are shown in Fig. 4.10. It is evident from Fig. 4.10(a) that the vertical load remained constant throughout the horizontal load loading history. This is an important factor in the testing of shear walls.

Horizontal load response for different walls is provided in detail in Chapter 5 of this thesis. Fig. 4.10 (b) shows a typical set of horizontal load data.

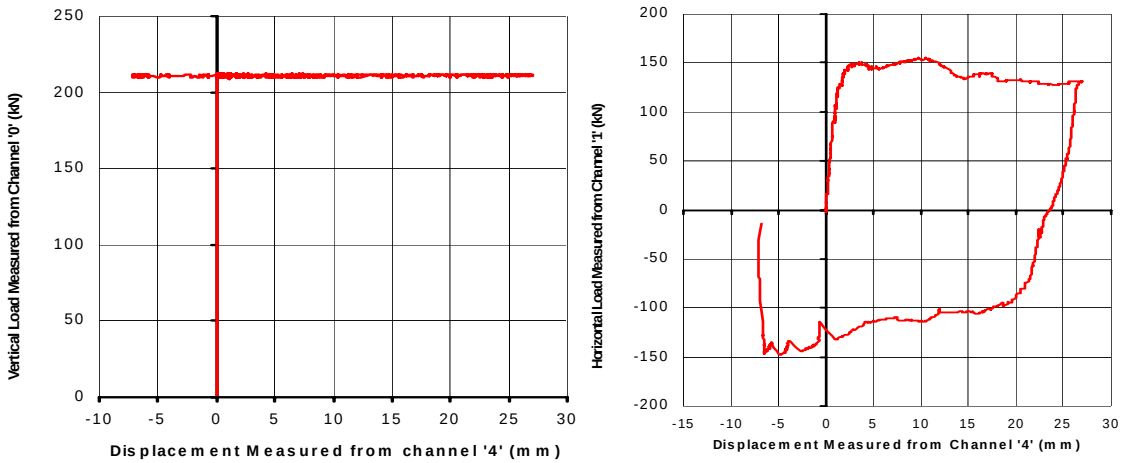

(a) Channel 0 (Vertical load) (b) Channel 1 (Horizontal load)

Figure 4.10: Data from channels ‘0’ and ‘1’

To determine appropriateness of data, the horizontal load is plotted against displacement measured from channels 2, 3, 4 and 5 in Fig. 4.11. It is clear from this figure that the displacement measured through channels 2, 3 and 4 at the West end of the wall had almost the same value, whereas the displacement measured through channel 5 located at the East end was significantly lower. This difference was due to the fact the LVDTs at location 2, 3 and 4 were at the opposite end to the horizontal load whereas LVDT 5 was located close to the horizontal load and was locally affected by the bearing stresses. Therefore data from channel 5 near loading jack location were disregarded. The load-displacement curve of the walls was plotted using the values of horizontal displacement measured from channel 4 at mid height of bond beam or the average horizontal displacement measured from channels 2 and 3 at the bottom of bond beam location.

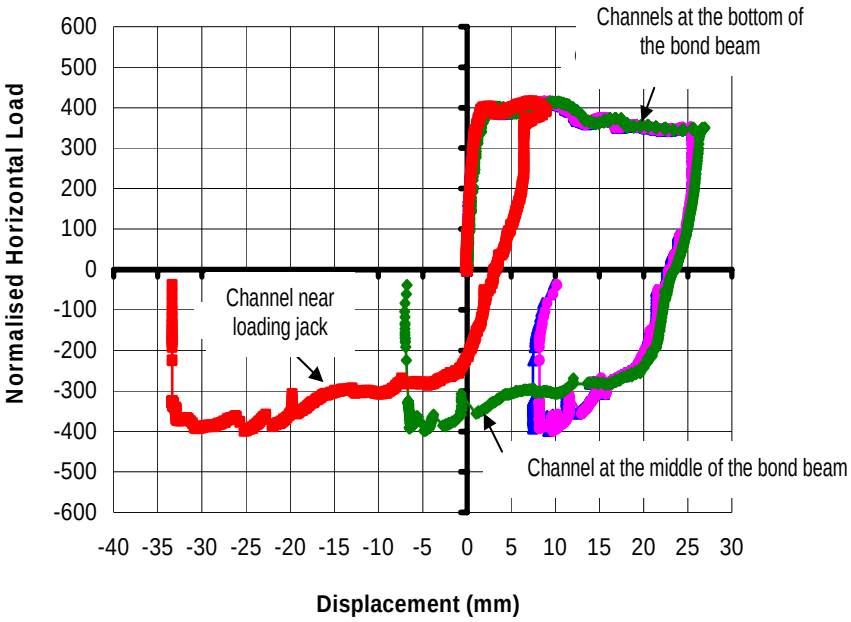

Figure 4.11: Horizontal load versus displacement measured at bond beam level

To examine the appropriateness of the deformation data collected, the horizontal displacement measured for the heel, the toe and the base slab are plotted against the horizontal displacement measured at mid height of bond beam in Fig. 4.12.

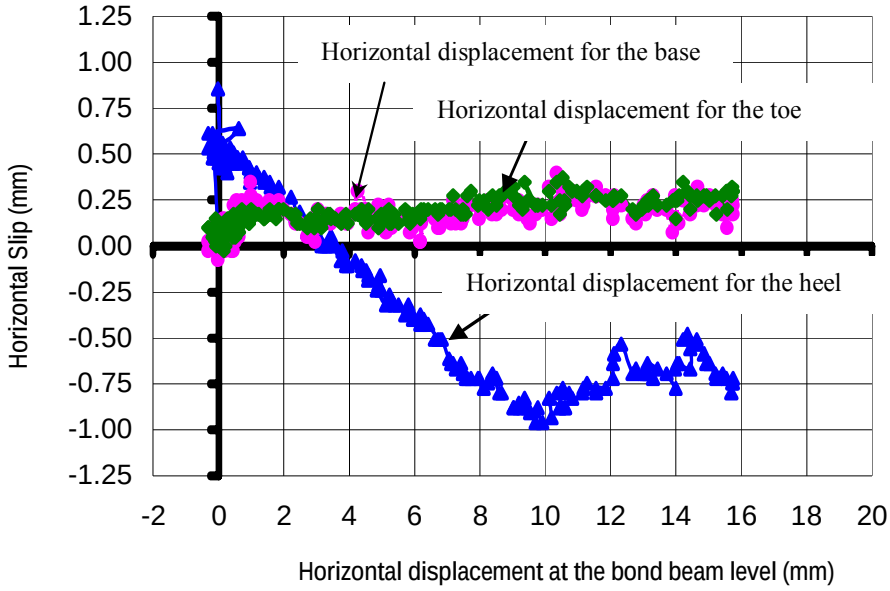

Figure 4.12: Horizontal displacements of a wall at base level

Horizontal displacements of the heel, the toe and the base slab were measured from channels 6, 7 and 8 respectively. Fig 4.12 exhibits that the horizontal slip of the base slab relative to the strong floor of the HTL was considerably small (maximum of 0.35mm), however, the slip was subtracted from the wall displacement measured at the bond beam level for plotting the load-displacement curves.

The negative horizontal displacement at the heel (location 6) is entirely understandable as the cracked heel tend to rotate clockwise under the top left horizontal load. The much smaller toe (location 7) horizontal displacement partly nullified the negative heel horizontal displacement. Effectively it could be said that there was no base sliding mechanism of failure noticed in the WSRM walls. However, the average value of the horizontal displacement at the toe and the heel was subtracted from the total displacement measured at locations 2, 3 and 4 to plot the true load-displacement behaviour of the walls. Horizontal deformation at the toe and the heel of the walls is presented further in detail in Chapter 5.

Typical vertical deformations of the toe and the heel of the walls are shown in Fig. 4.13.

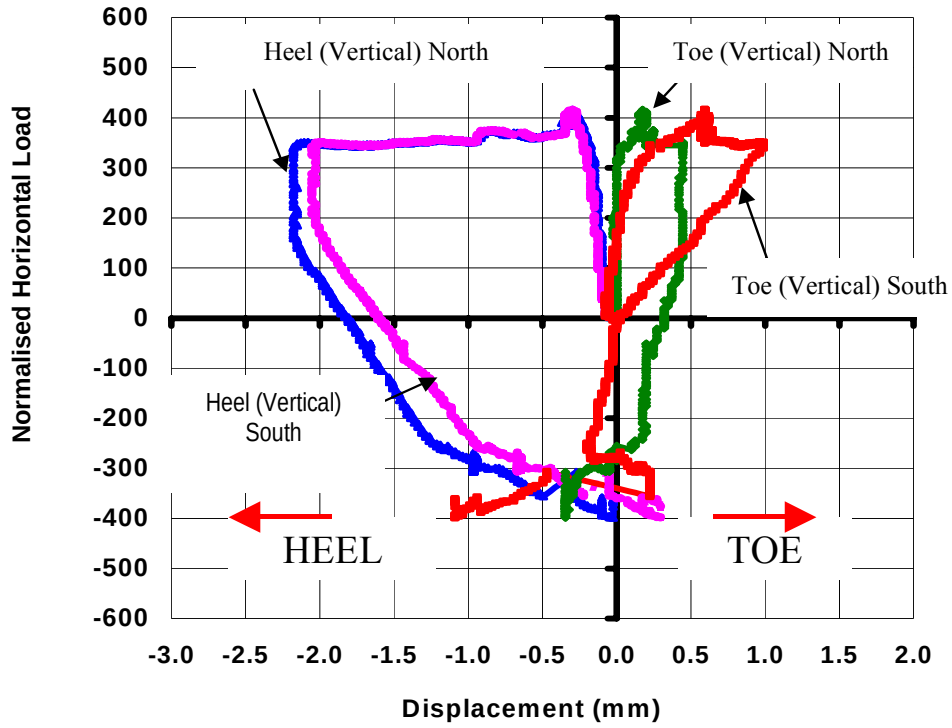

Figure 4.13: Vertical deformation of the toe and the heel of a wall

Under monotonic loading in the forward direction, channels 9 and 10 recorded the vertical deformation at the heel of the walls whereas channels 11 and 12 recorded the vertical deformation at the toe of the walls. When the load was reversed, the toe turned into the heel and the heel turned into the toe.

It is noticed from Fig. 4.13 that the vertical deformations at the heel were higher (crack opening) than that at the toe (crack closure). Vertical deformations of the toe and the heel of the walls are elaborated further in Chapter 5.

Typical horizontal, vertical and diagonal deformations at the centre (see Fig. 4.7) of the wall are plotted in Fig. 4.14. The average value of deformation measured from channels 13&16, 15&18

and 14&17 provided the vertical, the horizontal and the diagonal deformations respectively at the centre.

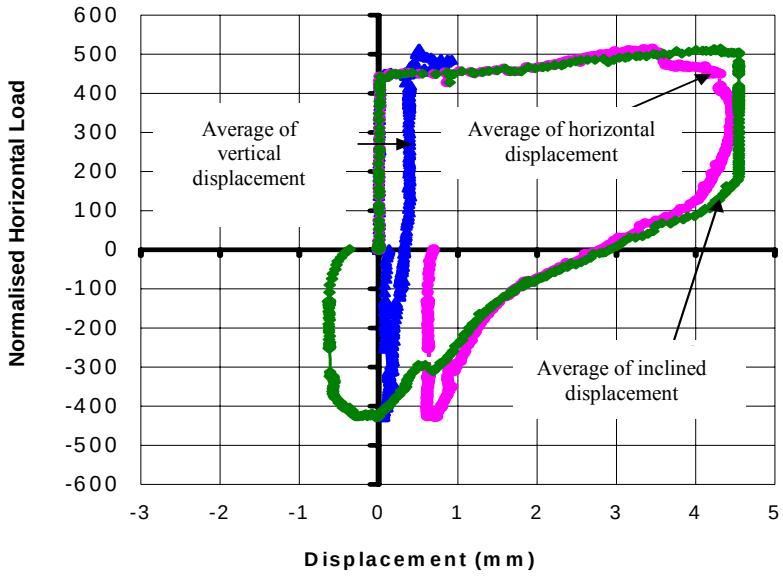

Figure 4.14: Magnitude of deformation at the centre of wall

It is clear from Fig. 4.14 that the magnitude of diagonal deformation (average of 14 & 17) and the horizontal deformation (average of 15 & 18) are larger than the vertical deformation, indicating dominance of applied horizontal racking load and the diagonal shear failure at the centre of the walls. Vertical deformation at the centre of the walls was the smallest due to presence of the constant vertical load.

Similar to other deformation data, deformation along the full length of the diagonals was also recorded in millimetres by the LabVIEW (2004) program. Load-diagonal deformation for the WSRM (#7, #8) walls tested under monotonic and cyclic loading is shown in Fig. 4.15. Deformations along two diagonals under forward monotonic and reverse monotonic loading are shown in Fig. 4.15(a), whereas deformations along two diagonals under cyclic loading are shown in Fig. 4.15(b). These figures show that the diagonals of the walls under both monotonic and

cyclic loading were elongated or shortened approximately 10mm at the ultimate load stage, exhibiting occurrence of major damage along the diagonal, a typical shear failure mechanism.

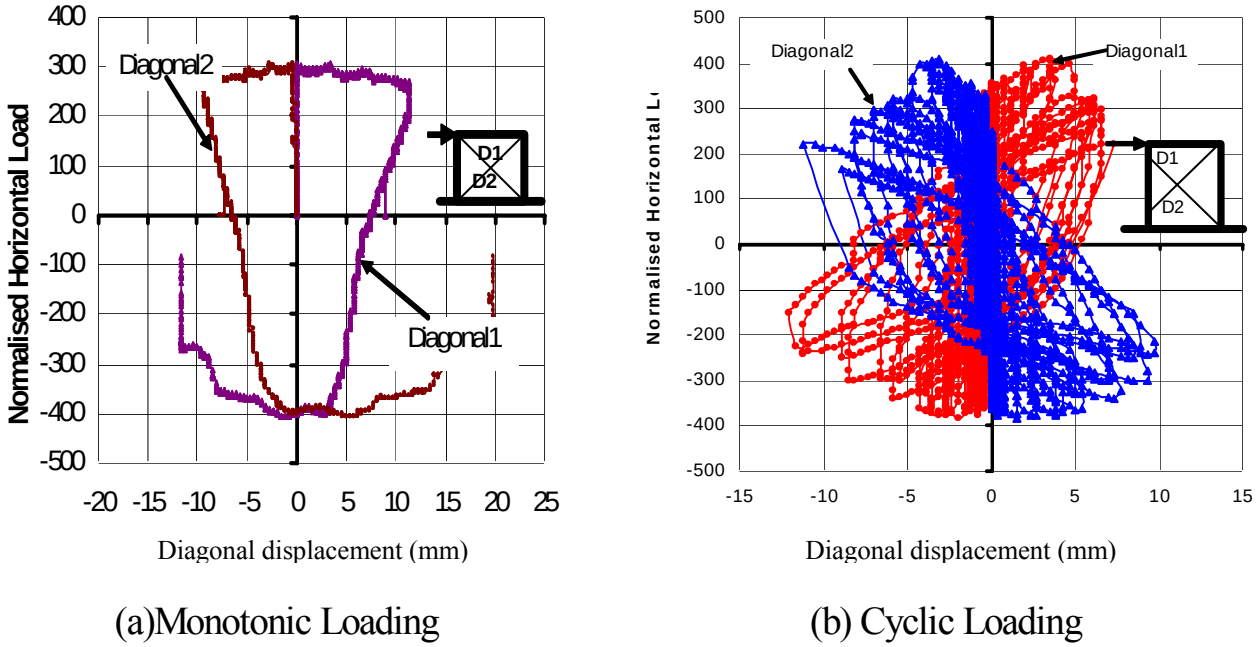

Figure 4.15: Typical diagonal deformation of the walls

Under both monotonic and cyclic loading, when one diagonal was under compression the other was under tension. Obviously these deformations are larger than the diagonal deformations measured at 200mm gauge length (shown in Fig. 4.14). It is evident from this figure that the walls exhibited significant diagonal deformation. Diagonal deformations of the walls are discussed in detail in Chapter 5.

Eccentricities (to the thickness direction) in either vertical or the lateral loading could cause out-of-plane deformation affecting the inplane behaviour of shear walls adversely. To ensure perfect inplane response, the out-of-plane deformation at the centre was measured using an independently mounted LVDT as shown in Fig. 4.16. Only the first four walls were instrumented with this LVDT.

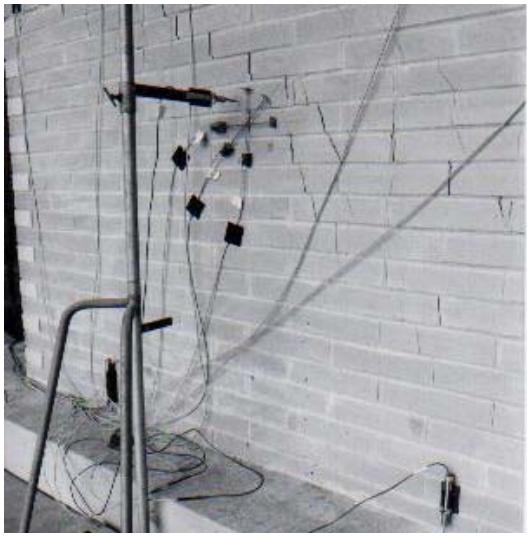

Figure 4.16: Measurement of potential out-of-plane deformation of shear walls

All of the four walls showed absolutely no tendency for out-of-plane deformation. As strict inplane behaviour was ensured, this measurement was dispensed with for the rest of walls tested.

4.6 Failure of Walls

Regardless of the spacing of the vertical reinforcement, all walls cracked along the loaded diagonal. With the increase in the horizontal displacement, crack width increased for almost the whole length of the diagonal crack. This observation is consistent with the cracking hypothesis made from the results of the elastic analyses presented in Chapter 3. In general, all walls exhibited stepped diagonal cracks. Similar crack patterns were observed under monotonic loading, cyclic loading and reverse monotonic loading. Failure patterns of the WSRM, the ECRM and the URM walls are presented in this section.

4.6.1 WSRM Walls

Under monotonic loading, all WSRM walls exhibited elastic behaviour until the onset of cracks. Initial cracks appeared along the loaded diagonal of the walls due to splitting of the vertical mortar joints and tension failure of the masonry units. With the gradual increase in the applied

horizontal displacement, the horizontal load increased. Under increasing monotonic displacement, all the WSRM walls exhibited true diagonal cracking passing through the grouted cores as shown in Fig. 4.17.

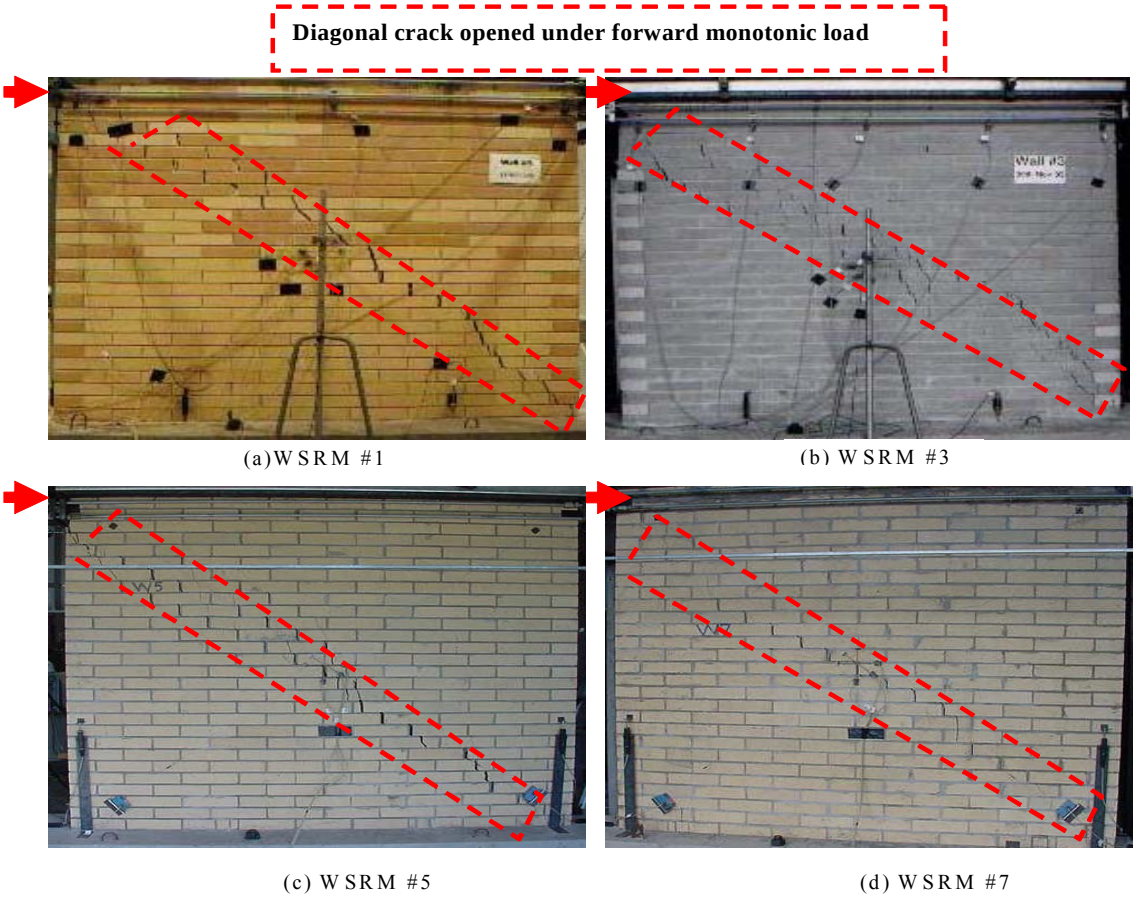

Figure 4.17: Crack patterns of WSRM walls tested under monotonic loading

Regardless of the position of the grouted cores, under monotonic loading the WSRM walls exhibited a single diagonal crack. Positioning of the vertical grouted cores in the WSRM walls appears not to have affected the final crack pattern as hypothesized in Chapter 3. It can be seen from Fig. 4.17 that, in addition to the mortar joints, the masonry units also failed in tension to provide a true diagonal crack. The final crack patterns of the WSRM walls tested under reverse monotonic loading are shown in Fig. 4.18.

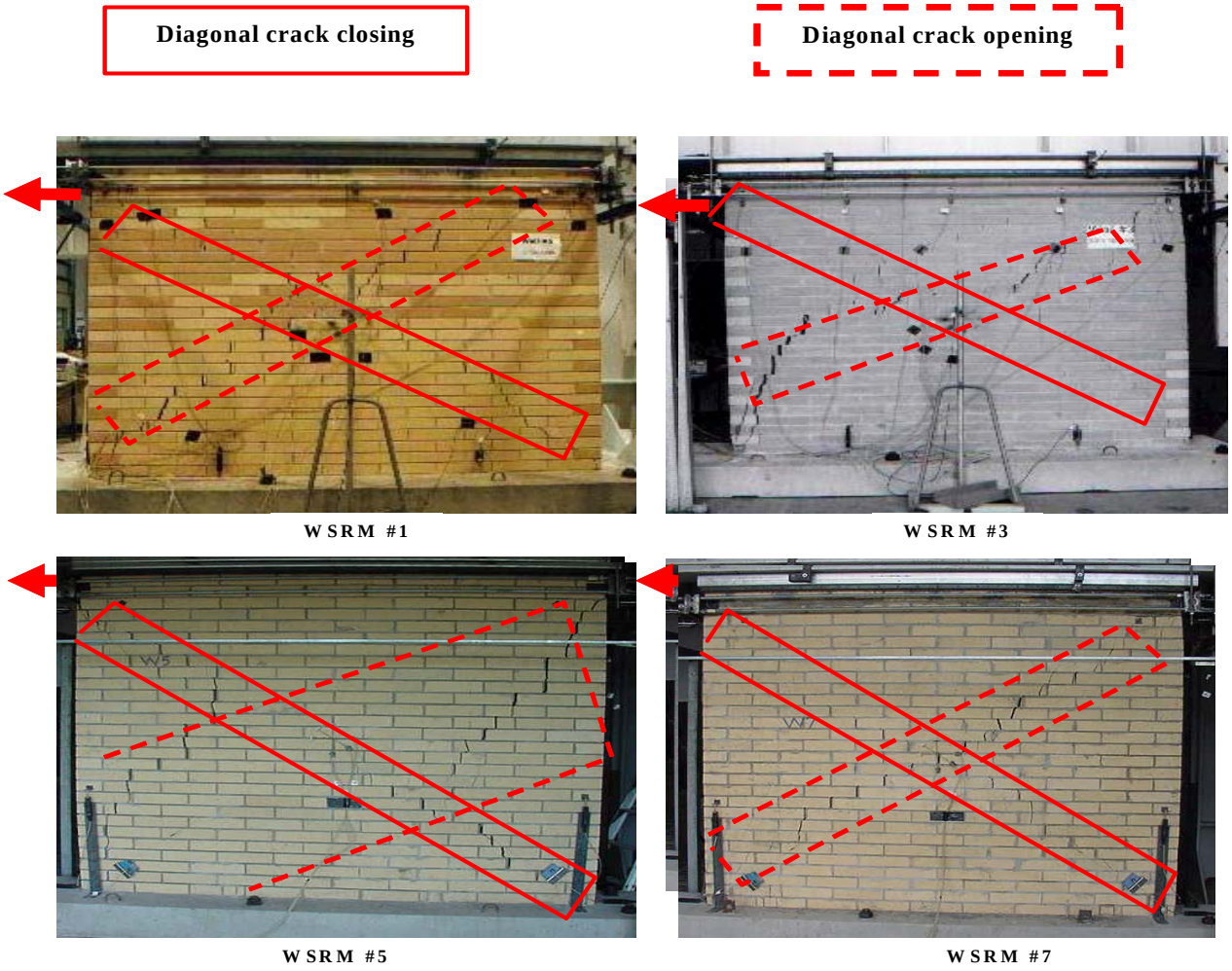

Figure 4.18: Crack patterns of WSRM walls tested under reverse monotonic loading

Under reverse monotonic loading, with the appearance of the diagonal crack along the opposite (loaded) diagonal the crack formed during the forward monotonic loading closed. Generally the crack formed due to the reverse monotonic loading was similar in shape to the crack due to forward monotonic loading, although the width of the diagonal crack zone varied due to the level of damage suffered by the walls during the forward loading. WSRM#5 exhibited a much wider crack zone due to reverse loading perhaps due to the larger applied displacement in the forward direction.

Under cyclic loading, the failure mode of the WSRM walls was similar to that observed under monotonic loading. Since the applied horizontal displacement was reversed after each small

increment during the entire loading history, two diagonal cracks occurred along the two opposite diagonals. Crack patterns of walls subjected to the cyclic loading are shown in Fig. 4.19.

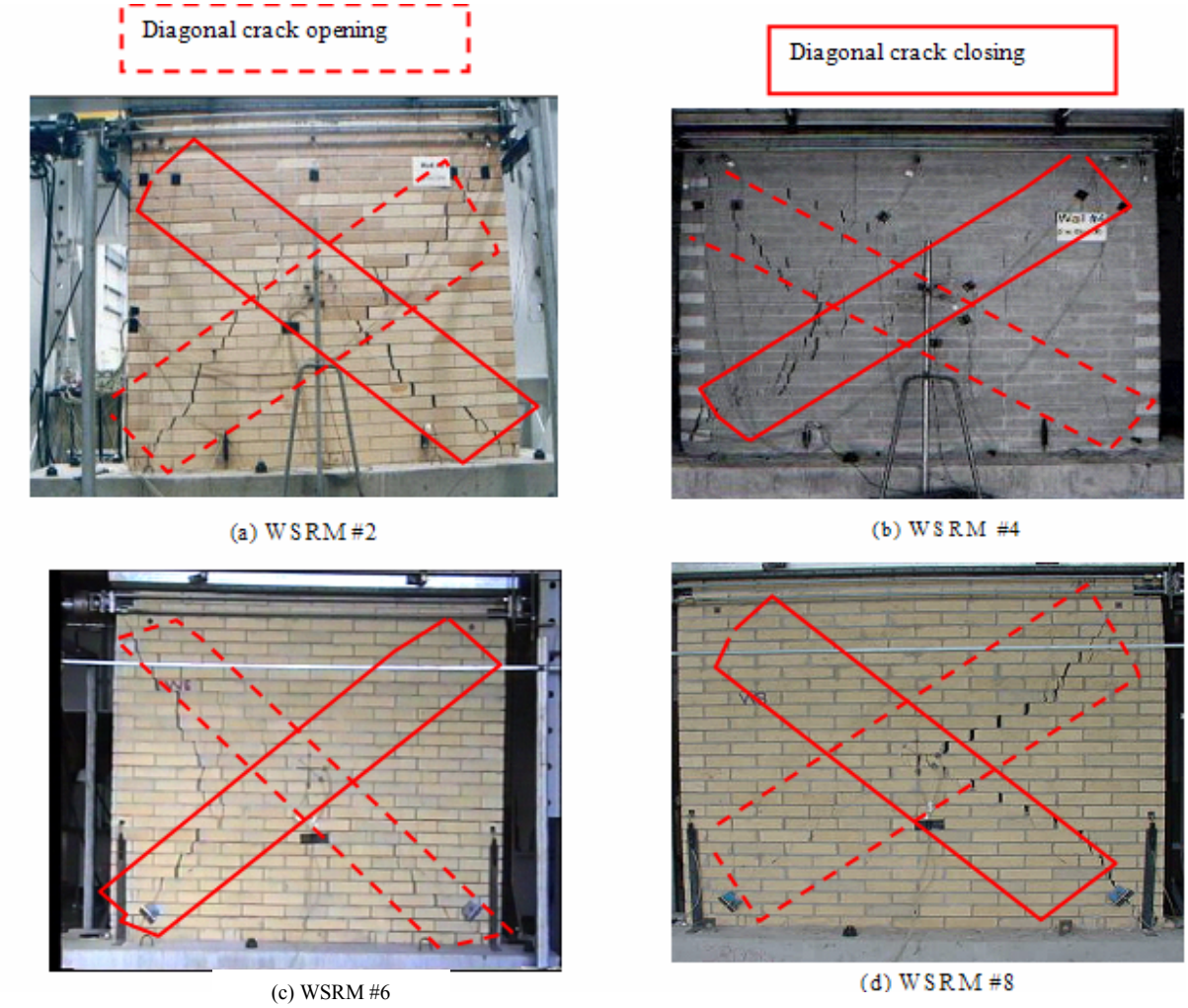

Figure 4.19: Crack patterns of WSRM walls tested under cyclic loading

Under cyclic loading both diagonal cracks propagated with the increase of the horizontal displacement in the forward and reverse directions, however, when one diagonal crack was opened the other was closed. Final crack patterns under cyclic loading were similar to those achieved under fully reversed monotonic loading. From this observation, it may be concluded that the type of loading history (monotonic or cyclic) did not affect the final crack patterns of the WSRM walls. The effects of spacing of the vertical reinforced cores also appeared to be insignificant to the behaviour/cracking of the WSRM walls.

Failure of the toe of the WSRM walls under monotonic and cyclic loading is shown in Fig. 4.20 and Fig. 4.21 respectively.

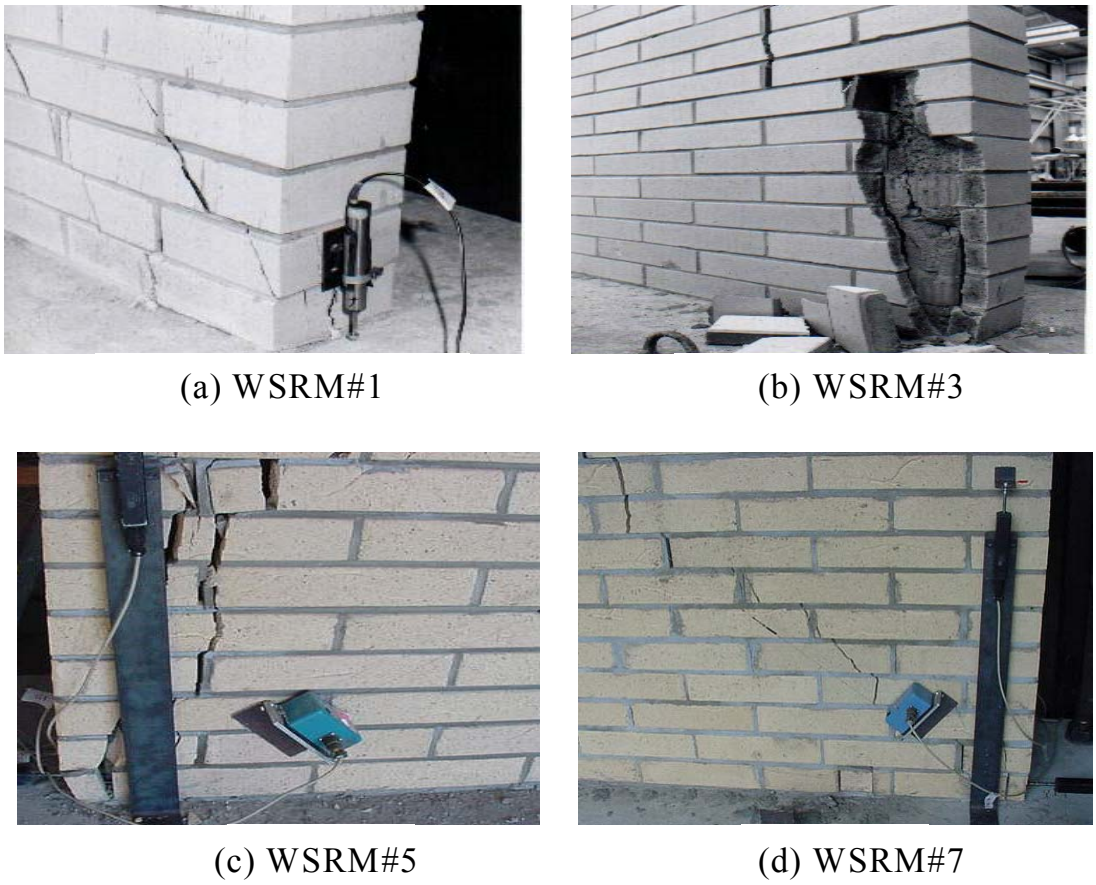

(a) WSRM#1 (b) WSRM#3

(c) WSRM#5 (d) WSRM#7

Figure 4.20: Toe crushing of WSRM walls under monotonic loading

Substantial deformation at the toe of the WSRM walls is evident from Figs. 4.20 and 4.21. The block shell around the toe of WSRM #3 was removed manually to examine the condition of the reinforced grouted cores. It is evident from Fig. 4.20(b) that the reinforced grouted cores exhibited vertical splitting and shells spalled off the units, typical of compression failure.

Like diagonal cracks, the cracks which appeared at the toe of the WSRM walls under monotonic and cyclic loading were also similar; however, the level of damage in different walls was different due to different final horizontal displacement (applied drift). Damage at the heel of the

walls was not significant. The measured horizontal and vertical deformations at the toe and the heel of the WSRM walls are presented in Chapter 5 of this thesis.

(a) WSRM #2

(b) WSRM #4

(c) WSRM #6

(d) WSRM #8

Figure 4.21: Toe crushing of WSRM walls under cycling loading

4.6.2 ECRM Walls

The ECRM wall was tested only under monotonic loading. At the initial stage of loading, cracks appeared along the loaded diagonal of the wall and, with the increase in the horizontal displacement, the crack width increased to the full length of the diagonals. Major cracking along the diagonal of the wall appeared under forward and reverse monotonic loading as shown in Fig. 4.22.

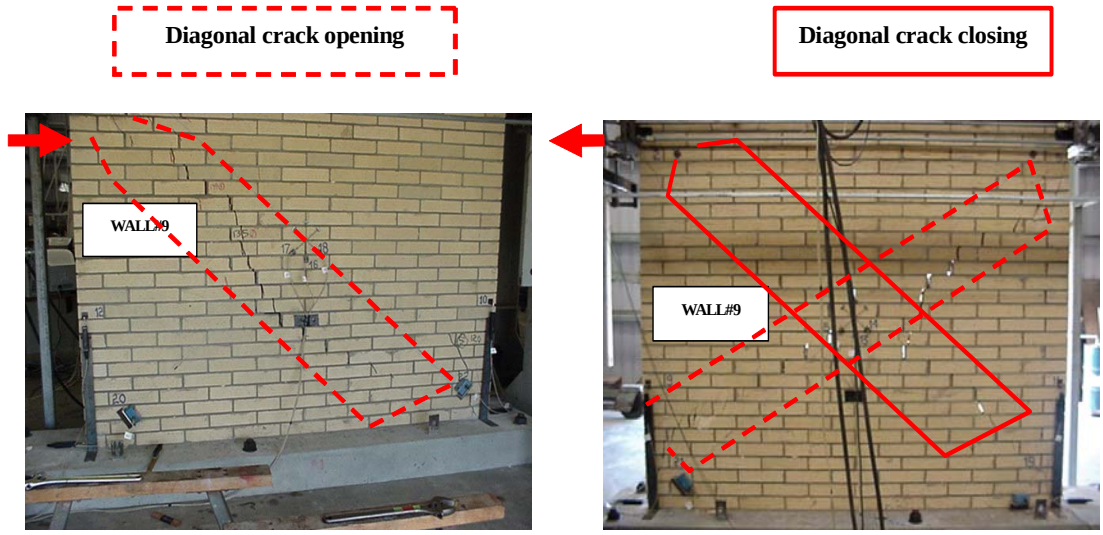

(a) Forward monotonic load **(b) Reverse monotonic load**

Figure 4.22: Final crack pattern of ECRM wall tested under monotonic loading

This pattern of cracks was similar to that observed for WSRM walls tested under reverse monotonic and cyclic loading (see Fig. 4.18 and Fig. 4.19). Failure of the toe of the ECRM walls is shown in Figure 4.23. Similar to the WSRM walls, the toe of the ECRM wall also exhibited significant deformation including bulging typical of compression failure. The horizontal and the vertical deformations of the toe of the ECRM walls are further discussed in Chapter 5.

Figure 4.23: Toe crushing of ECRM walls under monotonic loading

Like the WSRM walls, vertical splitting at the toe, spalling of shells, tension failure of masonry units and splitting of the vertical mortar joints were also seen in the ECRM wall.

4.6.3 URM Walls

The final crack pattern of the URM wall at the ultimate stage is presented in Fig. 4.24.

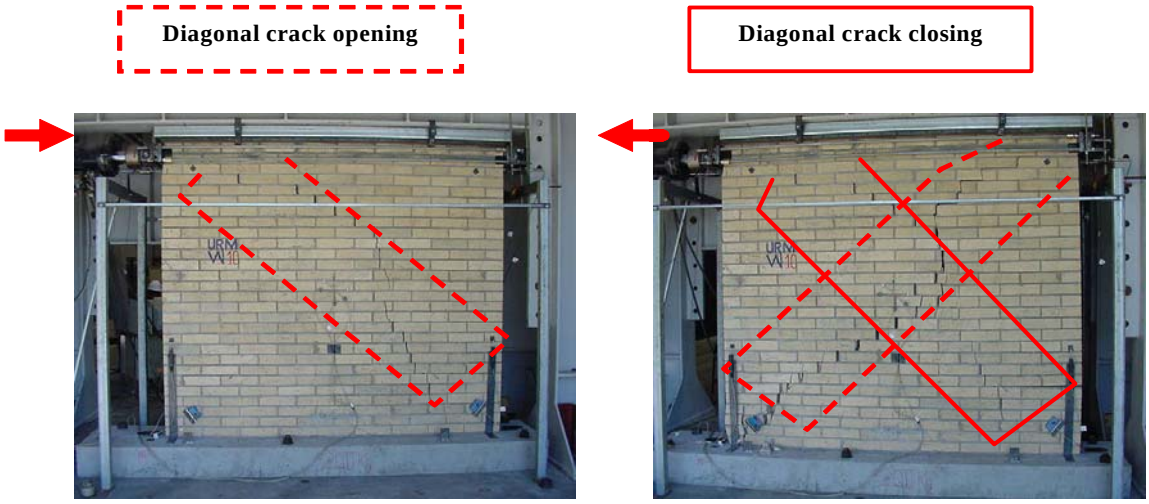

Figure 4.24: Final crack pattern of URM wall tested under monotonic loading

Similar to the WSRM and the ECRM walls, cracks appeared along the loaded diagonal of the URM wall and, with the increase in the horizontal load, the width of the cracks increased for the full length of the diagonal. The URM wall reached its maximum shear capacity upon its toe failure. After reaching the peak load, the URM wall exhibited brittle failure with the associated sliding and rocking behaviour leading to larger toe deformation.

Sliding and rocking types of failure of URM have also been observed by other researchers (Zhuge (1995), Mahmoud et al. (1995), Drysdale and Hamid (1983)). Perhaps the presence of 0.5MPa vertical stress has prevented large sliding/rotation in our tests. Width of cracks in the

middle of the wall was greater than in other regions and was up to 25mm at the final stage of the test.

Unloading in the forward direction and then loading in the reverse direction allowed the first diagonal crack to close and a new crack to open along the opposite diagonal.

Failure of the toe and the heel of the URM wall is shown in Fig. 4.25.

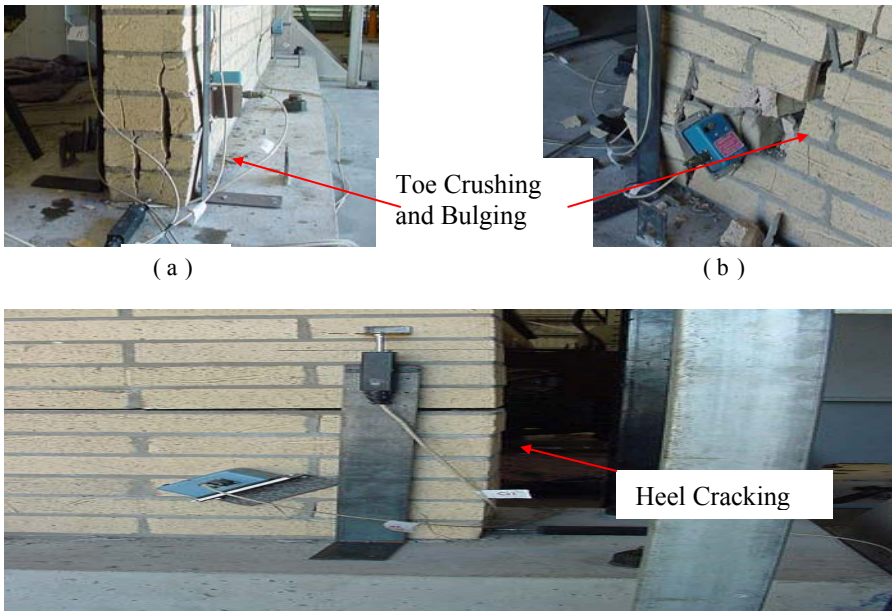

Figure 4.25: Toe crushing and heel splitting of URM wall

Fig. 4.25(a) is exhibiting vertical splitting at the toe of the URM wall, a typical compression failure. From Fig. 4.25(b), it is evident that the toe of the URM wall exhibited substantial deformation including bulging. The horizontal and the vertical deformation at the toe and the heel of the URM wall are presented further in Chapter 5. Fig. 4.25(c) is showing that the heel of the URM wall split horizontally between courses six and seven. This mechanism was not prominent in the WSRM and the ECRM walls. The URM wall exhibited this behaviour since it did not have any grout or reinforcement in the end vertical cores whereas the WSRM and the ECRM walls always had vertical reinforced grouted cores at the ends.

One of the reasons for the horizontal crack not appearing in the joint subjected to maximum bending is the confining effect of the large concrete footing on the bottom joints. A similar effect is reported by Assa and Dhanasekar (2000) on the behaviour of reinforced concrete columns tested under axial and lateral loading.

4.7 Summary

In this experimental program, ten clay block masonry walls were constructed and tested under either monotonic or cyclic loading. Among these walls, eight were WSRM walls, one was an ECRM wall and one was a URM wall. Four of the WSRM walls were tested under cyclic loading and the other four walls were tested under monotonic loading. The design, construction, curing, handling and test procedures adopted during testing of these walls have been explained in this chapter. Material properties of the mortar, grout, masonry prism, and masonry units have also been provided.

The arrangement of boundary conditions conforming to cantilever shear walls, positioning of data sensors, and details of the data acquisition program used for the testing of the walls are also included. The spacing of the vertical reinforcement was the only parameter that was varied to examine the behaviour of the WSRM walls. A moderate value of vertical compression (0.5 MPa) was maintained during application of the horizontal load until failure. Final crack patterns of the WSRM, the ECRM and the URM walls are presented and discussed.

This experimental study has shown that the WSRM, the ECRM and the URM walls exhibited damage along the loaded diagonal of the walls.

It has been found that one major crack appeared along the loaded diagonal during both the forward loading of the monotonic as well as the cyclic loading histories. A second crack along the opposite diagonal appeared when the direction of loading was reversed. Therefore, the final

crack pattern under cyclic loading was similar to that under reverse monotonic loading. The diagonal cracks closed and opened with the increment of horizontal displacement in the forward and reverse direction during cyclic loading, whereas one diagonal crack appeared during forward monotonic loading and a second crack appeared along the opposite diagonal when the direction of monotonic loading was reversed. Similar diagonal crack patterns were found under monotonic and cyclic loading irrespective of the spacing of the vertical grouted reinforced cores.

In the URM wall, higher toe and heel deformations were found than those in WSRM and ECRM walls. This was due to the lack of grouted cores at the ends of the URM wall. All WSRM and ECRM walls had reinforced grouted cores at the ends and hence exhibited smaller deformations at the toe and the heel.

CHAPTER 5

ANALYSIS OF EXPERIMENTAL DATA

5.1 Introduction

The experimental study carried out to investigate the behaviour of masonry shear walls provided data on the lateral shear load capacity, the ductility and damage characteristics. The data collected from the experiments are analysed and reported in this chapter. Behaviour of the WSRM walls was investigated and compared with that of the ECRM and the URM walls.

The load-displacement curves obtained from the tests were first smoothed to draw envelope curves and then the behaviour was assessed. The effect of loading history (monotonic/cyclic) to the overall behaviour is discussed. Damage characteristics such as the stiffness degradation, the diagonal deformation, and the deformations at the toe, the heel and the centre zones were examined with reference to the overall drift of the shear walls with the increasing lateral loading. The effects of spacing of the vertical reinforced cores to the overall behaviour of WSRM walls are discussed and conclusions drawn.

Shear capacities of the walls predicted by different empirical equations are also reported and compared with the experimental capacity.

5.2 Load-Displacement Response

The walls exhibited elastic behaviour until the onset of micro-cracks. With the increase in horizontal displacement, the heel region of the walls failed in tension due to limited tension

capacity of the masonry, which transferred the tensile stresses to the embedded steel. The walls subsequently exhibited hardening behaviour. At the same time, compressive stresses in the toe region of the walls increased nonlinearly whereas the shear stresses dominated the loaded diagonal region. With further increase in the horizontal displacement, cracks in the loaded diagonal region of the walls propagated leading to gradual reduction of the horizontal load. Under reverse monotonic loading, the pre-existing diagonal cracks closed and new cracks emerged along the current loaded (opposite) diagonal with the increase in the horizontal displacement in the reverse direction.

Under cyclic loading, cracks appeared along both diagonals of the walls. As the push and pull mechanism continued, the diagonal cracks were opening and closing. The width of the crack zone increased with the increased horizontal displacement. Both monotonic and cyclic loadings exhibited elastic regime, hardening regime, distinct peak load and softening behaviour.

Load and deformation data collected by the LabVIEW (2004) data acquisition program (presented in Chapter 4) were plotted to examine the behaviour of the walls. Displacement measured at channel 4 (see Fig. 4.7) was used to draw the horizontal load - displacement curve of the walls. Relative movement of the base slab measured through data channel 8 and the average value of the horizontal displacement at the toe (channel 7) and the heel (channel 6) although very small, were subtracted from the total value of the displacement measured at channel 4 to provide a true representation of load - deformation behaviour. Load-displacement curves of the walls without normalisation are provided in Appendix C.

Typical load-displacement behaviour of two WSRM walls is illustrated in Fig. 5.1 where the load-displacement curve obtained under the forward and the reverse monotonic loading are superimposed on the hysteretic loops obtained from the corresponding cyclic loading test. The monotonic loading curve could be regarded as one major cycle whereas the cyclic loading data

consisted of several hysteretic loops each regarded as a sub-cycle of the major cycle of the monotonic test curve.

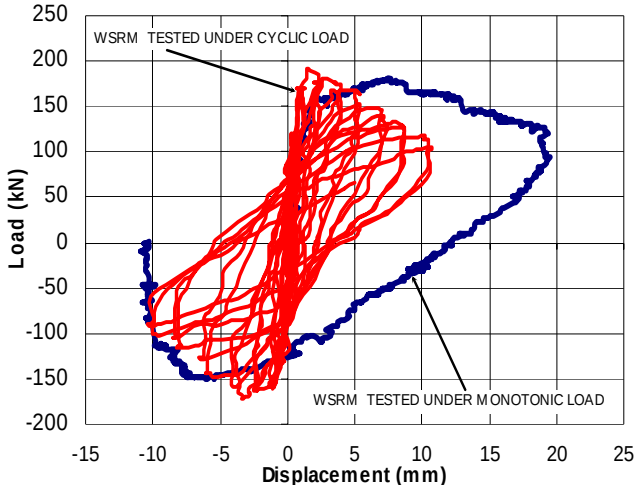

Figure 5.1: Typical horizontal load-displacement plot of WSRM walls

The load-displacement behaviour of the walls under cyclic loading may be better-explained using three load-displacement loops at the yield, the peak and the ultimate stages as shown in Fig. 5.2. These cycles are drawn using the normalised horizontal load (normalisation of the horizontal load is explained in Eq. 4.2 earlier and will be further discussed in section 5.2.1).

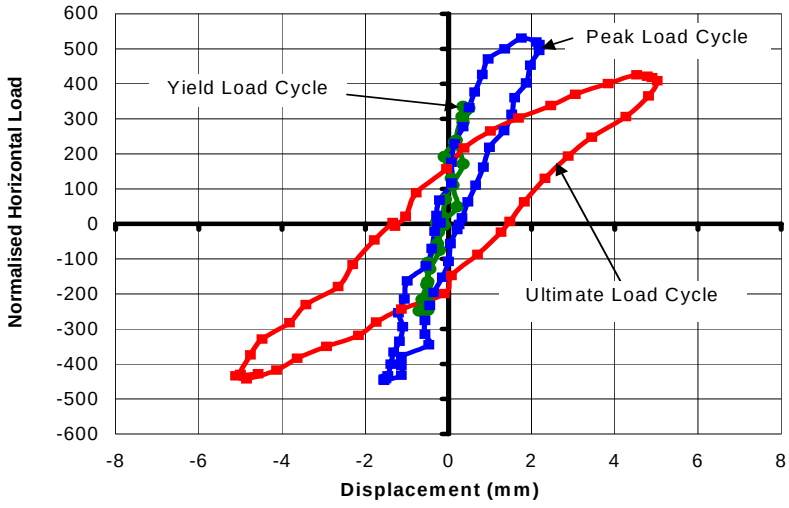

Figure 5.2: Hysteretic loops at yield, peak and ultimate loads

It has been observed that, until yield, the walls exhibited elastic behaviour and showed negligible residual displacement upon the removal of the applied horizontal load. With the increase in the displacement controlled loading cycles, the walls exhibited fattening of the hysteretic loops and reached the peak load stage at about 125% of the yield load. Beyond the peak load stage, the walls showed further increase in fattening of the hysteretic loops and substantial loss in the horizontal load capacity leading to the ultimate stage.

The typical cyclic load behaviour of masonry shear walls could be illustrated as shown in Fig. 5.3

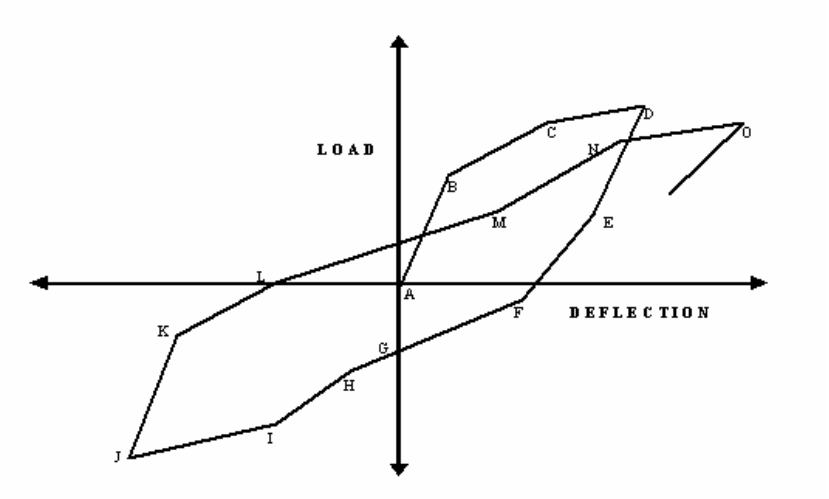

Figure 5.3: Failure mechanism of the WSRM walls under cyclic load test

On the load-displacement curve, segment ‘A-B’ represents the elastic behaviour until the onset of cracks; ‘B-C’ represents nonlinear behaviour due to material yielding and/or micro-cracking; ‘C-D’ portrays further hardening perhaps due to yielding of any tensile reinforcement; ‘D-E’ represents unloading, which exhibits a significant reduction in load with a small decrease of deflection; ‘E-F’ represents further reduction in load due to reduction in displacement (point ‘F’ shows significant residual deflection retained after removal of the full horizontal load and point ‘G’ shows the required load in the reverse direction to achieve zero deflection); ‘G-H’ represents

further increase in load in the reverse direction; 'H-I' depicts closing of crack surfaces during loading which is reflected by the change of slope during reloading; 'I-J' shows substantial increase in deflection similar to 'C-D'; 'J-K' and 'K-L' are similar to 'D-E' and 'E-F' respectively with point 'L' representing additional damage during reverse direction loading; 'L-M' represents the loading during the next cycle.

A similar behaviour of reinforced masonry shear walls and RC columns under cyclic loading has been reported in the literature (Park and Paulay (1975), Priestley and Elder (1982), Jihang et al. (1997), Tanuwidjaja and Dhanasekar (1998)).

5.2.1 Normalisation of Load and Smoothing of Curves

Although an attempt was made to keep the material properties the same for all the walls, variability was inevitable due mainly to workmanship and could not be avoided. The properties of the constituent materials for the walls provided in Table 4.2 exhibit significant variability. It was decided to use the shear strength of masonry, predicted empirically as a function of the square root of the compressive strength of the masonry as shown in Eq. 5.1 (Eq. 4.2 is reproduced here for convenience) to normalise the effect of the constituent properties of the test walls.

As per clause 5.4 of AS3600 (2001), the shear capacity of reinforced concrete walls is calculated using the square root of the characteristic compressive strength of concrete. Matsumura (1988) calculated shear capacity of reinforced masonry shear walls using the square root of the compressive strength of masonry. Fattal and Todd (1993b) also defined shear capacity of the partially reinforced masonry walls as a function of the compressive strength of masonry. Therefore, in this thesis, the shear capacity of WSRM walls is normalised using the square root of compressive strength of masonry.

$$\text{Normalised Horizontal Load} = \frac{\text{Inplane Horizontal Load}}{0.22\sqrt{f_m} \times \text{A}_\text{g}} \times 10^3 \qquad (5.1)$$

where 'f_m' is the compressive strength of a masonry prism in MPa, 'A_g' is gross cross-sectional area of the wall in mm^2 and the inplane horizontal load is shown in Newtons. A typical load - displacement curve obtained after normalisation for Group 2 (Wall#3 and Wall#4) of the WSRM shear walls is shown in Fig. 5.4. Normalised load-displacement curves are used in this chapter to compare the behaviour of the walls. However, the original load-displacement curves are provided in Appendix C.

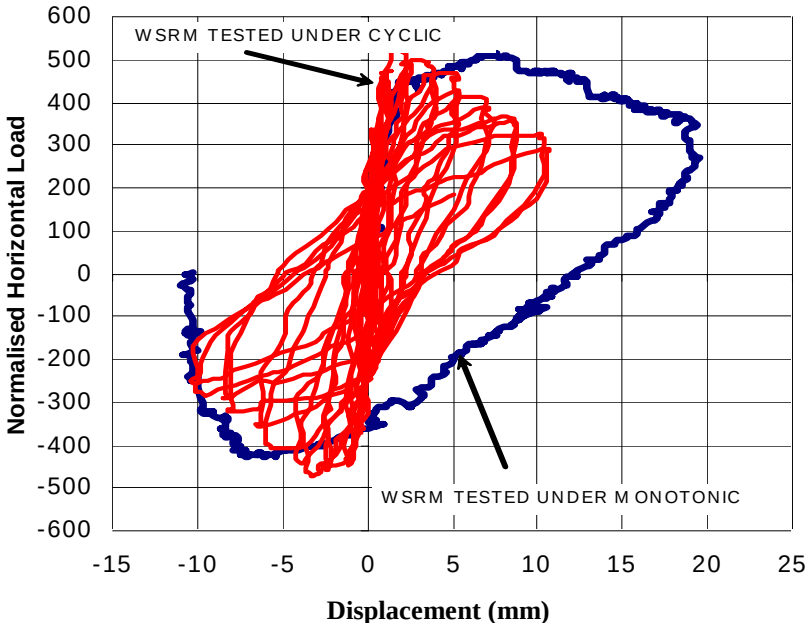

Figure 5.4: Typical normalised horizontal load-displacement curves

The actual load-displacement curve obtained from the experiment was not smooth and it was difficult to clearly define the peak, the yield and the ultimate load points; therefore, the curves have been smoothed to better understand the behaviour of the walls. All experimental load-displacement curves shown in this section are accompanied by the corresponding smooth curves.

5.2.2 WSRM Walls

Normalised horizontal load - displacement curves under forward and reverse monotonic loading for WSRM walls are discussed in this section. The actual experimental curves accompanied with their corresponding smoothed curves are presented in this section to understand the true behaviour of WSRM walls under monotonic and cyclic loading.

5.2.2.1 Group #1 Walls

The normalised horizontal-displacement curve accompanied by smoothed curves for wall WSRM#1 are shown in Fig. 5.5. The curve was smoothed only for the forward direction loading.

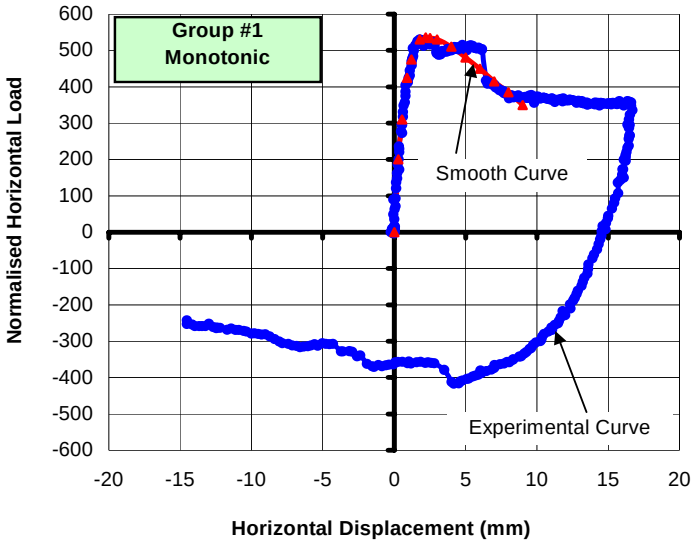

Figure 5.5: Load–displacement curve of WSRM #1

From the smoothed curve it is evident that the WSRM#1 wall reached peak horizontal load at a displacement of approximately 2mm and gradually lost its resistance to horizontal load. It lost 20% of the peak load (ultimate load) at a horizontal displacement of about 7mm. After 7mm of horizontal displacement, this wall was simply pushed under vertical compression exhibiting no significant change to its horizontal load-displacement curve and hence this phase is of no interest.

Upon reversal of the displacement controlled horizontal loading, the WSRM#1 exhibited approximately 2mm recovery in the horizontal displacement and was able to resist 80% of the peak load that was achieved under the forward monotonic loading.

Hysteretic loops of WSRM#2 tested under cyclic loading are shown in Fig. 5.6. Envelope curves consisting of peak load points of each hysteretic loop were drawn for ease of understanding of the behaviour of the WSRM walls under cyclic loading. The envelope curve was drawn only for the data points in the first quadrant of the hysteretic curves (consistent with the smoothed curve for monotonically loaded walls).

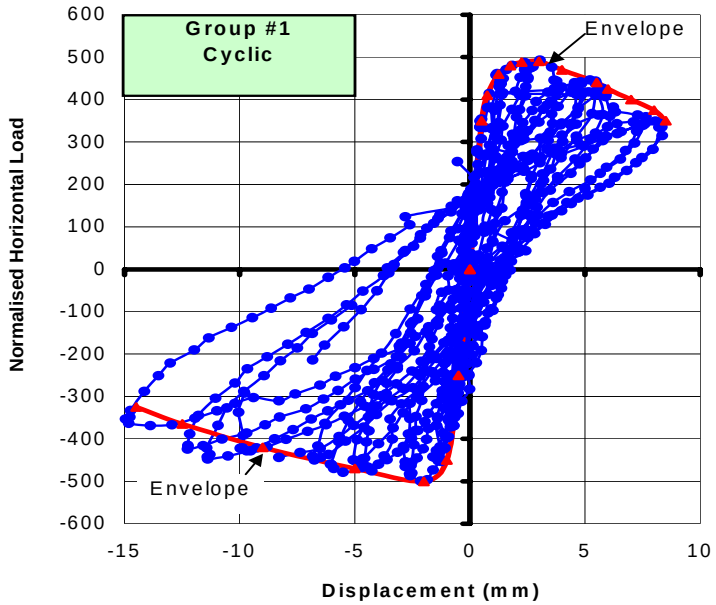

Figure 5.6: Load–displacement curve of WSRM#2

The WSRM#2 wall exhibited a peak normalised horizontal load of approximately “500” at a horizontal displacement of approximately 2.5mm both in the forward and in the reverse directions. This wall then exhibited a gradual loss in the horizontal lateral load capacity and reached ultimate load stage at about 9mm and 9.5mm horizontal displacement in the forward and reverse directions respectively.

The normalised smooth horizontal load-displacement curve (forward direction loading) of the WSRM#1 wall is superimposed on the normalised smooth load-displacement envelope of the WSRM #2 wall as shown in Fig. 5.7. The smooth curve achieved for monotonic loading matches well with the smooth envelope obtained from the cyclic loading test. It is evident from Fig. 5.7 that WSRM#1 and WSRM#2 walls exhibited a similar softening trend. Effect of loading history (monotonic/cyclic) was therefore considered not significant.

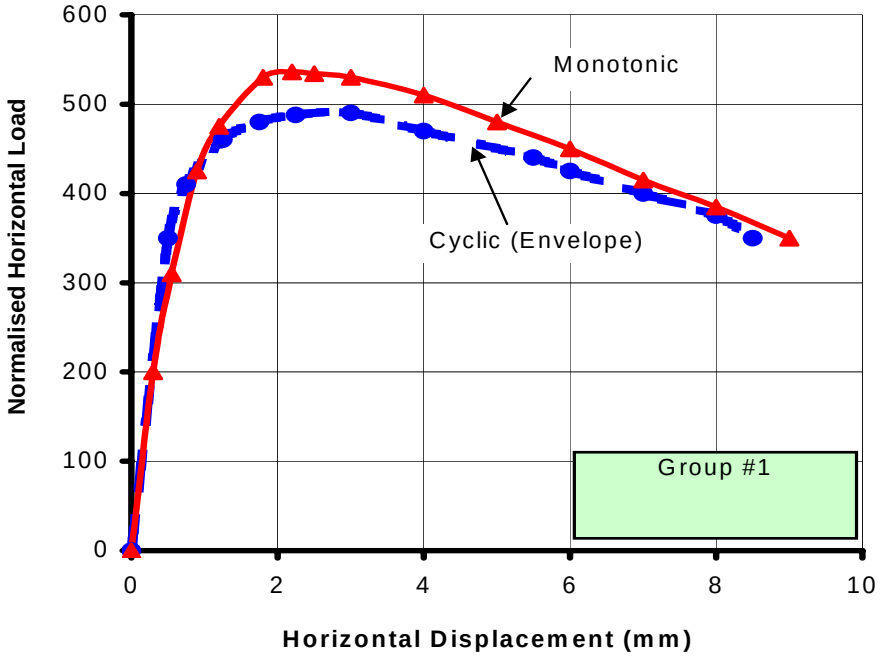

Figure 5.7: Load–displacement curves of WSRM#1 and WSRM#2

5.2.2.2 Group #2 Walls

Spacing between the two vertical reinforced cores at the middle of WSRM#3 and WSRM#4 walls was equal to 780m that divided the walls into three unreinforced masonry panels. The experimental horizontal load-displacement curve for WSRM#3 accompanied by its smooth curve is presented in Fig. 5.8. This wall exhibited hardening before it reached the peak horizontal load at a displacement of approximately 2mm. After the peak point, this wall exhibited softening

behaviour and gradually reduced its resistance to the horizontal load. Peak horizontal load dropped to 80% at a horizontal displacement of about 10mm.

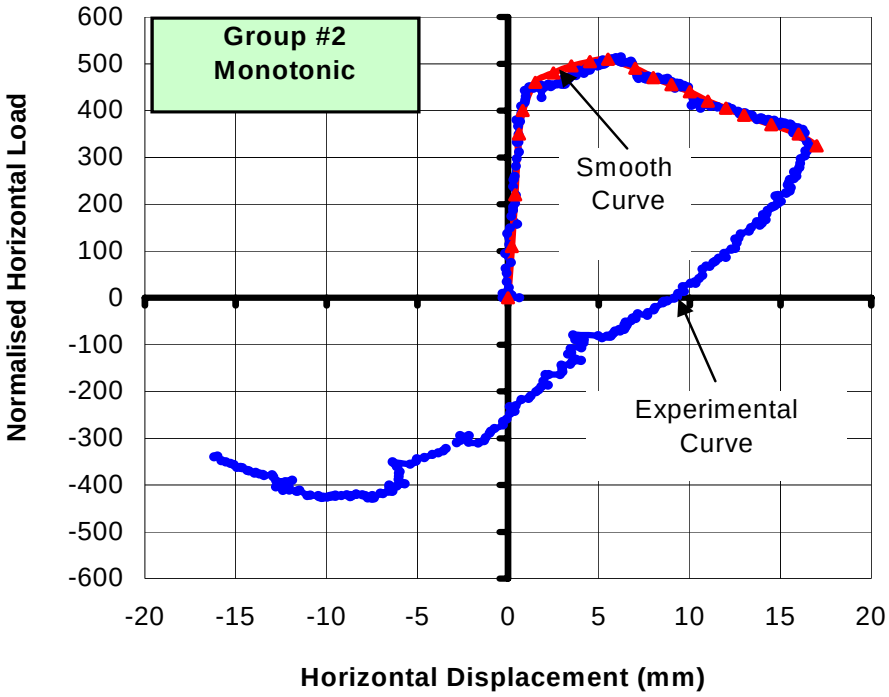

Figure 5.8: Load–displacement curve of WSRM#3

The WSRM#3 wall required reversal of 8mm of horizontal displacement to relieve fully the entire horizontal load. In the reverse direction, the wall exhibited a maximum 80% of the peak load achieved under forward monotonic loading similar to WSRM#1.

Hysteretic loops of WSRM#4 under cyclic loading accompanied by the smooth envelope curves are presented in Fig. 5.9.

The WSRM#4 wall reached peak horizontal load at approximately 2mm and 3mm of horizontal displacement in the forward and the reverse directions respectively. It lost 20% of its peak horizontal load at a horizontal displacement of 6mm and 7mm in the forward and reverse directions respectively. However, the peak horizontal load was similar under both the forward and reverse directions.

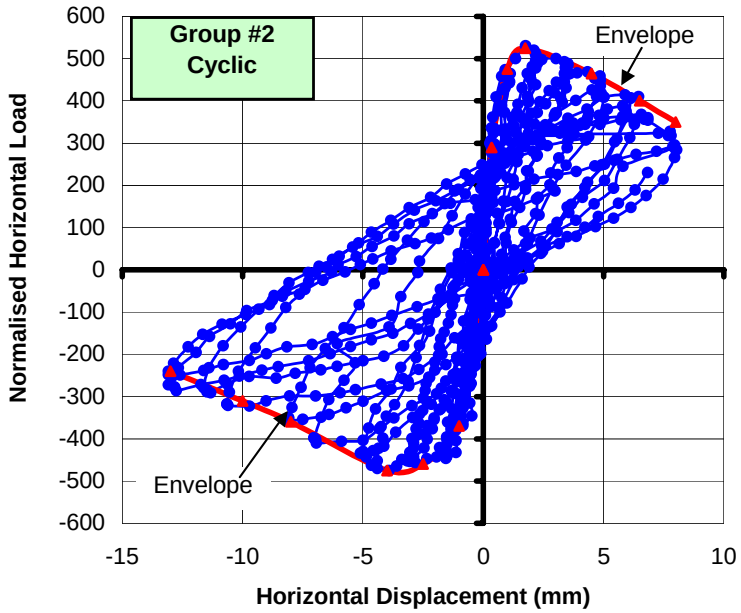

Figure 5.9: Load–displacement curve of WSRM#4

The normalised smooth monotonic loading curve for WSRM#3 and the envelope curve of WSRM#4 are presented in Fig. 5.10. It can be seen that that these two walls have exhibited their peak horizontal load very close to each other although the rate of reduction of the horizontal load under monotonic and cyclic loading was marginally different. WSRM#4 tested under cyclic loading degraded faster than the monotonically loaded WSRM#3.

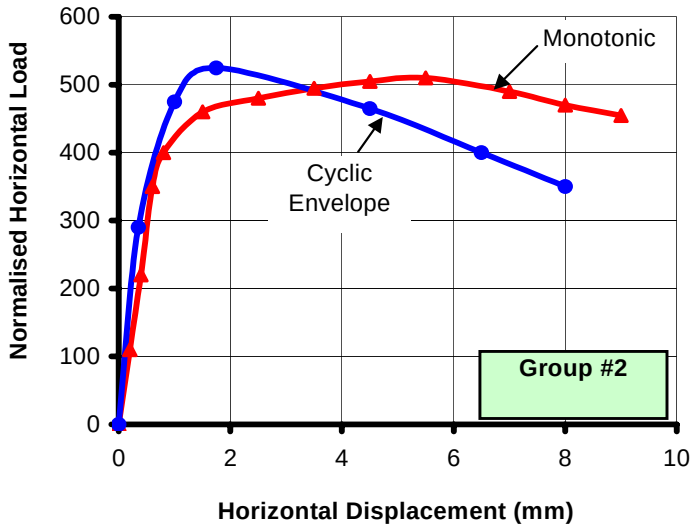

Figure 5.10: Load–displacement curves of WSRM#3 and WSRM#4

5.2.2.3 Group #3 Walls

Spacing between the two vertical reinforced cores at the middle of WSRM#5 and WSRM#6 walls was equal to 1140m that divided the walls into three unreinforced masonry panels. The horizontal load-displacement curve for WSRM#5 under monotonic loading accompanied by its smooth curve are shown in Fig. 5.11. WSRM#5 reached the peak horizontal load at a horizontal displacement of approximately 3mm. After the peak load stage, it showed gradual reduction in the horizontal load.

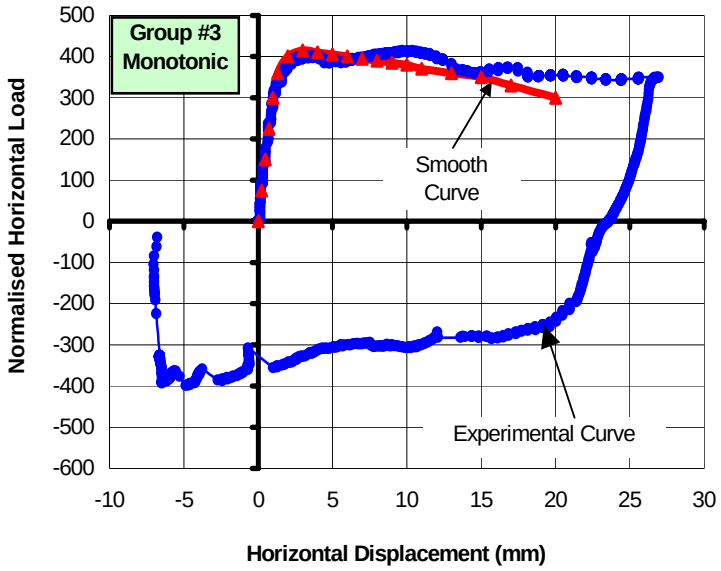

Figure 5.11: Load–displacement curve of WSRM#5

The load-displacement curve did not exhibit significant change after 15mm of horizontal displacement; it appeared that the wall was pushed under the displacement controlled horizontal load in the presence of vertical compression. A smooth curve was extrapolated to read the ultimate horizontal displacement at 80% of the peak horizontal load as shown in Fig. 5.11. Under reverse monotonic loading the peak horizontal load was equal to that under forward monotonic loading.

Hysteretic loops achieved under cyclic loading for WSRM#6 are shown in Fig. 5.12.

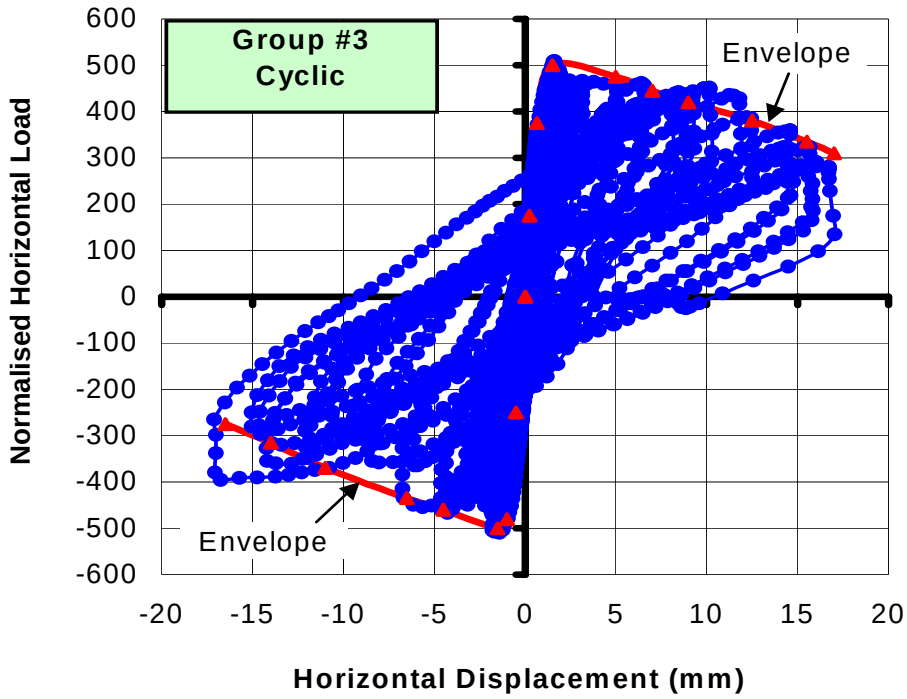

Figure 5.12: Load–displacement curve of WSRM #6

The WSRM#6 wall reached the peak horizontal load at approximately 2mm of horizontal displacement. WSRM#6 exhibited gradual loss of the horizontal load and reached the ultimate load stage at a horizontal displacement of 10mm under both the forward and reverse loading.

The normalised smooth monotonic load-displacement curve of WSRM#5 and the envelope curve of WSRM#6 are presented in Fig. 5.13. It is noticed from this figure that WSRM#6 exhibited 18% more peak horizontal load than that for WSRM#5 which is different to the other two groups of walls for which results have been discussed in sections 5.2.2.1 and 5.2.2.2. The softening trends of WSRM#5 and WSRM#6 are marginally different with the cyclically loaded wall degrading faster.

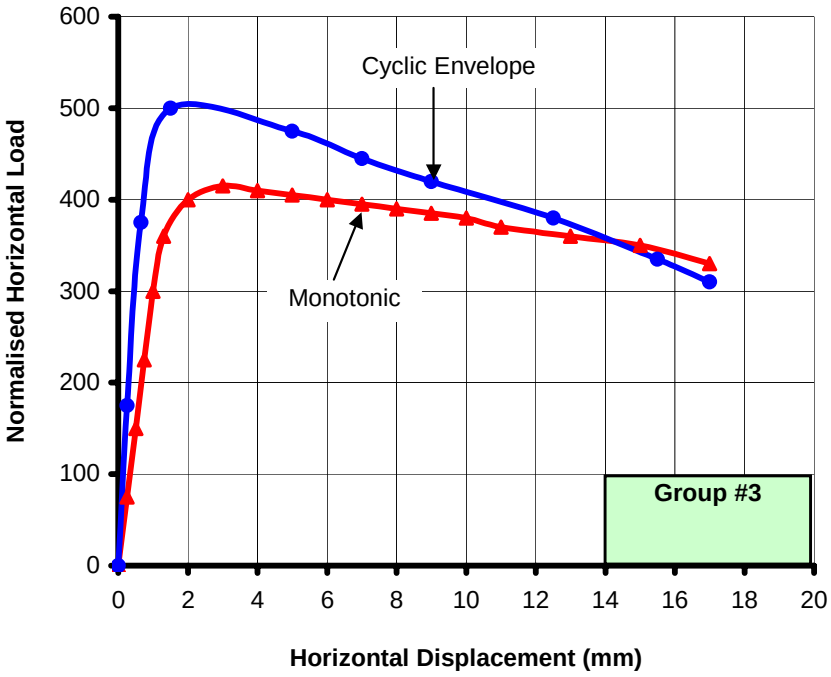

Figure 5.13: Load–displacement curves of WSRM#5 and WSRM#6

5.2.2.4 Group #4 Walls

Spacing between the two vertical reinforced cores at the middle of WSRM#7 and WSRM#8 walls was equal to 2000m that divided the walls into three unreinforced masonry panels. The monotonic loading curve for WSRM#7 accompanied by its smooth curve is shown in Fig. 5.14. It is clear from the figure that WSRM#7 exhibited a peak horizontal load at a horizontal displacement of 3mm in the forward direction.

The load-displacement curve did not exhibit significant change after 5mm of horizontal displacement; it appeared that the wall was pushed under the displacement controlled horizontal load in the presence of the vertical compression. At 5mm of horizontal displacement, the drop in the peak horizontal load was only 4% in contrast to the required 20% for the ultimate load stage. The smooth curve was, therefore, extrapolated to read the ultimate horizontal displacement as shown in Fig. 5.14. Displacement read from the extrapolated smooth curve at 80% of peak load was equal to 10mm.

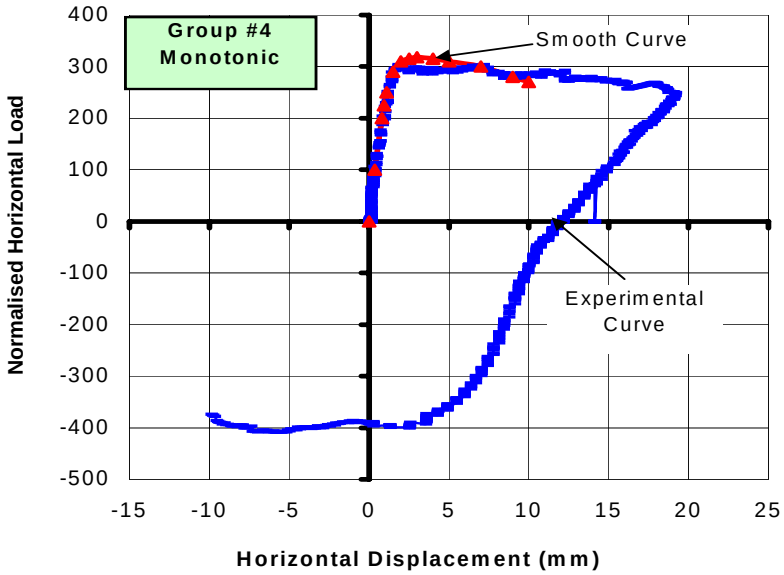

Figure 5.14: Load–displacement curve of WSRM#7

Hysteretic loops of the WSRM#8 wall along with smooth envelope curves are shown in Fig. 5.15. The peak horizontal load was reached at approximately 5mm of horizontal displacement in the forward direction and at about 4mm in the reverse direction. After reaching the peak load, the WSRM#8 wall exhibited gradual reduction in the horizontal load and reached the ultimate load stage at a horizontal displacement of 9.5mm in the forward and reverse directions.

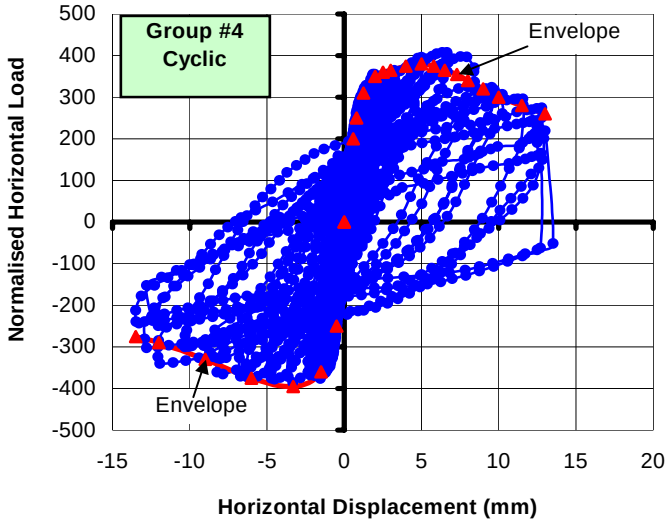

Figure 5.15: Load–displacement curve of WSRM#8

The normalised smooth monotonic curve of WSRM#7 and the envelope curve of WSRM#8 are presented in Fig. 5.16.

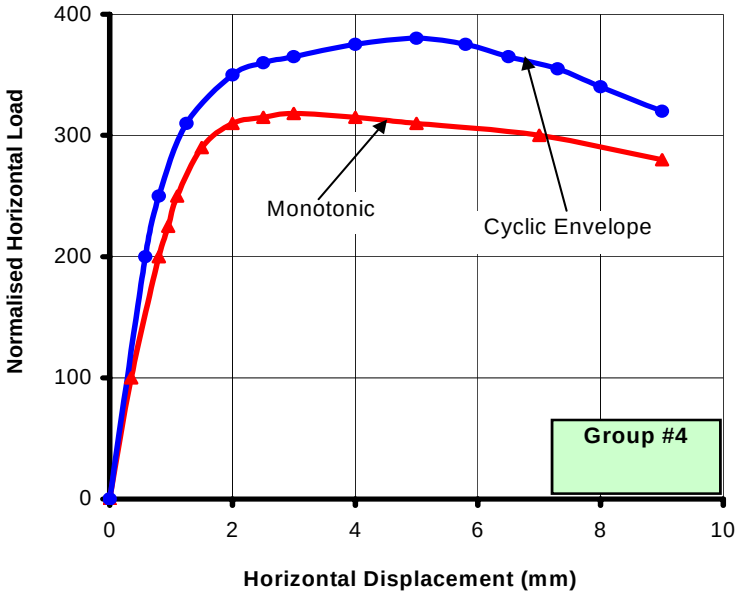

Figure 5.16: Load–displacement curves of WSRM#7 and WSRM#8

It could be seen from Fig. 5.16 that WSRM#8 exhibited 20% higher peak horizontal load than that for WSRM#7, however, their softening trends were similar.

5.2.3 Group #5 Wall (ECRM)

The ECRM wall (Wall #9) had vertical reinforced cores only at the ends with a large unreinforced masonry panel of width 2700mm. The monotonic load-displacement curve of this wall accompanied by its smooth curve is shown in Fig. 5.17(a). The ECRM wall reached its peak normalised load of "335" at a horizontal displacement of approximately 2mm in the forward direction and at 4mm in the reverse direction. The normalised peak horizontal load in the forward and the reverse directions were close to each other. The load-displacement curve of the ECRM wall in the forward direction is shown in Fig. 5.17(b). It can be noticed from this figure that this wall reached its ultimate load of "270" at approximately 8mm of horizontal displacement.

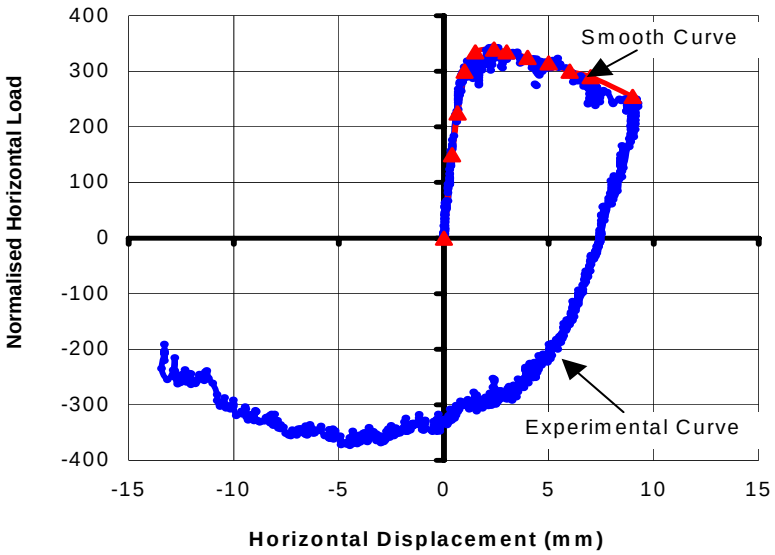

(a) Complete load-displacement curve

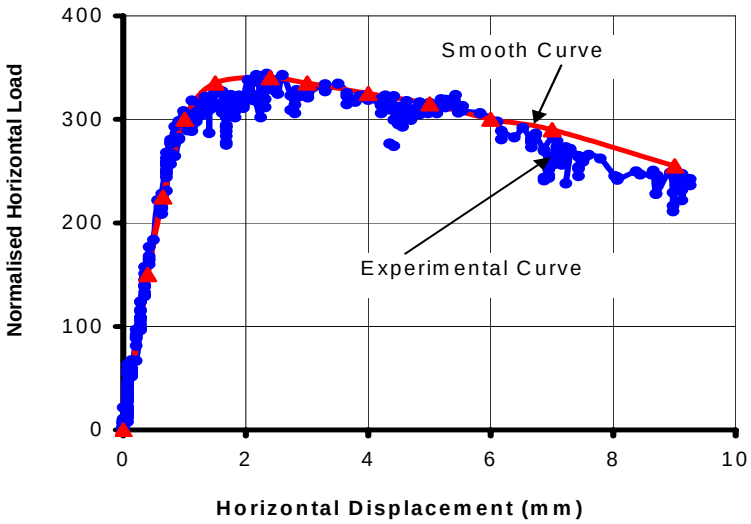

(b) Load-displacement curve in the forward direction loading

Figure 5.17: Load-displacement curve of ECRM wall

5.2.4 Group #6 Wall (URM)

The monotonic load-displacement curve of the URM wall is shown in Figure 5.18. The maximum normalised horizontal load of "280" for the URM wall was equivalent to 112kN of the actual experimental load. The smoothed curve to the experimental load-displacement curve of the URM wall under horizontal loading in the forward and reverse directions is shown in Fig. 5.18(a). The forward direction curve is shown in Fig. 5.18(b) for clarity.

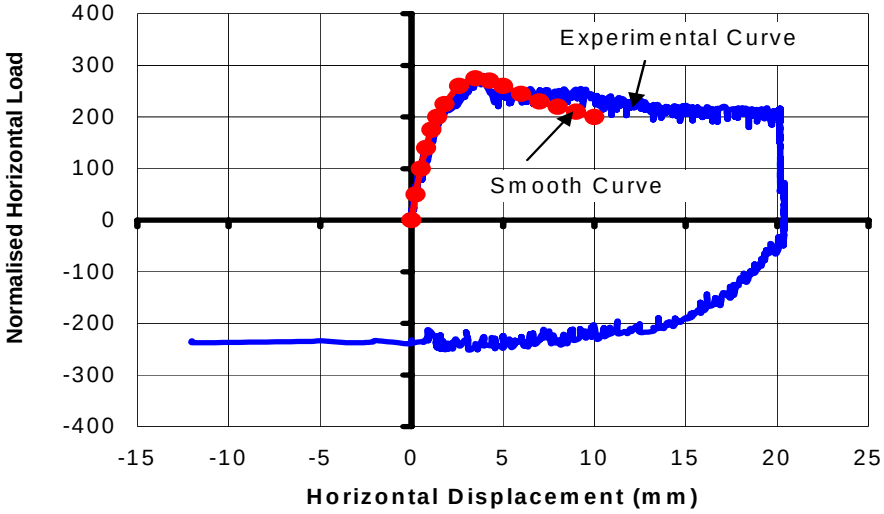

(a) Complete load-displacement curve

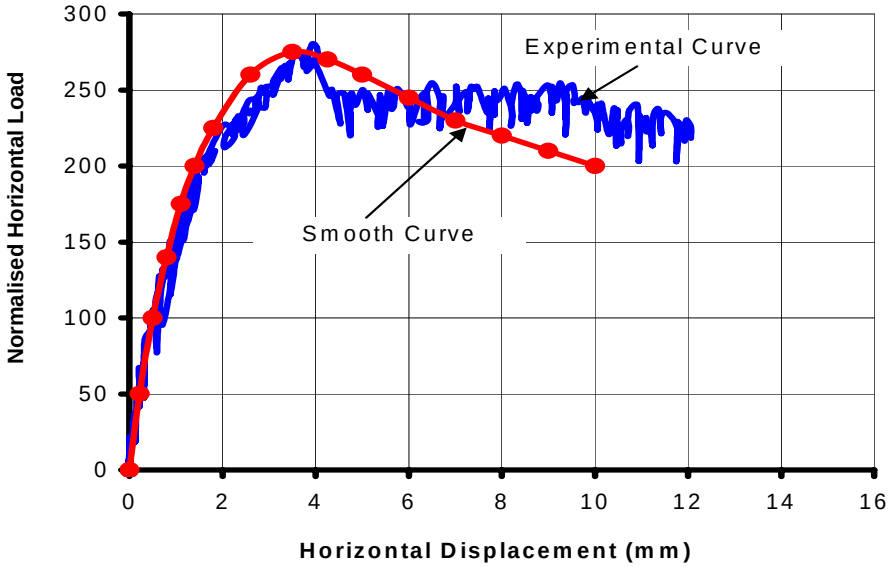

(b) Load-displacement curve in the forward direction loading

Figure 5.18: Load-displacement curve of URM wall

After reaching the peak load, the URM wall exhibited a sudden loss in the horizontal load and then was able to be pushed for a horizontal displacement of 20mm or more. The experiment in the forward direction was stopped when the cracks had opened significantly (as high as 5mm crack width). It is clear from Fig. 5.18(a) that, upon reversal of horizontal displacement, the

URM suddenly lost all of its resistance to the horizontal load. This loss may be attributed to accumulation of significant damage due to forward monotonic loading.

It is noticed from Fig. 5.18(b) that the URM wall exhibited a significant change in its load-displacement curve at an approximate horizontal displacement of 5mm in the forward direction. At 5mm of horizontal displacement, the URM had lost 10% of its peak load; therefore the smooth curve was extended based on the behaviour of the experimental load-displacement curve to determine the ultimate load capacity of the wall. The ultimate normalised load of "225" was found at a horizontal displacement of 8mm.

5.3 Discussion

Based on the load-displacement curves for the six groups (10 walls) of the masonry walls presented in section 5.2, it has been attempted in this section to categorise them as WSRM or Non-WSRM walls. Smoothed normalised load-displacement curves of the six walls obtained from monotonic and cyclic loading are presented in Fig. 5.19 to examine any systematic effect of either the spacing of the vertical reinforced cores or the loading history (monotonic/cyclic).

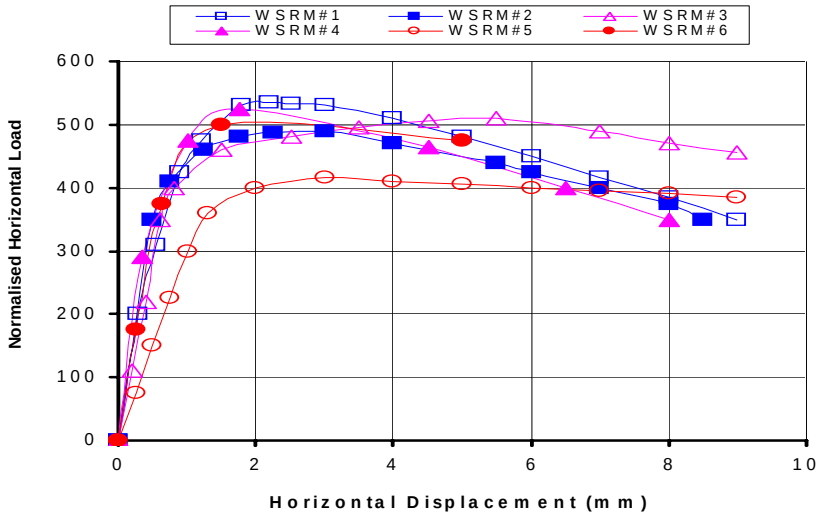

Figure 5.19: Smooth curves for WSRM walls – monotonic and cyclic load behaviour

It could be seen from Fig. 5.19 that the curves generally showed scatter without any systematic bias towards either the spacing of the reinforced grouted cores or the loading history.

WSRM#1 exhibited the highest normalised peak load of "540" whereas WSRM#5 exhibited the lowest normalised peak load of "420" defining a scattering of 22%. It appears from Fig. 5.19 that all the six WSRM walls reached the ultimate load capacity at an average horizontal displacement of 8mm. At the ultimate horizontal displacement (8mm), WSRM #3 exhibited the highest horizontal load of "470" whereas WSRM #1 exhibited the lowest horizontal load of "350" defining a scatter of 26%. Based on these observations, these six walls (WSRM#1 to WSRM #6) are considered as a single group (WSRM) with similar hardening and softening trends and close values of the peak lateral loads.

Normalised smooth curves of the last three groups (wall #7, #8, #9 and #10) are presented in Fig. 5.20. Maximum horizontal spacing between the vertical grouted cores in walls of group #4 (wall #7, #8), and group #5 (wall #9) was equal to 2000mm and 2685mm respectively whereas wall #10 was unreinforced ungrouted.

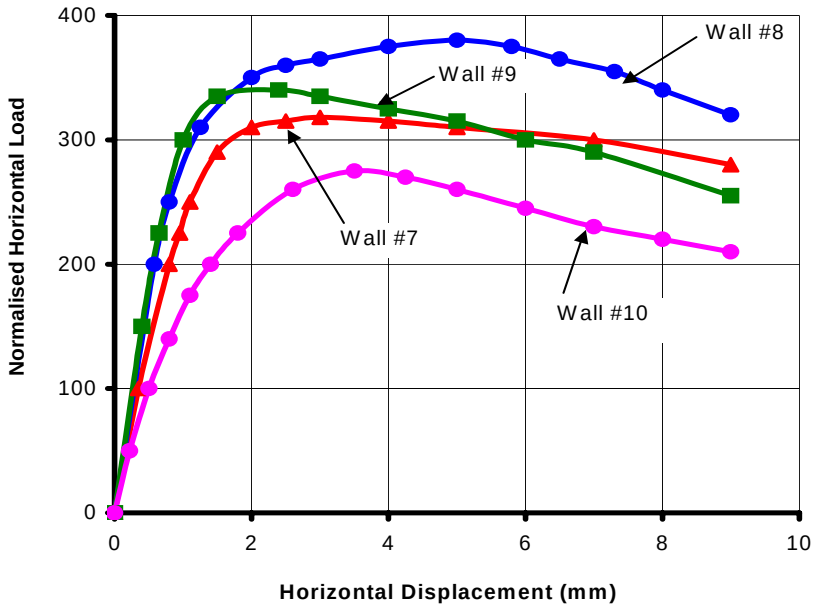

Figure 5.20: Smooth curves for Non-WSRM walls

Similar to the walls of the WSRM group, walls of the Non-WSRM group generally showed scatter without any systematic bias towards either the spacing of the reinforced grouted cores or loading history. WSRM#8 exhibited the highest normalised peak load of "380" whereas WSRM#10 exhibited the lowest normalised peak load of "275" defining a scattering of 28%. It appears from Fig. 5.20 that all four Non-WSRM walls reached the ultimate load capacity at an average horizontal displacement of 7mm. At the ultimate horizontal displacement (7mm), WSRM#8 exhibited the highest horizontal load of "360" whereas WSRM#10 exhibited the lowest horizontal load of "230" defining a scatter of 36%. Based on these observations, these four walls (#7 to #10) are considered as a single group (Non-WSRM) with similar hardening and softening trends and close values of the peak lateral loads.

Maximum peak normalised horizontal load for Non-WSRM (#7 to #10) walls was smaller than "400" whereas this value for the WSRM (#1 to #6) walls was more than "400". From Fig. 5.19 and Fig. 5.20, conclusions can be drawn that the limit specified in clause 8.6.2 of AS3700 (2001) for the WSRM walls is appropriate and the masonry walls with spacing between the vertical grouted cores equal to 2000mm or more should not be considered as WSRM walls.

It therefore can be concluded that, in spite of the presence of end cores with reinforcement and subsequent marginal improvements in the behaviour, the ECRM walls can be regarded as URM walls for practical purposes. This conclusion is consistent with the provisions in AS3700 (2001). All walls not conforming to WSRM walls are defined as Non-WSRM walls in further discussions in this thesis.

5.4 Shear Capacity

Experimental values of the shear capacity under forward monotonic and cyclic loading determined from smooth normalised load-displacement curves (presented in section 5.2) are reported in Table 5.1.

Table 5.1: Experimental normalised shear capacity of walls

Type of Walls	Group # As per Fig. 4.1	Wall No.	Loading History	Normalised Forward Loading		% Difference
				Capacity	Ave.	
WSRM Walls	Group #1	WSRM#1	Monotonic	535	497.5	7.5
		WSRM#2	Cyclic	490		-1.5
	Group #2	WSRM#3	Monotonic	510		2.5
		WSRM#4	Cyclic	525		5.5
	Group#3	WSRM#5	Monotonic	415		-16.6
		WSRM#6	Cyclic	510		2.5
Non-WSRM Walls	Group #4	WSRM#7	Monotonic	318	328.3	-3.1
		WSRM#8	Cyclic	380		15.7
	Group #5	ECRM	Monotonic	340		3.6
	Group #6	URM	Monotonic	275		-16.2

The average value of the normalised peak horizontal load for WSRM (#1 to #6) and Non-WSRM (#7 to #10) walls is equal to “497.5” and “328.3” respectively. From these results it is evident that the average normalised peak load of WSRM walls was 34% higher than that for the Non-WSRM walls, which is significant to distinguish the two types of masonry shear walls. Maximum percentage difference in the shear capacity of the WSRM and Non-WSRM walls from their respective average value is 16.6% and 16.2%, which is considered as a normal level of variability among the masonry researchers. Table 5.1 is also showing that the masonry shear walls containing vertical reinforced grouted cores at the horizontal spacing of 2000mm or more should be considered as URM walls rather than WSRM walls.

5.4.1 Prediction Equation

Researchers have proposed several empirical shear capacity equations for the partially reinforced masonry. Various equations available in the literature to predict the shear capacity of the masonry shear walls are discussed in the literature review (section 2.5.1). A good correlation between the computer programs and experimental results for the inelastic behaviour of reinforced masonry shear walls has been found by Shing et al. (1990a). Different shear capacity equations available in the literature are used in this section to calculate the shear capacity of the WSRM and the URM shear walls tested as part of this thesis.

5.4.2 WSRM Walls

Clause 8.6.2 of the Australian Standard for masonry structures AS3700 (2001) proposes a shear capacity equation for WSRM walls as shown in Eq. 5.2.

$$V_d \leq \phi \, (f_{vr} \, A_d + 0.8 \, f_{sy} \, A_s) \qquad (5.2)$$

where

$$f_{vr} = (1.50 - 0.5 \, H / L) \text{ MPa} \qquad (5.3)$$

'V_d' is the design shear force acting on the cross-section of the masonry walls; 'H' and 'L' are the height and length of the shear wall in millimetres (mm) respectively; 'A_d' is the design cross-sectional area of the wall; 'f_{sy}' is the yield strength of the reinforcement in MPa and 'A_s' is the area of the vertical reinforcement in the WSRM walls in mm^2. 'A_s' is the cross sectional area of the reinforcement bars. 'A_s' is given by $A_{sh} \times L/H$ if $H/L > 1.0$, otherwise 'A_s' is the lesser of the area of the horizontal (A_{sh}) and the vertical reinforcement. In the WSRM walls, there was no horizontal reinforcement except in the bond beam. Since the horizontal reinforcement in the bond beam does not take the shear load applied to the walls, the effective horizontal

reinforcement is considered zero. Shear capacity of the WSRM walls calculated from Eq 5.2 are reported in Table 5.2. A value equal to 1.0 was used in Eq. 5.2 for capacity reduction factor (ϕ).

Some researchers have attempted to predict the shear capacity of partially reinforced masonry shear walls from empirical equations. For example, Fattal and Todd (1993) investigated the effectiveness of empirical equations proposed by Matsumura (1988), Shing et al. (1990a), Okamoto et al. (1987) and UBC (1988) for predicting the shear capacity of the fully reinforced and partially reinforced masonry shear walls. They found that the equation proposed by Matsumura (1988) was the closest predictor of shear capacity of most of the reinforced masonry shear walls, however, this equation could not predict the shear capacity of the URM and partially reinforced masonry shear walls. Therefore, as part of the National Institute of Standards and Technology (NIST) masonry research program, Fattal (1993b) used statistical methods to modify the equation of Matsumura (1988) to predict shear capacity closer to the experimental values of 72 partially reinforced and unreinforced masonry shear walls obtained from three different test programs reported by Yancey et al. (1990). The modified equation of Matsumura (1988) provided by Fattal (1993b) that relates the nominal shear capacity (v_n) of the masonry walls to the shear strength of its constituents is shown in Eq. 5.4.

$$v_n = v_m + v_s + v_a \tag{5.4}$$

where v_m, v_s, v_a respectively are the contributions of masonry, horizontal reinforcement, and axial compression to shear capacity. Eq 5.4 is rewritten as shown in Eq. 5.5.

$$v_n = k_o k_u \left[\left\{\frac{0.5}{r+0.8}\right\} + 0.18\right]\sqrt{f'_m f_{yv}}\,(\rho_v)^{0.7} + 0.011 k_o \gamma \delta f_{yh} \rho_h^{0.31} + 0.012 k_o f'_m + 0.2\sigma_c \tag{5.5}$$

where 'ρ_v' and 'ρ_h' are ratios of vertical and horizontal reinforcement respectively, and 'f_{yv}' and 'f_{yh}' are the nominal yield stresses of the vertical and horizontal reinforcement respectively. The

dimensionless factors (k_o, k_u and γ) used in Eq. 5.5 are 0.8, 0.64 and 0.60 respectively for concrete masonry and 0.80, 0.80 and 1.00 respectively for clay masonry.

The nominal shear capacity of a wall (V_n) is calculated as a product of the nominal shear strength (v_n) and the net horizontal cross-sectional area (A_n) of the wall. Eq 5.5 was used in this section to calculate the shear capacity of the WSRM walls.

Values of the parameters used in Eq. 5.5 were: Height of the walls (H) = 2408mm, length of the walls (L) = 2870mm, thickness of the walls (t) = 150mm, distance from the centre of the tension reinforcement to the extreme compression fibres (d) = 2790mm, spacing of the horizontal reinforcement (S_h) = vertical distance from the base of the wall to the mid height of the bond beam = 2332mm, yield strength of the horizontal and the vertical reinforcement (f_{yh}=f_{yv}) = 500MPa, reinforcement ratio of the reinforcement in the end cores of the WSRM walls (ρ_{ve}) = 0.00033, ratio of the total vertical reinforcement (ρ_v) = 0.001022, area of the vertical reinforcement (A_v) = 440mm^2, horizontal reinforcement ratio (ρ_h)= 0.00111, area of the horizontal reinforcement (A_h) for two N16 reinforcement bars = 400mm^2, aspect ratio of the wall (r = H/L) = 0.84 and (r_d= H/d) = 0.86, vertical pre-compression (q) = 0.5MPa. Compressive strength (f_m) for each wall used in Eq. 5.5 was read from Table 4.2. Values of the shear capacity calculated from Eq. 5.5 are reported in Table 5.2.

Table 5.2: Experimental and predicted shear capacity of the WSRM walls

Wall No.		WSRM# (1)	WSRM# (2)	WSRM# (3)	WSRM# (4)	WSRM# (5)	WSRM# (6)	Average Difference
Experimental Shear Capacity (kN)		179.1	161.0	180.3	190.7	155.7	191.0	
Predicted Shear Capacity (kN)	AS3700 (2001)	251.7						
	% Difference	29%	36%	28%	24%	38%	24%	30%
	Fattal and Todd (1993)	179.1	166.6	179.5	184.4	212.0	216.9	
	% Difference	0	3.1	-0.4	1.9	26.6	11.9	7.2%

Experimental values of the shear capacity (without normalisation) are compared with values of the shear capacity predicted by clause 8.6.2 of AS3700 (2001) and by the empirical Eq.5.5 provided by Fattal and Todd (1993). Both of these shear capacity equations do not account for the effect of spacing of the vertical reinforcement, rather they assume uniform distribution of the vertical reinforcement bars. Instead of normalised peak loads, actual experimental values of the shear capacity were used because the equation of Fattal and Todd (1993) accounted for the effect of material variation.

It is interesting to note that both the equations have over-predicted the shear capacity of the WSRM walls. The equation available in AS3700 (2001) does not consider the effect of the strength of the constituent materials of the WSRM walls and is found to be on average 30% non-conservative. The equation of Fattal and Todd (1993) was found to be 7.2% non-conservative on average. The equation 8.6.2 (1) of AS3700 (2001) definitely requires critical review as unsafe prediction of the shear capacity of the WSRM walls currently results.

5.4.3 Non-WSRM Walls

Since the ECRM walls contain vertical reinforced grouted cores at a horizontal distance equal to or more than 2000mm, AS3700 (2001) considers them as unreinforced masonry walls. Their shear capacity is calculated from Eq. 5.6 available in clause 7.6 of AS3700 (2001) and is reported in Table 5.3.

$$v_d = v_o + v_l \tag{5.6}$$

where

$$v_o = f_m A_d \tag{5.7}$$

and

$$v_l = k_v f_d A_d \tag{5.8}$$

in which ' f_m ' is the characteristic shear strength of masonry, 'A_d' is the design area of the walls, 'k_v' is a shear factor, 'f_d' is minimum design compressive stress. Values of f_m , f_d and k_v used in calculation of shear capacity of the ECRM walls were equal to 0.35MPa, 0.5MPa and 0.3 respectively. These values were adopted as per guidelines of AS3700 (2001). Design area of the ECRM walls was calculated as bedded area of the wall (200,900mm^2). Shear capacity of the ECRM walls is also calculated from equation of Fattal and Todd (1993) (Eq. 5.5) and its values are provided in Table 5.3. Reinforcement ratio (ρ_{ve}) of the reinforcement in the end cores of the ECRM walls was equal to 0.00051. Design areas of the walls of Group #4 (walls #7 and #8), Group #5 (wall #9) and Group #6 (wall#10) were equal to 232,900mm^2, 216,900 mm^2 and 200,900mm^2 respectively

Table 5.3: Shear capacity of Non-WSRM walls

Wall No.		WSRM#7	WSRM#8	ECRM	URM	Average
Group		#4		#5	#6	
Experimental Capacity (kN)		129.2	153.1	144.4	110.5	134.3
AS3700 (2001)	Predicted Capacity	116.5		108.5	100.5	110.5
	% Difference	-9.8	-24.4	-25.2	-9.0	-17.1
Fattal and Todd (1993)	Predicted Capacity	119.1	117.9	126.1	107.9	117.8
	%Difference	-7.9	-23.5	-18.3	-2.6	-13.1

It is noticed that both the AS3700 (2001) and Fattal and Todd (1993) equations have conservatively predicted the shear capacity of the Non-WSRM walls. AS3700 (2001) and Fattal and Todd (1993) predicted the shear capacity of the Non-WSRM walls with variation on average of 17.1% and 13.1% respectively. AS3700 (2001) which is a rather simple equation has predicted the shear capacity with a maximum conservativeness of 25.2% in contrast to the complex equation of Fattal and Todd (1993) which predicted the shear capacity of the Non-WSRM walls with a maximum difference of 23.5%. It can therefore be concluded that both the equations could predict the shear capacity of the URM wall / Non-WSRM walls efficiently.

5.5 Ductility

The term ductility refers to the ability of a structure to deform beyond its elastic limits without excessive strength decay or stiffness degradation. Ductile structures are able to deform beyond their peak load without collapse. The term ductility could be associated with the material behaviour, the cross-sectional behaviour, the member behaviour and the overall structural behaviour; in this study displacement ductility of the member as defined in Eq. 5.9 and 5.10 is used. Mathematically, displacement ductility is defined as the ratio of the ultimate displacement (D_u) to the yield displacement (D_y) as shown in Eq. 5.9.

$$\mu_d = \frac{D_u}{D_y} \tag{5.9}$$

Using Eq. 5.9, ductility of the structural elements is calculated at the ultimate stage only. To understand the level of ductility of the masonry shear walls at different load levels, Eq. 5.10 is used.

$$\mu_d = \frac{D^*}{D_y} \tag{5.10}$$

where D^* is a prescribed displacement beyond yield. Identification of yield and ultimate points on the load-displacement curve play an important role in the accuracy of the calculated factors. Several methods are found in the literature to define the yield and the ultimate points on the load-displacement curves of shear walls or beam-columns. In this thesis, the concept of the equivalent elastic-perfectly plastic system proposed by Muguruma et al. (1991) was used for the identification of the yield point. This model is graphically illustrated in Fig. 5.21.

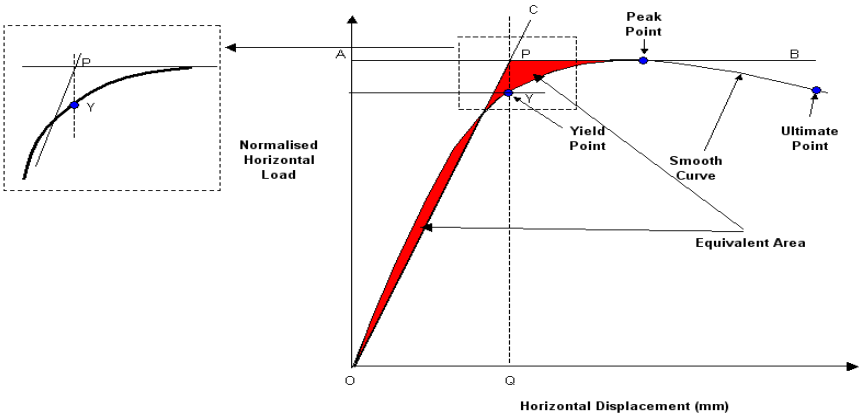

Figure 5.21: Model for identification of yield point

According to this model a horizontal line (AB) is drawn at the maximum (peak) load level of the load-displacement curve and an inclined line (OC) is then drawn from the origin such that it provides equal pre and post yield energy (shown as the shaded area in Fig. 5.21). A vertical line (PQ) is then drawn from the point (P) where the inclined line intersects the horizontal line. The point where the vertical line intersects the load-displacement curve (Y) is defined as the yield point, and its corresponding load and displacement are called the yield load and the yield displacement respectively.

According to Muguruma et al. (1991) and Saatcioglu (1991), reinforced columns reach their ultimate displacement when reduction in their shear capacity exceeds 20% of the peak load. In contrast, some of the walls tested during this research did not lose 20% of the peak load until they reached very large displacements (where experiments were to be stopped for reasons described in section 4.4.4), therefore the smoothed load-displacement curves were extrapolated as shown in section 5.2 to determine the ultimate point.

To simplify the discussions on ductility, the averages from each group of walls tested were drawn. Smoothed load-displacement curves for WSRM and Non-WSRM walls presented in Figs. 5.7, 5.10, 5.13 and 5.20 are reproduced in Fig. 5.22 along with their average curves.

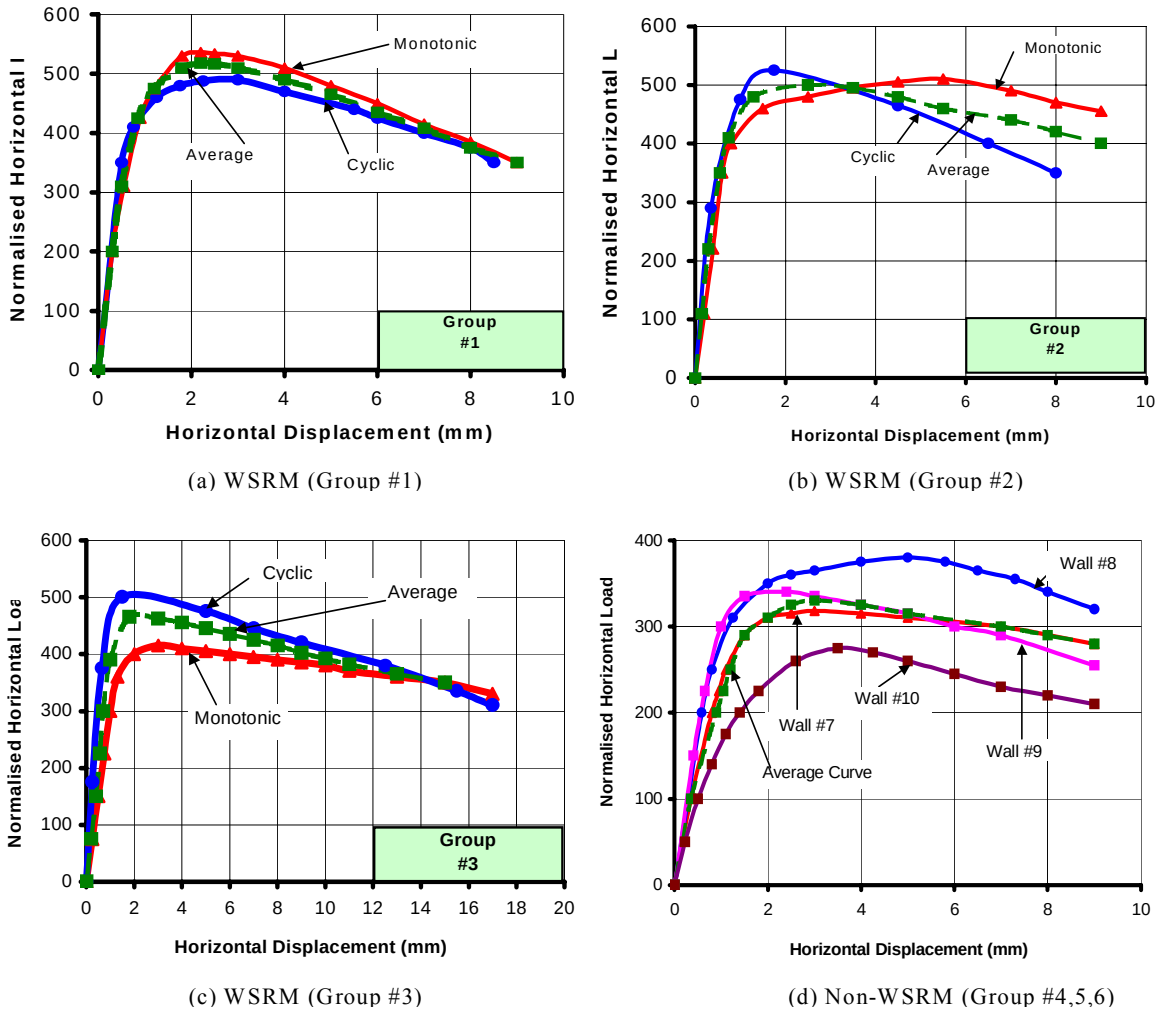

Figure 5.22: Average load-displacement curves for WSRM and Non-WSRM walls

In addition to the displacement ductility factor, drift ratio and structural response factor (R_f) are also calculated as these are important parameters that characterise the behaviour of the shear walls. Drift ratio is calculated as the ratio of the horizontal deflection of the wall to the height of the wall and the structural response factor (R_f) is calculated from Eq. 5.11 provided by Paulay and Priestley (1992)

$$R_f = \sqrt{2\,\mu_d - 1} \qquad (5.11)$$

where 'μ_d' is the displacement ductility of the walls.

The equivalent elastic-perfectly plastic model (Fig. 5.21) was used to determine the yield, the peak and the ultimate load stages from the average load-displacement curves provided in Fig. 5.22 and their values are reported in Table 5.4. The ductility factor calculated from Eq. 5.10, the structural response factor calculated from Eq. 5.11 and the drift ratios are also provided in Table 5.4.

Table 5.4: Loads, displacements and ductility of WSRM and Non-WSRM walls

Wall No.		WSRM Walls				Non-WSRM Walls
Group		#1	#2	#3	Average	#4, #5, #6
Yield Load Stage	Normalised Horizontal Load	425	450	430	435	300
	Displacement (mm)	1.0	1.2	1.4	1.2	1.8
	Drift Ratio (%)	0.04	0.05	0.06	0.05	0.07
Peak Load Stage	Normalised Horizontal Load	518	500	475	498	330
	Displacement (mm)	2.0	2.5	2.0	2.2	3.0
	Ductility	2.0	2.1	1.4	1.8	1.7
	Drift Ratio (%)	0.08	0.10	0.08	0.09	0.12
Ultimate Load Stage	Normalised Horizontal Load	414	400	380	398	264
	Displacement (mm)	7.0	9.0	11.0	9.0	9.5
	Ductility	7.0	7.5	7.9	7.5	5.3
	Drift Ratio (%)	0.29	0.37	0.46	0.37	0.39
	Response Factor	3.6	3.7	3.8	3.7	3.1

The WSRM walls yielded at an average displacement of 1.2mm, which is significantly smaller than the yield displacement of the Non-WSRM walls (1.8mm). This finding is consistent with the hypothesis of early cracking of WSRM walls made in Chapter 3.

The ductility factor of the WSRM walls was equal to 1.8 at the peak load stage, which increased to 7.5 at the ultimate load stage. Similarly, the average value of drift ratio was 0.09 at the peak load stage and increased to 0.37 at the ultimate load stage. Significant increase in the ductility factor and the drift ratio shows that the WSRM walls exhibited quite ductile behaviour before reaching their ultimate load stage.

Average values of normalised horizontal load at the yield, the peak and the ultimate load stage for the Non-WSRM walls were equal to “300”, “330” and “264” respectively. They were 31%, 34% and 33% less than the corresponding average values of the WSRM walls.

At ultimate load stage, the ductility factor of the Non-WSRM walls was equal to 71% of that of the WSRM walls. Although the ultimate drift ratio of both the WSRM and the Non-WSRM walls are similar (0.37 and 0.39 respectively), the ultimate ductility of the Non-WSRM walls was 29% lower than that of the equivalent WSRM walls. This indicates that the ultimate horizontal displacement of the Non-WSRM walls contains a significant proportion of rigid body deformation.

Based on these results, it becomes evident that the WSRM walls showed highest ductility, normalised horizontal load and structural response factor. Non-WSRM walls exhibited higher drift ratio but their ductility, normalised horizontal load and the structural response factors were less than those for WSRM walls.

5.6 Damage Characteristics

In order to assess the level of damage, stiffness degradation, toe and heel deformation, diagonal deformation and centre deformation are calculated and presented in this section.

Typical plots of toe and heel deformation, diagonal deformation and centre deformations of the walls are provided in section 4.5 of Chapter 4. Their values for the WSRM wall and the Non-WSRM walls are presented in this section.

5.6.1 Stiffness Degradation

Stiffness degradation (C_K) of the structural elements is defined by the rate of reduction in stiffness beyond yield. Mathematically it is expressed as the ratio of the secant modulus at a specified displacement (K) to the secant modulus at yield (K_o) as shown in Eq. 5.12.

$$C_k = \frac{K}{K_o} \tag{5.12}$$

where 'K_o' is the slope of a line passing through the origin to the yield point and '$K^{'}$ is the slope of a line passing through the origin to a specified point on the load deflection curve as shown in Fig. 5.23. This model measures the degradation in stiffness when the wall is pushed from the yield load level to the ultimate load level. It is assumed that the stiffness remains unchanged before the wall reaches its yield point.

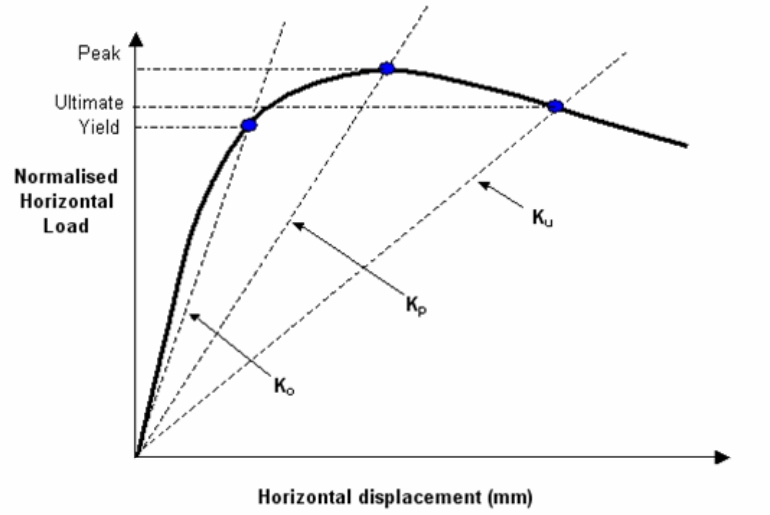

Figure 5.23: Stiffness degradation model

This model was originally proposed by Usami et al. (1991) to define the stiffness degradation (C_K) for reinforced concrete columns subjected to cyclic loading. As this model is simple, it is used here to determine the stiffness degradation of masonry walls in this thesis.

The stiffness degradation model provided in Fig. 5.23 was applied to the average load-displacement curves for the WSRM and Non-WSRM walls presented in Fig. 5.22. Values of stiffness at the yield (K_o), the peak (K_p) and the ultimate (K_u) load stages are reported in Table 5.5.

Table 5.5: Stiffness degradation of the walls

Parameters	WSRM Walls				Non-WSRM Walls
Group	#1	#2	#3	Average	
K_o (mm^{-1})	425.0	375.0	307.0	369.0	166.7
K_p (mm^{-1})	259.0	200.0	237.5	232.2	110.0
K_u (mm^{-1})	59.1	44.4	34.5	46.0	27.8
C_{kp} (%)	39	47	23	37	34
C_{ku} (%)	86	88	89	88	83

Stiffness was calculated as the ratio of the normalised values of the horizontal load to the corresponding horizontal displacement, therefore the unit of the stiffness parameters (K_o, K_p, K_u) is mm^{-1}. The average value of initial stiffness of "369 mm^{-1}" for WSRM walls was 55% higher than that for the Non-WSRM walls. This observation is consistent with the hypothesis made in Chapter 3. Similarly, the average stiffness of "232.2 mm^{-1}" at the peak load of the WSRM walls was 53% higher than that for the Non-WSRM walls. At the ultimate load stage, the average stiffness of the Non-WSRM walls was only 40% of the average for the WSRM walls. It is noticed that stiffness degradation at the peak and the ultimate load stages for the Non-WSRM walls were similar to those for the WSRM walls.

5.6.2 Toe and Heel Deformation

Lateral load - vertical deformation plots under monotonic load at the toe and at the heel of the walls is shown in Fig. 5.24. Data from only some selected walls are provided here to maintain clarity. It is evident from this figure that the URM walls exhibited both more toe and heel

vertical deformation than did the WSRM (#5) and the ECRM (#9) walls. The corresponding deformations in the WSRM and the ECRM walls are almost the same because both types of walls had grouted cores at the heel and the toe.

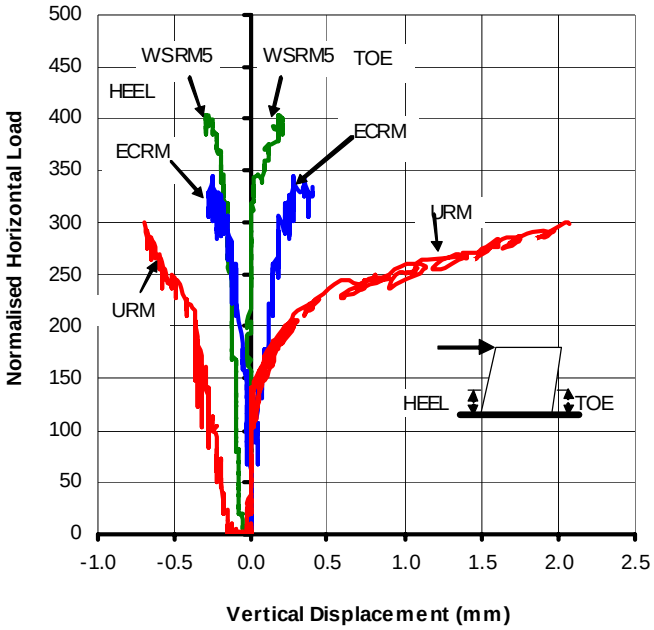

Figure 5.24: Toe and heel deformation of the walls under monotnic loading

Values of the vertical deformations of the toe and the heel of the WSRM and Non-WSRM walls at the peak load stage are reported in Table 5.6.

Table 5.6: Vertical deformations (mm) at the toe and the heel of walls at peak load stage

	WSRM Walls							Non-WSRM Walls				
Wall #	1	2	3	4	5	6	Ave.	7	8	9	Ave.	10
Heel	-0.27	-0.38	-0.45	-0.46	-0.27	-0.25	-0.34	-0.30	-0.62	-0.05	-0.32	-0.69
Toe	0.27	0.32	0.40	0.26	0.17	0.43	0.31	0.05	0.73	0.17	0.32	2.10

Values of the vertical deformation at the toe and the heel of the WSRM are similar to that for the Non-WSRM walls (excluding URM #10 wall) showing that the grouted core at the toe and the heel was equally effective for the WSRM and the Non-WSRM walls. From Table 5.6 it is

evident that the vertical deformation at toe and heel of the URM wall were significantly higher than those for WSRM and the other Non-WSRM walls, which shows splitting of the masonry courses at the heel and rigid body rotation in the URM wall.

5.6.3 Diagonal Deformation

Typical diagonal deformations of the walls under monotonic and cyclic loading are presented in Fig. 4.15 (Chapter 4). Deformation along the diagonals of the walls under monotonic loading is plotted in Fig. 5.25 and the values of the diagonal deformation at the peak load stage are reported in Table 5.7.

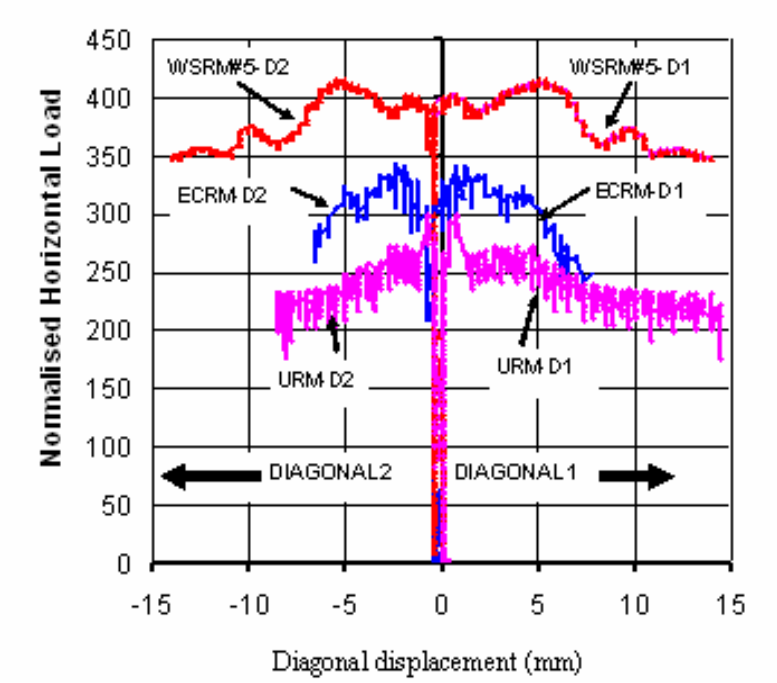

Figure 5.25: Diagonal deformation of the walls

Diagonal deformations were not measured for WSRM walls #1 to #4. String pots for WSRM#6 were locally disturbed and hence could not produce reliable diagonal deformation data for this wall.

Table 5.7: Deformation along diagonals of walls (mm) at peak load stage

	WSRM Wall	Non-WSRM Walls				
Wall	#5	#7	#8	#9	Average	#10
Diagonal 1	5.0	3.5	3.5	3.8	3.6	0.78
Diagonal 2	-5.0	-2.70	-3.10	-3.10	3.0	-0.78

The average value of deformation along the compressive and the tensile diagonals of the WSRM wall at the peak load was equal to approximately 5mm. Corresponding values for the Non-WSRM (except URM wall #10) walls were equal to 3.6mm and 3.0mm respectively. The peak load deformation along the diagonals of the URM walls was equal to 0.78mm. These data could be collected only for a limited number of tests; however, they provided important information. From Table 5.7, it becomes evident that the WSRM walls and the Non-WSRM walls (except URM wall) transferred most of the shear load within their body whereas the URM wall transferred the shear load (without much material deformation) through significant rigid body rotation resulting in rocking mode of failure.

5.6.4 Centre Zone Deformation

Typical deformation data at the centre along the horizontal, vertical and diagonal directions have already been previously presented in Fig. 4.14. LVDTs at the centre zone of most of the walls especially under cyclic loading using the push and pull mechanism were disturbed, hence consistent deformation data could not be collected for all walls. However, deformation data for some walls were collected and are presented in Table 5.8.

Table 5.8: Strain at the centre of the test walls at peak load stage (gauge length 200mm)

	WSRM# 1	WSRM# 3	WSRM# 5	WSRM# 7	URM
Average horizontal displacement (mm)	0.045	3.3	3.4	1.1	0
Average vertical displacement (mm)	0.045	0.5	0.95	1.1	0
Average displacement along diagonal (mm)	0.045	4.5	3.3	1.1	0

The WSRM#1 wall showed very small deformation at the centre because it contained intermediate vertical reinforced cores at the centre that locally minimised the crack width of the masonry. However, in this wall the crack did appear at the centre after the peak load stage passed.

The WSRM#3 and WSRM#5 walls, which had fairly uniformly distributed vertical reinforced cores, exhibited larger deformations (strains) than those for WSRM#7.

The URM wall exhibited no deformations (strains) at peak load due to less deformation at the centre (most of the overall horizontal deflection appears to be related to rotations due to heel / toe vertical deformation). That the crack did not pass exactly through the centre (see Fig. 4.24(a)) where the LVDTs were installed also contributed to this insignificant measured deformation at the centre of the URM wall.

As cracking dominated post-peak deformations at the central zone of the walls, no attempt was made to convert the deformations presented in this section to inplane strain state (horizontal, vertical or shear strains).

5.7 Effect of Spacing of Vertical Reinforcement

To understand the effect of spacing of the vertical reinforcement, the normalised horizontal load and ductility factors of the walls determined from the average load-displacement curves presented in sections 5.2 and 5.3 of this chapter are plotted as a function of horizontal spacing between the vertical reinforcement bars in Fig. 5.26. Average values of normalised horizontal load for both WSRM and the Non-WSRM walls at the peak load stage are included in Fig. 5.26(a).

Ductility factors calculated from the average curves shown in Fig. 5.22 for the WSRM and Non-WSRM walls and are plotted in Fig. 5.26(b).

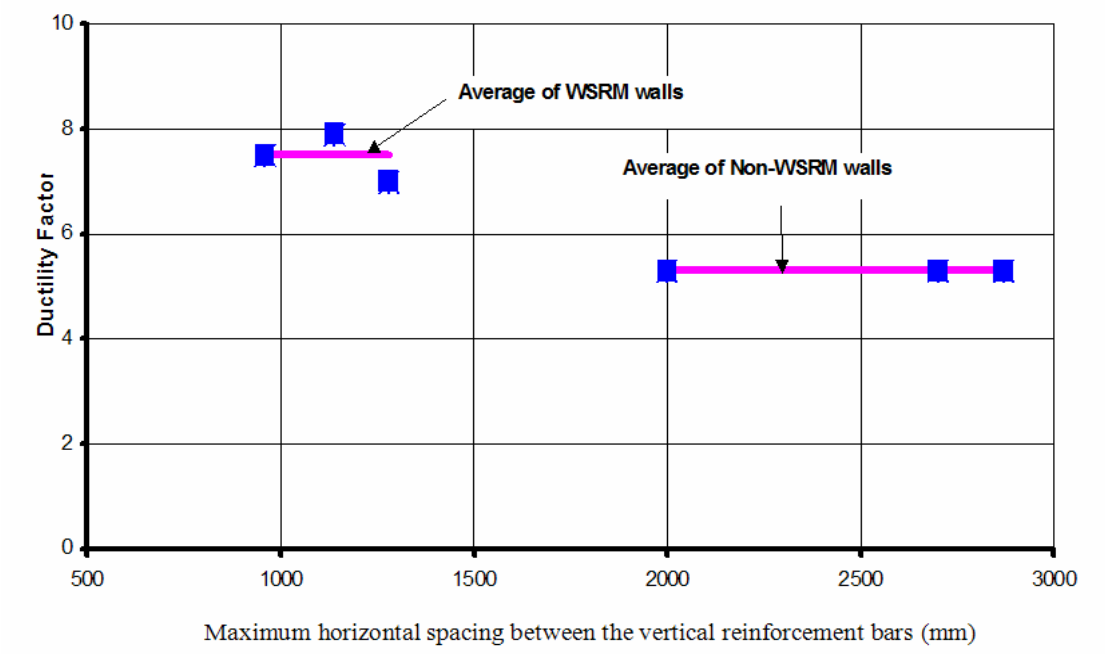

(a) Ductility of WSRM and Non-WSRM walls

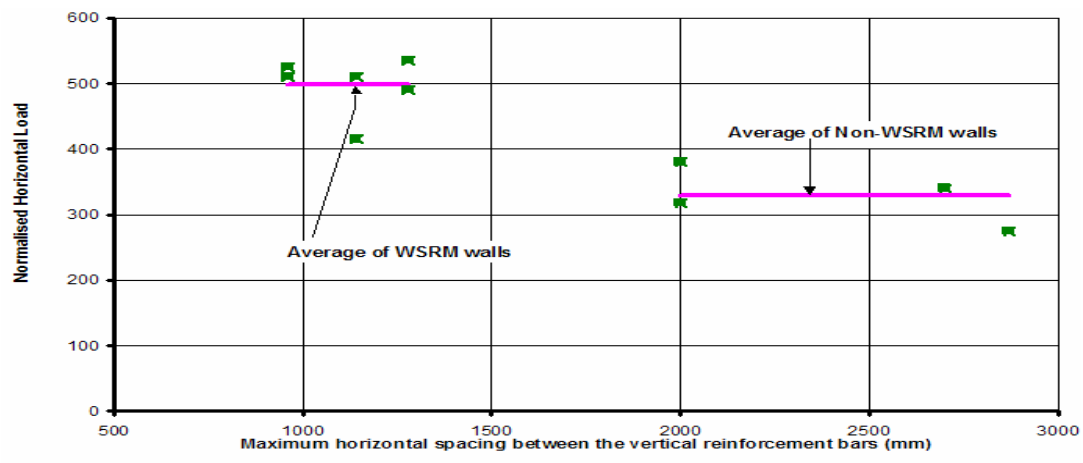

(b) Normalised load of WSRM and Non-WSRM walls

Figure 5.26: Ductility and normalised horizontal load at ultimate load stage

It can be seen that the ductility factors as well as values of the peak normalised horizontal loads of the WSRM walls are significantly higher than those for the Non-WSRM walls. The limit of 2000mm specified in clause 8.6.2 of AS3700 (2001) for the vertical reinforcement bars for the

WSRM and the URM walls seems adequate as the behaviour of the two types of the walls are significantly different. For practical design purposes, the walls containing vertical reinforced cores at horizontal spacing of 2000mm or more could be safely classified as URM walls.

5.8 Summary

Behaviour of masonry walls containing only 0.10% (based on gross dimensions of the walls) of vertical reinforcement and subjected to uniform vertical pressure of 0.5MPa under lateral monotonic and cyclic loading is investigated. Variation of the maximum spacing of the vertical grouted reinforced cores was the main parameter in this investigation. Shear capacity, ductility, stiffness degradation, structural response factor and amount of damage in critical regions of the walls have been investigated. Complete horizontal load-displacement curves under forward monotonic, reverse monotonic and cyclic loading have been included. It has been found that the hardening regimes, softening trends and normalised peak loads obtained under monotonic and cyclic loadings were similar for all the walls with the exception of small differences. Therefore, monotonic and cyclic envelope curves have been averaged to determine the response of the walls.

Shear capacity of the walls obtained from the experimental program has been reported and compared with that predicted by the equation available in the Australian Standard for masonry structures AS3700 (clause 8.6.2) and an empirical equation provided by Fattal and Todd (1993). Both the equations have provided non-conservative prediction of the shear capacity of the WSRM walls. The equation available in AS3700 (2001) predicted the shear capacity of the WSRM walls on average 30% non-conservatively (unsafe prediction). Therefore the equation 8.6.2 (1) of AS3700 (2001) must be reviewed and improved to provide conservative prediction of the shear capacity of the WSRM walls.

Two groups of masonry shear walls emerged based on the values of normalised horizontal load, displacement ductility factors, stiffness values and damage characteristics. The first group consisted of WSRM walls #1 to #6 in which maximum horizontal spacing between the vertical reinforcement bars was less than 2000mm. The second group consisted of masonry walls containing vertical reinforcement bars at maximum horizontal spacing of 2000mm or more, or walls with no vertical reinforcement and no grouted cores (URM). This grouping is consistent with the AS3700 (2001) definition of the WSRM walls.

The average experimental values of the normalised horizontal load for the WSRM walls at the peak and the ultimate load stages was 34% higher than that for the Non-WSRM walls. The ductility factor of the WSRM walls was 29% higher than that for the Non-WSRM walls. Average stiffness values of the WSRM walls at the yield, the peak and the ultimate load stage were 55%, 53% and 40% higher respectively than that for the Non-WSRM walls. Vertical deformation at the toe (average 0.34mm) and the heel (average 0.31mm) of the WSRM and Non-WSRM walls were similar except for the URM wall. The URM wall exhibited larger vertical deformations at the toe (2.1mm) and the heel (0.69mm) due to the absence of grouted cores at the ends that were present for all the WSRM and the other Non-WSRM walls.

The URM wall exhibited rocking type of failure that did not happen for the WSRM and the other Non-WSRM walls due to presence of vertical reinforced cores at the ends. Due to the same reason, the WSRM walls dissipated most of the horizontal load at the centre and hence showed higher diagonal deformation at the centre than the other walls.

Based on the results discussed in this chapter, it becomes evident that the WSRM walls performed better than the Non-WSRM walls because the WSRM walls could resist higher lateral load and exhibited more ductility and better damage characteristics.